Enhancement of heat transfer by corona wind

tu/e
Research Report
ISSN 0167-9708
Coden: TEUEDE

Eindhoven
University of Technology
Netherlands

Faculty of Electrical Engineering

Enhancement of Heat Transfer by Corona Wind

by
H. Kadete

EUT Report 87-E-184
ISBN 90-6144-184-6
December 1987

Eindhoven University of Technology Research Reports

EINDHOVEN UNIVERSITY OF TECHNOLOGY

Faculty of Electrical Engineering
Eindhoven The Netherlands

ISSN 0167- 9708 Coden: TEUEDE

ENHANCEMENT OF HEAT TRANSFER BY CORONA WIND

by

H. Kadete

EUT Report 87-E-184
ISBN 90-6144-184-6

Eindhoven
December 1987

This report describes a study carried out in a cooperation of the Department of Electrical Engineering, University of Dar es Salaam, Tanzania, and the High-Voltage Group of Eindhoven University of Technology, the Netherlands. The experimental work done in Dar es Salaam is described in section 3.6.

This text was submitted to the University of Dar es Salaam as a Ph. D. Thesis earlier. As result the Doctor's degree, the first from the University of Dar es Salaam's Faculty of Engineering, was conferred to the author by the Chancellor of the University, President Mwinyi of Tanzania, on 29 August 1987.

CIP-GEGEVENS KONINKLIJKE BIBLIOTHEEK, DEN HAAG

Kadete, H.

Enhancement of heat transfer by corona wind / by H. Kadete. - Eindhoven: University of Technology, Faculty of Electrical Engineering. - Fig., tab. - (EUT report, ISSN 0167-9708; 87-E-184)
Met lit. opg., reg.
ISBN 90-6144-184-6
SISO 661.52 UDC 621.3.015.532-712 NUGI 832
Trefw.: corona-ontladingen.

ABSTRACT

The mechanism of heat transfer enhancement across solid gaseous interfaces by corona wind directed towards the heat transfer surface is investigated. Basic principles of heat transfer, negative dc corona, and the nature of corona wind are studied. Voltage-current characteristics of negative dc corona in geometries which create corona wind are measured. The velocity distribution and velocity characteristics of corona wind are measured by Pitot-tube and by hot-wire constant-temperature anemometer. Corona wind is visualized by Toepler schlieren measurements. Corona wind is also visualized by the injection of carbon dioxide generated mist into the flow. Heat transfer measurements with and without corona wind reaching an upward facing heat transfer surface are made.

Voltage-current characteristics of a corona triode are measured. The corona triode is used to generate corona wind and to control the magnitude of current which reaches the heat transfer surface. Heat transfer measurements in this corona triode geometry are made.

Conclusions are that corona wind may adequately be described by the Navier-Stokes equations of motion. The Coulomb ion drag forces transferred to the neutral gas background, create corona wind. The corona current is a function of the applied voltage and the electrode gap geometry. The average corona wind turns out to be proportional to the square root of the corona current. The corona wind velocity distribution is bellshaped with a maximum of about 5 m/s. The electrokinetic conversion efficiency is of the order of one percent. The enhancement of heat transfer by corona wind is significant. Heat convection enhancement by up to 90 percent are measured. The enhancement of convective heat transfer by corona wind blowing on a heat transfer surface turns out to be proportional to the 0.3 power of the corona current.

It turns out that the enhancement of convective heat transfer is only due to the augmentation of the hydrodynamic flow of the air. The corona wind is laminar, less turbulent than a mechanically created jet, has a small spread with a cross-section area of about 2x4 cm^2, and has a long reach of up to 25 cm which makes it superior to mechanically created jets for enhancement of heat convection by blowing towards heat transfer surfaces.

The Langmuir-Child equation for space charge limited current (SCLC) in vacuum is expressed in a general form in a gaseous media.

Kadete, H.
ENHANCEMENT OF HEAT TRANSFER BY CORONA WIND.
Faculty of Electrical Engineering, Eindhoven University of Technology, the Netherlands, 1987.
EUT Report 87-E-184

Address of the author:
Dr. Henry Kadete,
Department of Electrical Engineering,
University of Dar es Salaam,
P.O. Box 35131,
Dar es Salaam,
Tanzania

To my wife Chem-Chemi and son Camara for their understanding, constant encouragement, and for bearing with me during some extremely trying moments. The said two have been inspirational towards the completion of this work.

CONTENTS

SYMBOLS

N.B. Symbols in boldface are vectors.

UPPER CASE LETTER SYMBOLS

A	Area [m^2]
B	Constant
D	Diameter [m]
D_o	Optical transparency [percent]
D_e	Electrical current transparency of a grid [percent]
$\frac{D}{Dt}$	Substantive derivative, or hydrodynamic derivative. In the cartesian two coordinate system = $\partial/\partial t + u\partial/\partial x + v\partial/dy$
E	Electric field intensity [V/m]
E_b	Breakdown field strength between two parallel planes [V/m]
E_c	Onset corona field strength at surface of highly stressed electrode [V/m]
E_g	Electric field intensity between grid and anode of a corona triode [V/m]
E_o	Electric field intensity between cathode and grid, close to the grid in corona triode [V/m]
E	Electric field strength parallel to the x direction [V/m]
$\frac{dE}{dx}$	Gradient of the electric field intensity in the x direction [V/m^2]
F	Force [N]
F	Force acting in the x direction [N]
H	Magnetic field intensity [A/m]
I	Current [A]
I_c	Corona current from discharge electrode [A]
I_h	Current through the heating element [A]
I_p	Corona current collected at the plate [A]

I_s	Saturation corona current [A]
I_w	Corona current collected at the wires [A]
K	Mobility [m^2/Vs]
L	Length of an electric flux line [m]
M	Air mass flow rate [Kg/s]
N_a	Number of air molecules crossing a plane per second [s^{-1}]
N_i	Number of ions crossing a plane per second [s^{-1}]
P	Power [W]
P_h	Power consumed by a heating element [W]
P_{in}	Average input power [W]
Q	Charge per pulse [C]
R	Resistance [Ω]
R_{he}	Resistance of heating element [Ω]
R_h	Resistance of hot wire of anemometer probe [Ω]
R_o	Resistance of cold wire of anemometer probe [Ω]
R_{th}	Thermal resistance [$^oC/W$]
T	Temperature [^oC]
T_a	Ambient temperature [^oC]
T_{max}	Maximum temperature [^oC]
T_p	Temperature of plate [^oC]
T_s	Temperature at solid-gaseous interface [^oC]
$\frac{dT}{dn}$	Temperature gradient normal to a cross-section area considered [$^oC/m$]
$\left[\frac{dT}{dn}\right]_s$	Temperature gradient normal to a cross-section area considered at the surface [$^oC/m$]
ΔT	Temperature difference [^oC]
ΔT_c	Temperature difference between heated surface and ambient when corona wind is blowing at heated surface [^oC]
ΔT_n	Temperature difference between heated

surface and ambient when no corona wind is blowing at the surface [^{o}C]

$\frac{d\Delta T}{dt}$ The rate of change of the temperature difference [^{o}C/s]

U Scalar function

V Voltage [V]

V_a Voltage output of anemometer measuring unit [V]

V_f Potential between grid and anode of corona triode due to voltage of cathode [V]

V_c Corona inception voltage [V]

V_g Voltage applied to corona discharge gap [V]

V_{gc} Corrected potential between grid and anode of corona triode [V]

V_{gr} Voltage applied to grid [V]

V_o Voltage output of anemometer measuring unit at zero velocity measurement [V]

V_r Potential between biasing grid and anode for which anode current is zero in a corona triode [V]

$\frac{dV}{dx}$ Voltage gradient in the x direction [V/m]

W_a Kinetic energy of the corona wind [J/s]

W_e Electrical energy dissipated in the corona discharge per second [J/s]

W_i Work done on an ion in traversing the drift region [J]

X Flow resistance coefficient of a grid [percent]

LOWER CASE LETTER SYMBOLS

a	Distance between grid wires of corona triode [m]
a	Constant
a_c	Constant
a_o	Constant
b	Constant
b	Reduction factor [dimensionless]
c	Geometrical factor
c_h	Specific heat capacity of heat transfer surface [J/kg^{o}C]
d	Corona geometry spacing between cathode and anode [m]
d_g	Length between cathode and biasing grid in corona triode [m]
d_p	Length between cathode and plate [m]
d_w	Length between cathode and wires [m]
e	Electronic charge [1.609 x 10^{-19} C]
f	Force density [N/m^3]
f_x	Force density parallel to the x direction [N/m^3]
f_y	Force density parallel to the y direction [N/m^3]
g	Constant of acceleration due to force of gravity [m/s^2]
h	Convective heat transfer coefficient [W/m^2 ^{o}C]
h_c	Convective heat transfer coefficient from heated surface when corona wind is blowing at the surface [W/m^2 ^{o}C]
h_l	Height of light source image [m]
Δh_l	Reduced height of light source image [m]
h_n	Natural convective heat transfer coefficient [W/m^2 ^{o}C]
h_p	Manometric pressure measurement [m]
i_w	Instantaneous current to wires [A]

i_p	Instantaneous current to plate [A]
j	Current density [A/m^2]
j	Current density in the x direction [A/m^2]
j_o	Current density in corona triode between cathode and grid close to the grid [A/m^2]
j_O	Current density along axis of point-to-plate geometry measured at the plate [A/m^2]
j_p	Current density in corona triode between grid and anode [A/m^2]
j_s	Saturation corona current density [A/m^2]
j_ϕ	Current density at an angle ϕ from axis of point-to-plate geometry measured at the plate [A/m^2]
k	Thermal conductivity [W/m^{o}C]
k_f	Thermal conductivity in boundary layer [W/m^{o}C]
l	Length from biasing grid to anode in a corona triode [m]
m	Mass [kg]
m_a	Mass of one air molecule [kg]
m_i	Mass of one ion [kg]
n	Refractive index of a medium [dimensionless]
$\frac{\partial n}{\partial x}$	Gradient of refractive index in the x direction [m^{-1}]
p	Pressure [Pa]
p_m	Measured pressure [Pa]
$\frac{dp}{dx}$	Pressure gradient in the x direction [$Pa \cdot m^{-1}$]
Δp	Pressure difference [Pa]
Δp_m	Measured pressure difference [Pa]
q	Rate of heat transfer [W]
q_c	Rate of convective heat transfer [W]
q_k	Rate of conductive heat transfer [W]
q_{nr}	The net heat which is radiated away by a surface [W]

q_r	Rate of heat transfer by radiation [W]
r	Radial distance [m]
dr	Differential radial distance [m]
s	Spacing [m]
s_c	Spacing of combs [m]
s_w	Spacing of wires [m]
ds	Differential spacing [m]
t	Time [s]
t_p	Time in which power is consumed by heating element [s]
t_c	Control time [s]
dt	Differential time difference [s]
u	Air velocity parallel to the x direction [m/s]
u_{av}	Average velocity of corona wind [m/s]
u_{avc}	Average velocity of the corona wind in the central core [m/s]
u_{avo}	Average velocity of the corona wind in its outer region [m/s]
u_{avs}	Average space charge limited corona wind velocity [m/s]
u_f	Free stream average velocity of mechanically created wind from orifice [m/s]
$\mathbf{u}_i$	Ion velocity [m/s]
u_i	Ion velocity parallel to the x direction [m/s]
u(r)	Radial distribution of velocity parallel to the x direction [m/s]
u_{max}	Maximum velocity of corona wind parallel to the x direction [m/s]
u'	Velocity component to which anemometric probe is most sensitive [m/s]
Δu	velocity difference parallel to the x direction [m/s]

$\frac{du}{dx}$	Gradient of velocity u along the x direction [s^{-1}]
$\frac{d^2 u}{dx^2}$	Second derivative of velocity u in the x direction [$m^{-1}s^{-1}$]
$\frac{Du}{Dt}$	Substantive derivative of the velocity u [m/s^2]
v	Air velocity parallel to the y direction [m/s]
$\frac{dv}{dy}$	Gradient of air velocity v along the y direction [s^{-1}]
$\frac{d^2 v}{dy^2}$	Second derivative of the velocity v in the y direction [$m^{-1}s^{-1}$]
$\frac{Dv}{Dt}$	Substantive derivative of the velocity v [m/s^2]
x	Linear displacement in x direction of cartesian coordinate system [m/s]
x_p	Distance of anemometric probe below wires of EWS [m]
dx	Differential linear displacement [m]
$\frac{dx}{dt}$	Velocity in the x direction [m/s]
x,y,z	Cartesian coordinates [m,m,m]

GREEK SYMBOLS

α	Viscosity [Pa·s]
β	Temperature coefficient of Resistivity [$(^{o}C)^{-1}$]
χ	Conductor roughness factor [dimensionless]
δ	Relative air density [dimensionless]
ϵ	Electrostatic permittivity [F/m]
$\frac{\partial \epsilon}{\partial \rho_m}$	Variation of permittivity of medium with respect to the density distribution [Fm^2/Kg]
ϵ_o	Electrostatic permittivity of vacuum, 8.854188×10^{-12} F/m
ϵ_r	Relative permittivity of a medium [dimensionless]
ϕ	Angular displacement [degrees]
η	Dummy variable
κ	Constant
λ	Overheating ratio [dimensionless]
μ	Magnetic permeability [H/m]
$\frac{\partial \mu}{\partial \rho_m}$	Variation of magnetic permeability of medium with respect to the density distribution [Hm^2/Kg]
ν	Kinematic viscocity [m^2/s]
ψ	Focal length of schlieren head lens [m]
ρ_m	Mass density [Kg/m^3]
ρ_{mf}	Mass density of manometric fluid [Kg/m^3]
ρ	Charge density [C/m^3]
σ	Stefan's constant [$W(^{o}C^{-4})$]
τ	Time constant [s^{-1}]
υ	Light intensity [Lumens]
$\Delta\upsilon$	Light intensity difference [Lumens]

ζ	Efficiency [percent]
∇	$i\partial/\partial x + j\partial/\partial y + k\partial/\partial z$
Π	Trichel pulse repetition frequency [s^{-1}]
Ξ	Enhancement of convective heat transfer over natural convection [percent]

CHAPTER I INTRODUCTION

1.1 General Remarks

Heat transfer is an important part of many industrial processes. The enhancement of heating or cooling in an industrial process may create a saving in energy, reduce process time, raise thermal rating and lengthen the working life of equipment. Some processes are even affected qualitatively by the action of enhanced heat transfer.

Conventionally, convective heat transfer has been enhanced by mechanically created fluid jets or by air streams due to fan action. The jets are created by pumping a fluid through tubes or ducts to orifices.

The investment and maintenance costs of such heat transfer enhancement schemes are high, especially due to the costs of pumping equipment and the corrosive action of the moving medium to the pipes or ducts, especially at high temperatures. Also operational problems such as generation of noise, reduction of the possibility to view the heat transfer surface, and difficulty of cooling complicated geometries make conventional systems unsuitable in some cases.

A corona discharge on the other hand creates a jet which is variously known as corona wind, electric wind or electric aura. The corona wind, as this jet will be referred to henceforth, shows convective heat transfer enhancement over natural convection with very low investment and operating costs. Moreover a device to generate corona wind is very simple in design, robust, and easy to operate. Especially it can be operated silently without reducing the possibility to view the heat transfer surface, and can be constructed to cool even the most difficult geometrical configurations .

1.2 Background

The corona wind phenomenon has been known since the late 1600's as was first reported by Hauksbee [1] in the year 1709. This phenomenon later drew the attention of the likes of Newton, [2] Faraday, [3] and Maxwell [4]. Chattock [5] is the first one to have described quantitatively the mechanism of corona wind formation. Subsequently the mechanism of corona wind formation was treated extensively in the literature. [6-11]

On the other hand, studies of heat transfer enhancement by electrostatic fields started with Senftleben, [12] in 1931. Senftleben and several other subsequent researchers, [13-15] attributed an observed enhancement of heat transfer to convection caused by an electrostatic wind. The electrostatic wind was thought to be created by the motion of neutral gas molecules due to polarization forces which were thought to exist in the gas media. Although this effect is present it is too small to be of practical significance.

That corona wind as attributed by Chattock may be directly responsible for the enhancement of the transfer of heat across solid gaseous interfaces was first reported by Moss and Grey [16] in 1966 and later by others [17-26]. Appreciation of the effectiveness of heat transfer enhancement by corona wind in the late 1960's brought about an intense research to understand its mechanism thereafter. There now exist several patents which apply corona wind to enhance the rate of heat transfer. [27-36]

Presently industrial applications of corona wind enhanced heat transfer can be found in bread or cookie baking improvement, improvement of machining processes, simplification and improvement of arc welding, improvement of the quality of plasma arc depositions of hard coatings, and the reduction of wear of cutting

tools. [37, 38]

Other areas of industrial applications are foreseen in the cooling of semiconductor components in computers, cooling of glass windows and mirrors of gas lasers, curing of tobacco leaf wrappings of cigars, drying of paints, enhancement of heat transfer from dry heat exchangers of thermal power plants, and many others. [38]

However the heat transfer augmentation process had not yet been clearly explained because of the possible simultaneous involvement of more than one underlying physical mechanism. For example it was possible that the interaction of ionic current and the heat transfer surface is important in disrupting the gas flow boundary layer. It was possible that the corona wind characteristics are important. The corona wind may be turbulent, pulsating etc. The electrohydrodynamic mechanism of the corona wind had not always been properly formulated.

If the process of heat transfer enhancement by corona wind is better understood it may be optimized and possibly also the door may be opened to an even wider field of applications.

1.3 Scope

Fundamental concepts on heat transfer are studied. Empirical and theoretical equations of negative dc corona are summarized. Understanding of these equations leads to the explanation of the effect of the corona discharge geometry on corona wind and consequently on convective heat transfer. Fundamental concepts of electrohydrodynamics of the gas flow are also studied. A theoretical treatment of the corona wind mechanism is given. This treatment is developed from the classical equations of Chattock [5]. Navier-Stokes equations of motion and Bernoulli's energy equation along a streamline

have to be properly modified to describe the corona wind.

In the experimental work, a negative dc voltage is applied across a corona discharge geometry or electric wind system(EWS) to generate the corona wind. The corona wind is directed to a nearby heat transfer surface. The effect of the corona wind on heat transfer across the solid gaseous interface is measured. In some of the heat transfer measurements a corona triode has been used to create the corona wind and to control the magnitude of current which reaches the heat transfer surface. To help understand the heat transfer augmentation mechanism by the corona wind, electrical characteristics of the corona discharge geometry have been measured. Qualitative and quantitative studies of the corona wind have been made. These consist of velocity distribution measurements of the corona wind by Pitot-tube and hot-wire anemometer, flow visualization of the corona wind by schlieren method, and flow visualization by injecting carbon dioxide generated mist into the corona wind.

A correlation between the experimental measurements and the theoretical analysis is made wherever possible.

1.4 Organization of Work

The introduction outlines some general remarks on the subject of the thesis. The historical development of scientific activities related to the enhancement of convective heat transfer due to corona wind is also presented. The introduction concludes with the description of the scope and organization of the work. This introduction forms chapter I

Chapter II outlines the basic concepts on heat transfer, negative dc coronas, and the electrohydrodynamic principles governing the generation of the corona wind.

The part of my work on experimental measurements which forms chapter III outlines the diagnostic measurements on the corona wind. These include:

-measurements of the voltage-current characteristics of negative dc corona in a geometry which is used to generate corona wind.

-measurements of the velocity distribution of the corona wind by Pitot-tube.

-measurements of the velocity characteristics of the corona wind by constant-temperature hot-wire anemometer.

-flow visualization of the corona wind by Toepler schlieren method.

-flow visualization of the corona wind when carbon dioxide generated mist is injected in the corona wind.

-heat transfer measurements with and without corona wind.

-measurements of the voltage-current characteristics of the corona triode.

-heat transfer measurements with corona triode used to control the magnitude of current which is collected by the heat transfer surface.

Chapter IV consists of the conclusions. Areas in which further research may be undertaken are pinpointed.

CHAPTER II FUNDAMENTAL PRINCIPLES

2.1 Heat Transfer

There are three commonly known processes of heat transfer, namely conduction, convection, and radiation. [39-41]

2.1.1 Conduction

Heat transfer by conduction is achieved when high energy particles pass some of their kinetic energy of motion (translational, rotational, or vibrational) to low energy particles by direct collisions or by the drift of free electrons in the case of heat conduction in metals. This process of passing energy is distributed in all directions in a medium. Heat transfer by conduction is dominant in metallic and semi-metallic media. The distinguishing feature of conduction is that it takes place within the boundaries of a body, or across the boundary of a body into another body placed in contact with the first without an appreciable displacement of the matter comprising the body. Conductive heat transfer is governed by the empirical equation

$$q_K = -K \cdot A \cdot \frac{dT}{dn} \quad . \tag{1}$$

Where q_K is the heat energy flow per unit time, K is the thermal conductivity, A is the area through which heat is flowing and dT/dn is the temperature derivative normal to the surface area considered.

2.1.2 Radiation

Radiation is the heat transfer process by electromagnetic waves. Radiation occurs even without any material medium. It was stipulated by Stefan and Boltzman that the total energy carried away by the emission of radiation is proportional to the fourth power of the absolute temperature. The equation of heat transfer by radiation is given by

$$q_r = \sigma \cdot (273 + T)^4 \ , \qquad (2)$$

In this equation q_r is the energy emission per second per unit area, T is the temperature of the body in degrees Celcius, and σ is a property of the particular emitting surface known as Stefan's constant.

2.1.3 Convection

Convection is the heat transfer process in fluids. The heat transfer medium (fluid) moves from one place to another and carries the heat with it. The actual process of energy transfer from one fluid particle or molecule to another is still that of conduction, but the energy is transported from one point in space to another by the displacement of the fluid itself.

There are two types of convection, known as natural and forced convection. In natural convection the fluid motion is a result of the heat transfer. That is because heating or cooling of the fluid in contact with a heat transfer surface results into a change of fluid density. This change of fluid density produces a natural circulation in which the affected fluid moves off of its own accord past the heat transfer surface, the fluid that replaces it is similarly affected by heat transfer and

the process is continued. In forced convection fluid flows due to the influence of an external agency such as a fan, pump, or any means. The basic rate equation for convective energy exchange is given by

$$q_c = h \cdot A \cdot \Delta T \ . \qquad (3)$$

Here q_c is the rate of heat transfer between the heat transfer surface and the fluid, A is the area of contact, ΔT is the temperature difference between the heat transfer surface and the bulk of the fluid, and h is the convective heat transfer coefficient.

As already pointed out, the convective heat transfer process is associated with movement of fluid particles. There are two types of fluid flow. These are laminar and turbulent. In laminar flow the fluid particles move in an orderly layer-like manner. In this case the heat transfer normal to the direction of fluid flow is only by conduction. In turbulent flow the movement of the fluid is characterised by an irregular and chaotic mixing of fluid elements in all directions. Turbulent flow of the fluid in the direction normal to the heat transfer surface greatly enhances the rate of heat transfer when the surface and the fluid are at different temperatures.

If we neglect heat transfer by radiation, we can combine Eq.(1) and Eq.(3) at a solid gaseous interface across which heat is flowing to yield a relation between the temperature gradient inside a solid, and the temperature difference between the surface of the solid and the bulk of a fluid, $T_s - T_a$. We have

$$q_k = q_c \ . \qquad (4)$$

It follows that,

$$\left[\frac{dT}{dn}\right]_s = \frac{h}{K} \cdot \left[T_s - T_a\right] . \qquad (5)$$

2.1.4 Boundary Layer Theory

The layer of fluid adjacent to a solid surface has no relative motion parallel to the solid surface due to the viscosity. As one moves away from the solid surface however the velocity increases asymptotically to the free stream velocity value. A velocity boundary layer [42] is defined as the region where the parallel velocity to the surface is less than 99 percent of the free stream velocity value. Beyond the boundary layer viscocity effects are neglected.

Heat transfer across a velocity boundary layer is therefore mainly by the slower process of conduction. Disruption of the velocity boundary layer can tremendously enhance the rate of heat convection.

The forced convection heat transfer coefficient for a circular plate of diameter D exposed to an impinging radially uniform wind of free stream velocity u_f is given by [21]

$$h = \left[k_f/\pi^{1/4}\right] \cdot \left[\frac{u_f}{\nu \cdot D}\right]^{1/2} . \qquad (6)$$

Here k_f is the thermal conductivity in the boundary layer, and ν is the Kinematic viscocity of the fluid. It is assumed that the wind flows

over a width greater than D.

2.2 Negative dc corona

When a strong enough non-uniform electric field is created in air across an electrode geometry ionization takes place in the vicinity of the highly stressed electrode. If the resulting discharge does not lead to a full breakdown, and carries only a moderate current, the discharge is known as corona. Ions which have the same polarity as the highly stressed electrode are injected into the gap. These ions get repelled away from the highly stressed electrode. The forces acting on the ions are the well known Coulomb forces. In the ensuing motion towards the collector electrode, the ions collide with neutrals. In this way the ions transfer their directed momentum and part of their kinetic energy of motion to the neutrals. The thus created air flow is referred to as corona wind.

Negative dc corona rather than positive dc corona is preferred to create corona wind because at atmospheric pressure and for the electrode geometries considered negative dc corona is more stable [43]. Breakdown voltages for negative dc corona voltages occur at much higher voltages.

2.2.1 Mechanism and Characteristics

Negative dc corona phenomena have been intensely studied experimentally. A very extensive treatment of its mechanism and characteristics can be found in books such as by Loeb, [11] Cobine, [44] Nasser, [45] Goldman, [46] and a host of others. A good summary of negative corona characteristics for a point-to-plate geometry can be found in a paper by Lama. [47]

For short gap lengths there is sparkover directly

whenever any discharge activity occurs. For longer gap lengths the transition will be from a pulsating discharge referred to as Trichel pulses directly to sparkover. For even longer gap lengths the transition will be from Trichel pulses to a continuous glow to sparkover. Fig. 1 shows the different discharge modes for a point-to-plate geometry at atmospheric pressure.

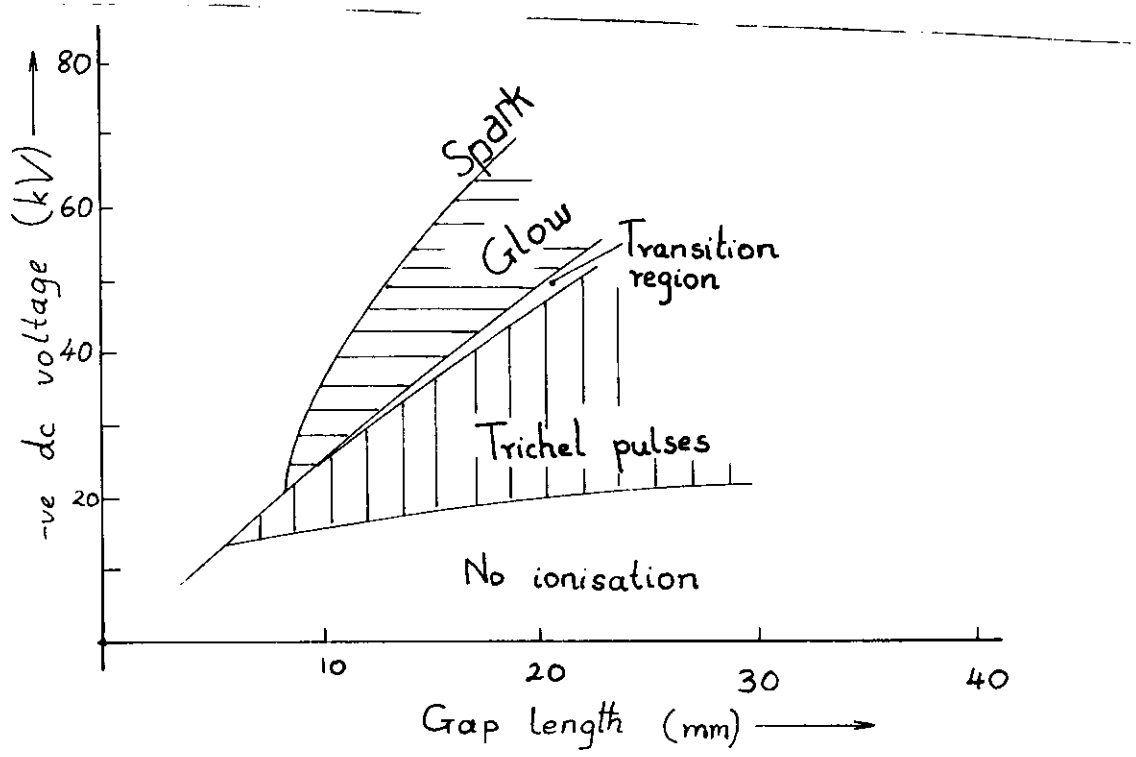

Fig. 1: Negative dc voltage point-to-plate breakdown and corona characteristics.

Depending on gap length and voltage across a point-to-plate geometry, the negative corona discharge is normally pulsating or a continuous reddish glow. On wires the corona appears as reddish glowing spots. The number of spots increases with the current. Four distinct regions of the discharge can be visually identified at the cathode of a point-to-plate geometry, namely the Crookes dark space, the negative glow, the

Faraday dark space, and the positive column. Towards breakdown the positive column has a centrally placed spike extending towards the anode. The visual form of a negative corona discharge is shown in Fig. 2.

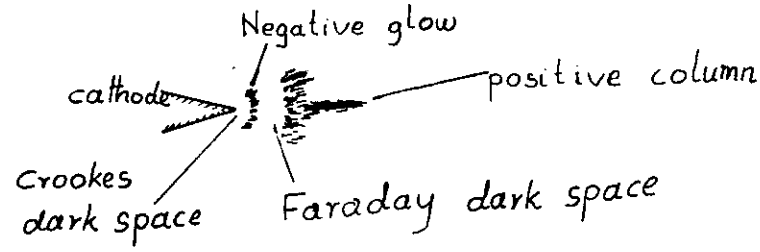

Fig. 2: Visual form of negative corona discharge in a point-to-plate geometry.

A model of the Trichel pulse formation was developed by Loeb [11]. In time sequence, the pulse is initiated by an electron ejected from the cathode surface by some mechanism such as field emission or positive ion bombardment, and multiplies by Townsend ionization. The positive ions left in the wake of the electron avalanche serve to increase the ionization field, leading to a rapid build up of the current. The positive ions further provide an additional source of electrons through bombardment of the cathode surface.

The electron avalanche is choked off in a very short time by the negative space charge which forms by electron attachment just outside the ionization region and which reduces the field in that region below the level required for ionisation. The discharge activity then stops

until the negative space charge has drifted in the electric field over a sufficient distance, referred to as clearing distance. The time interval involved is correspondingly referred to as the clearing time, for the field to regain its critical value.

A typical Trichel current pulse waveform has a very fast risetime in the order of nanoseconds often followed by two exponential decays with different time constants [48,49] as is shown in Fig. 3.

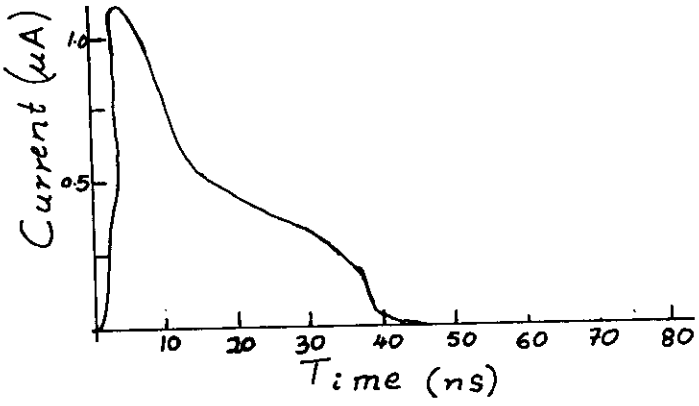

Fig. 3: Typical Trichel pulse waveform.

The fast risetime and high amplitude of the Trichel pulse current waveform is due to the motion and avalanche growth of the electrons in the high field region around the cathode. The first decaying exponential part of the Trichel pulse current waveform is determined by the motion of electrons in a reduced electric field region before attachment and the second decaying exponential part is determined by the motion of the positive ions towards the anode. The last part of the pulse is due to the motion of the negative ions, after the positive ions reach the cathode, which takes place in the low electric field region near the anode. Current is then very small.

The above description of a Trichel pulse is however still a matter of intense discussions.

The ionisation regions contain very little net space charge. The low field drift region is usually completely dominated by the negative space charges whose field will always reduce the Laplacian field in the ionisation region and enhance it near the plate as is shown in Fig. 4.

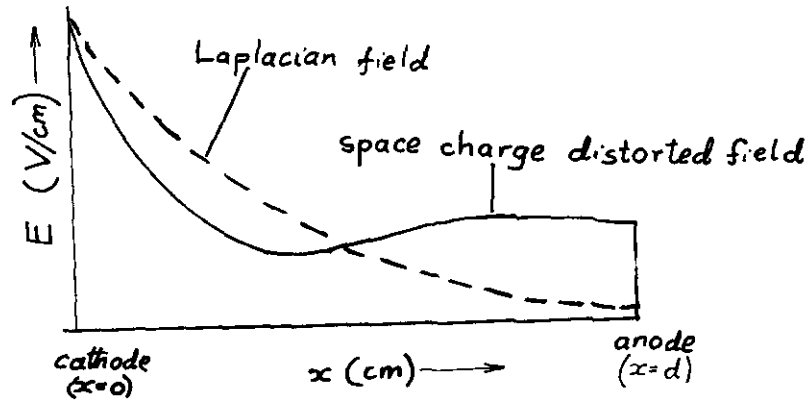

Fig.4: Field distortion by space charge.

2.2.2 Fundamental Equations

Well known empirical relationships governing Trichel pulses are:

(i) The time averaged corona current I_c, and the Trichel pulse repetition frequency Π, are linearly related for a given electrode gap configuration. The constant of proportionality is the charge per pulse Q.

$$I_c = Q \cdot \Pi \ . \qquad (7)$$

(ii) The charge per pulse depends on the shape of the discharge point, but is independent of the corona current, the applied gap voltage and gap length. If the

discharge electrode is a hemispherical cap of radius r, Q is only a function of r

$$Q = f(r). \tag{8}$$

(iii) The Trichel pulse repetition frequency Π is observed to follow the equation

$$\Pi = \frac{cV_g(V_g - V_c)}{rd^2}, \tag{9}$$

where c is a geometrical factor, r is the radius of the cathode, and d is the spacing between the cathode and anode. The voltages V_g and V_c are the voltage applied between the electrodes and the voltage for onset of corona respectively.

The ac corona onset field strength E_c at the surface of the highly stressed electrode of a coaxial cylinder geometry was found empirically [50] to be

$$E_c = E_b \cdot x \cdot \delta \cdot [1 + c/(\delta r)^{1/2}] \text{ KV(peak)/cm}. \tag{10a}$$

Here E_b is the breakdown field strength between two parallel planes, x is a factor which takes into account the roughness of the surface and c is a constant which depends on the electrode gap geometry. The relative air density is denoted by

$$\delta = \frac{2.94 \cdot 10^{-3} \cdot p}{273 + T}.$$

The atmospheric pressure is denoted by p in Pascals, and the temperature in degrees Celsius is denoted by T.

More recent empirical formulas which have been experimentally deduced for the corona onset field strength between coaxial cylinders are [51]

$$E_c = 23.8\left[1 + \frac{0.67}{r^{0.4}}\right] \text{ kVcm}^{-1}, \tag{10b}$$

and [52]

$$E_c = 24.5\left[1 + \frac{0.613}{r^{0.4}}\right] \text{ kVcm}^{-1} . \tag{10c}$$

Here r is the radius of the inner cylinder measured in meters. Equation (10b) and Eq. (10c) are in close agreement. A theoretical derivation of Peek's formula Eq.(10a) has also been given [53].

The corona discharge current I_c was empirically determined [54, 55] to obey the relationship

$$I_c = cKV_g(V_g - V_c) . \tag{11}$$

Here c is a constant which depends on the electrode gap geometry, V_g is the voltage applied between the electrodes, V_c is the voltage for onset of corona, and K is the mobility of the unipolar corona space charge in the drift region. For coaxial cylinders the constant c was later theoretically derived to be

$$c = \frac{8 \cdot \pi \cdot \epsilon_o}{d^2 \cdot \text{Ln}[d/r]} .$$

Where ϵ_o is the permittivity of free space, d is the interelectrode spacing and r is the radius

of the inner cylinder.

More exact equations for cylindrical coronas have been developed [56, 57]. Theoretical derivations of the Townsend current equations have also been made [58, 59].

The flow of current in the drift region of the corona discharge is governed by Poisson's equation, and the continuity equation. Poisson's equation is

$$\nabla \cdot E = \frac{\rho}{\epsilon_0} \quad . \tag{12}$$

Where

$$E = -\nabla V \quad .$$

The electric field is E, the local voltage is V, and ρ is the ion charge density.
The continuity equation is, for a stationary situation ($\partial\rho/\partial t = 0$)

$$\nabla \cdot j = 0 \quad , \tag{13}$$

Where

$$j = \rho u_i \, .$$

$$u_i = KE.$$

The corona current density is j, the ion velocity is u_i, and the ion mobility is K.
It follows from the continuity equation that

$$\nabla \cdot j = \nabla \cdot \rho u_i = \rho \, \nabla \cdot u_i + u_i \cdot \nabla \rho = 0 \quad .$$

Therefore,

$$\mathbf{u}_i \cdot \nabla \rho = -\rho \nabla \cdot \mathbf{u}_i .$$

Since,

$$\frac{D\rho}{Dt} = \mathbf{u}_i \cdot \nabla \rho \quad ,$$

$$\frac{D\rho}{Dt} = -\rho \, \nabla \cdot \mathbf{u}_i \quad .$$

$$= \frac{-K\rho^2}{\epsilon_o} \quad . \tag{14}$$

Where D/Dt is the hydrodynamic differential operator. Eq.(14) is used to derive Eq.(16).

For a point-to-plate geometry the current density distribution j at the plate obeys the empirical Warburg's law [60]

$$j_\phi = j_o \cdot \cos^5\phi \quad . \tag{15a}$$

$$\tan\phi = r/d \quad . \tag{15b}$$

For $\phi \leq 60^o$.

Where j_ϕ is the corona current density on the plate at any point ϕ degrees from the corona geometry axis and j_o is the current density at the plate along the corona geometry axis, and d is the point-to-plate spacing.

There is a fundamental saturation current density

j_S along any field line of length L crossing a gap of voltage V_g derived by Sigmond [61] from Eq. (14).

$$j_S = \frac{K \cdot \epsilon_o \cdot V_g^2}{L^3} \quad . \tag{16}$$

Here K is the ion mobility.

The total corona current I_c is given by

$$I_c = 2\pi \int jrdr \quad . \tag{17a}$$

From Eq. (15a),

$$\frac{d\phi}{dr} = \frac{\cos^2 \phi}{d} \quad . \tag{17b}$$

If we substitute Eq. (15a), Eq. (15b), and Eq. (17b) into Eq. (17a) we have,

$$I_c = 2\pi \int j_o \cos^5\phi \; d \tan\phi \; \frac{d}{\cos^2 \phi} \, d\phi$$

$$I_c = -2\pi d^2 \int j_o \cos^2 \phi \; d(\cos\phi) \quad . \tag{17c}$$

If we substitute d for L in Eq. (16) we

obtain j_o which we now use in Eq.(17c) to obtain the total point-to-plate saturation corona current I_s.

$$I_s = -2\pi d^2 \int_0^{60^o} \frac{K\epsilon_o V_g^2}{d^3} \cos^2 \phi d(\cos\phi) \quad .$$

$$I_s \approx \frac{2K\epsilon_o V_g^2}{d} \quad . \tag{17d}$$

Observed current densities or currents in excess of Eq.(17d) invariably imply either ions (electrons) of higher mobility than anticipated or bipolar conduction phenomenon like streamers.

2.3 Nature of Corona Wind

The equation for the electromagnetic forces in a gaseous dielectric is analyzed. A dominant term is deduced. The hydrostatic equilibrium condition is studied during corona. The conditons for breakdown of the hydrostatic equilibrium are summarized. The Navier-Stokes equations of motion are deduced for the corona wind. Bernoulli energy equation along a streamline is deduced for the corona wind. Also an expression for the electrokinetic energy conversion efficiency in corona discharge is deduced.

2.3.1 Electric Forces

It is possible to write a single general expression for the forces of electric origin in a dielectric medium. The total force per unit volume is [62, 63]

$$\mathbf{f} = \mathbf{j}\times\mu\mathbf{H} - \tfrac{1}{2}H^2\nabla\mu + \tfrac{1}{2}\nabla\left[H^2\rho_m\frac{\partial\mu}{\partial\rho_m}\right]$$

$$+ \rho\mathbf{E} - \tfrac{1}{2}E^2\nabla\epsilon + \tfrac{1}{2}\nabla\left[E^2\rho_m\frac{\partial\epsilon}{\partial\rho_m}\right] . \qquad (18)$$

Here $\mathbf{j}$ is the free current density in a dielectric material, μ is the permeability of the medium, $\mathbf{H}$ is the magnetic field intensity, ρ is the free charge density, $\mathbf{E}$ is the electric field intensity, ϵ is the electrostatic permittivity, and ρ_m is the mass density of the medium. The first and fourth terms are recognized as the usual free current, and free charge force densities. Their sum is the Lorentz force equation. The second and fifth terms are the Korteweg-Helmholtz polarization force densities. The third and sixth are the electromagnetic strictive forces whose effect is to increase static pressure in compressible flows.

The magnetic field intensity in our setups is negligible. Therefore the first term is neglected. The variation of magnetic and electrical properties due to temperature and composition variations of gaseous dielectrics is negligible. Therefore the second and fourth terms are neglected. The third and sixth terms are not to be considered since both the relative permittivity ϵ_r and the relative permeability μ_r of air have values close to unity.

The only significant force density is due to the free-charge Coulomb forces. Eq.(18) simplifies to

$$\mathbf{f} = \rho\mathbf{E} . \qquad (19)$$

2.3.2 Hydrostatics

The hydrostatic equation which is applicable in a perfectly symmetrical corona discharge configuration for instance in a cylindrical geometry where no electrical wind is generated is

$$\mathbf{f} = \nabla p. \tag{20}$$

Where $\mathbf{f}$ is the volume force transmitted by collisions of ions with neutrals, and p is the generated static pressure gradient which balances the electric volume force density.

If we resolve Eq.(20) in only one dimension it simplifies to

$$f_x = dp/dx \ . \tag{21}$$

From Eq.(19)

$$f_x = \rho E \ .$$

$$= \frac{\rho u_j}{K} \ .$$

$$= j/K. \tag{22}$$

Where ρ is the charge density, u_j the ion drift velocity, K the ion mobility, and j the ion current density.
Combining Eq.(21) and Eq.(22)

$$dp/dx = j/K \ . \tag{23}$$

For a completely symmetrical configuration , and where the volume charge density distribution is also symmetrical the Coulomb force density serves only to increase the pressure. This is possible for example in a coaxial cylinder corona geometry where a hollow presure profile would be formed.

The necessary condition for the fluid to stay at rest is that $\nabla \times \mathbf{f}$ equals zero in the whole region. In a point-to-plate corona discharge this condition is not fulfilled due to lack of symmetry of the discharge. We find that $\nabla \times \mathbf{f} = \nabla \times (\rho \mathbf{E}) = \rho \nabla \times \mathbf{E} + (\nabla \rho) \times \mathbf{E} \neq 0$. The factor $(\nabla \rho) \times \mathbf{E}$ is not zero especially at the boundaries of the discharge. [64]

2.3.3 Hydrodynamics

A disturbance of the hydrostatic equilibrium will result in a flow condition, the corona wind. The disturbance may be due to a lack of field symmetry, or due to the charge density distribution which would be more strongly felt at higher voltages.

Let us consider the corona wind. For simplicity it is represented by a two dimensional laminar flow as shown in Fig. 5.

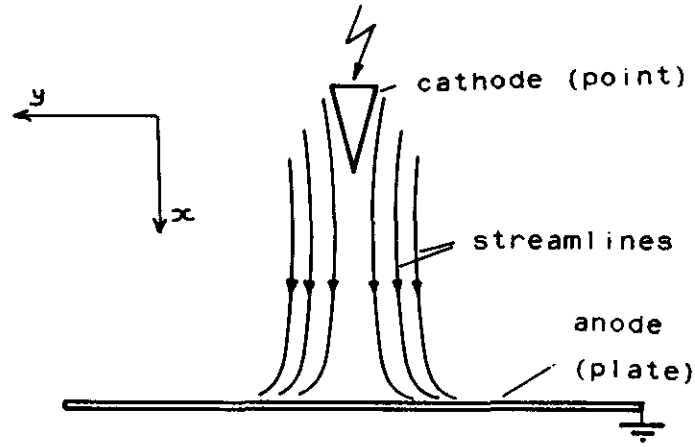

Fig. 5: Two dimensional laminar flow of the corona wind

We shall consider the flow to consist of a boundary layer in the mixing region, [65] where viscosity may not be neglected, and a central core in which we may neglect viscosity.

The Navier-Stokes equations of motion applied in the central core simplify to

$$\rho_m \frac{Du}{Dt} = f_x.$$

$$\rho_m \frac{Dv}{Dt} = f_y. \qquad (24)$$

Where D/Dt is the hydrodynamic differential operator, u is the air velocity parallel to the x-axis, v is the air velocity parallel to the y-axis, f_x is the Coulomb force density parallel to the x-axis, and f_y is the Coulomb force density parallel to the y-axis and ρ_m is the air mass density. The continuity equation reduces at low and stationary air velocities to the condition

$$\frac{du}{dx} + \frac{dv}{dy} = 0 . \qquad (25)$$

If we neglect f_y, Eq.(24) reduces to

$$\rho_m u \cdot \frac{du}{dx} = f_x . \qquad (26)$$

Integrating along a streamline over a distance d with the assumption that at x = 0, u = 0 and if we use η as a dummy variable in the left hand side below, we have

$$\int_0^u \rho_m \eta \, d\eta = \int_0^d f_x \, dx \, .$$

$$\frac{\rho_m \cdot u^2}{2} = f_x \cdot d \, . \qquad (27)$$

In other words the directed motion kinetic energy gained along a streamline equals the work done by the Coulomb force along that streamline.

Combining Eq.(22) and Eq.(27) we immediately see that

$$\frac{\rho_m \cdot u^2}{2} = \frac{j \cdot d}{K} \, .$$

At the plate we may say that

$$\frac{\rho_m \cdot u_{av}^2 \cdot A}{2 \cdot d} \approx \frac{I_c}{K} \, .$$

Where u_{avc} is the spatially averaged velocity of the corona wind in the central core of cross-section area A, and d is the distance between the cathode and the plate. It follows that, the average velocity in the central core is

$$u_{avc} \approx a_c \cdot \sqrt{I_c} \quad , \tag{28}$$

with

$$a_c = \sqrt{\frac{2 \cdot d}{\rho_m \cdot K \cdot A}} \quad .$$

In fact the wind blows over a larger area because of the viscosity forces which drag the surrounding air along with the central core considered above. This dragging force has a slowing effect to the velocity of air in the central core. The slowing effect however is small and difficult to ascertain, therefore it is neglected.

In the mixing region outside the core, the effect of viscosity is dominant. The Coulomb force density f_x is negligible. Since the whole medium is at atmospheric pressure the Navier-Stokes equation of motion takes the form

$$u \cdot \frac{du}{dx} = \nu \cdot \left[\frac{d^2 u}{dx^2} + \frac{d^2 u}{dy^2} \right] \quad .$$

Here ν is the Kinematic viscosity.
If we assume that the frictional force dragging the surrounding air is a fraction of the electrical driving force for the central part of the jet then the above expression may be rewritten as

$$u \frac{du}{dx} = b \cdot f_x \quad .$$

Here b is a constant. The spatially averaged velocity of the corona wind in the outer region may similarly be deduced to be

$$u_{avo} = a_o \cdot a_c \sqrt{I_c} ,$$

where u_{avo} is the spatially averaged corona wind velocity in the outer region and a_o is a constant.

The corona wind velocity averaged over the entire area may therefore be denoted by

$$u_{av} = a \cdot a_c \sqrt{I_c} . \qquad (29a)$$

Here u_{av} is the spatially averaged corona wind velocity and a is a constant.

To determine the space charge limited corona wind velocity we substitute I_s given by Eq.(17d) for I_c in the above expression. The average space charge limited corona wind velocity u_{avs} is therefore denoted by

$$u_{avs} = a \cdot \sqrt{\frac{2d}{\rho_m K A} \cdot \frac{2K\epsilon_o V_g^2}{d}} ,$$

$$= 2a \sqrt{\frac{\epsilon_o}{\rho_m A}} \cdot V_g \qquad (29b)$$

This equation indicates that for practical parameters $\epsilon_o = 8.85 \times 10^{-12}$ F/m, $\rho_m = 1.293$ kg/m^3, A = 8x10-4 m^2, and V_g = 20 kV velocities of the order 3.7 m/s should be expected.

2.3.4 Bernoulli Energy Equation

Bernoulli's energy equation along a streamline takes the form

$$p + \frac{\rho_m \cdot u^2}{2} - U = \text{Constant}, \qquad (30a)$$

where U is a scalar function whose gradient represents a conservative force acting along the streamline. In our case this force is given by the Coulomb force density, since we neglect gravitational force, magnetic force, and electric polar forces. Bernoulli equation now takes the form

$$p + \frac{\rho_m \cdot u^2}{2} - \int_1^2 \rho E dx = \text{Constant}. \qquad (30b)$$

Since the ambient pressure impresses itself on the jet, p is constant along the streamline and is equal to the ambient pressure.

2.3.5 Electrokinetic Energy Conversion Efficiency

The efficiency with which electrical energy is transformed into directed motion in the drift region of a corona discharge may be estimated as follows:
The total work done on an ion in traversing the drift region is given by

$$W_i = e\int E dx \approx eEd.$$

A large part of W_i ends up as random kinetic energy (heating) of the gas molecules; to calculate what fraction of W_i is converted into directed kinetic energy we consider the momentum equation.

The momentum gained by the air medium due to collisions with this ion is

$$\Delta(mu)_{gas} = \int F dt.$$

$$= e\int E\frac{dt}{dx}dx \ .$$

$$= e\int \frac{E}{KE}dx.$$

$$= \frac{ed}{K} \ .$$

Here m is the mass of air moving with velocity u due to the force F which acts on the air mass. The force F acts directly on the ion, but is completely transferred to the air mass, because the ion comes to a steady drift velocity in the background gas.

The kinetic energy gained by the surrounding air in its directed motion is

$$\Delta(\tfrac{1}{2}mu^2) \approx \tfrac{1}{2} \cdot \frac{ed}{K} \cdot u \ .$$

The electrokinetic efficiency therefore is

$$\xi \approx \frac{\tfrac{1}{2} \cdot e \cdot d \cdot u/K}{e \cdot E \cdot d}$$

$$\approx \tfrac{1}{2} \cdot \frac{u}{u_i} \quad . \tag{31}$$

The electrokinetic efficiency is very low, since $u_i \approx$ 200 times u. Most of the energy in the drift region is expended as heat and some energy is expended in inelastic collisions in the ionisation region.

In liquids where ions experience much more friction u_i and u are approximately equal. Clearly flow is generated more efficiently in that case. However because of low ion mobilities in liquids, the space charge limited currents are very small which still make the resulting fluid velocities small.

CHAPTER III EXPERIMENTAL MEASUREMENTS

3.1 Voltage-Current Characteristics of dc Corona

Voltage-current characteristics of a point-to-plate geometry and an electric wind system (EWS) are determined. Current measurements are made to determine the relative magnitudes of corona current to the wires I_w and the corona current to the plate I_p in an EWS. Some time resolved measurements of these currents are made. Equipotential line distributions are plotted for a point-to-plate geometry and EWS by a digital computer technique based on the Finite Element Method. The electrical characteristics will be correlated to other diagnostic measurements like velocity and heat transfer measurements. The EWS employs a multi-point comb as the cathode and two grounded wires as the anode. With such an electrode configuration a heat transfer surface may be positioned behind the wires at some distance from the cathode.

3.1.1 Principles of Measurements

The time averaged voltage-current characteristics of the EWS are determined by use of a circuit shown in Fig. 6. Voltage-current characteristics for a point-to-plate geometry are determined by simply removing the wires of the EWS in the experimental setup.

A negative high dc voltage is applied to the comb (or to a single point) by a Wallis type power supply rated at 0-30 KV, 0-1 mA, via a 2 MΩ current limiting resistor. A 4000 pF, 20 KV dc smoothing capacitor is connected in parallel with the dc power supply circuit.

Voltages are measured by a highly accurate Singer electrostatic voltmeter with four voltage ranges, 0-5, 0-10, 0-25, and 0-50 KV. The time averaged corona currents are measured by sensitive Keithley electrometers A_w and A_p, type 610B and 610C with current ranges down to 10^{-14} A . The current meters are connected in the ground connection of the wires and the ground connection of the plate.

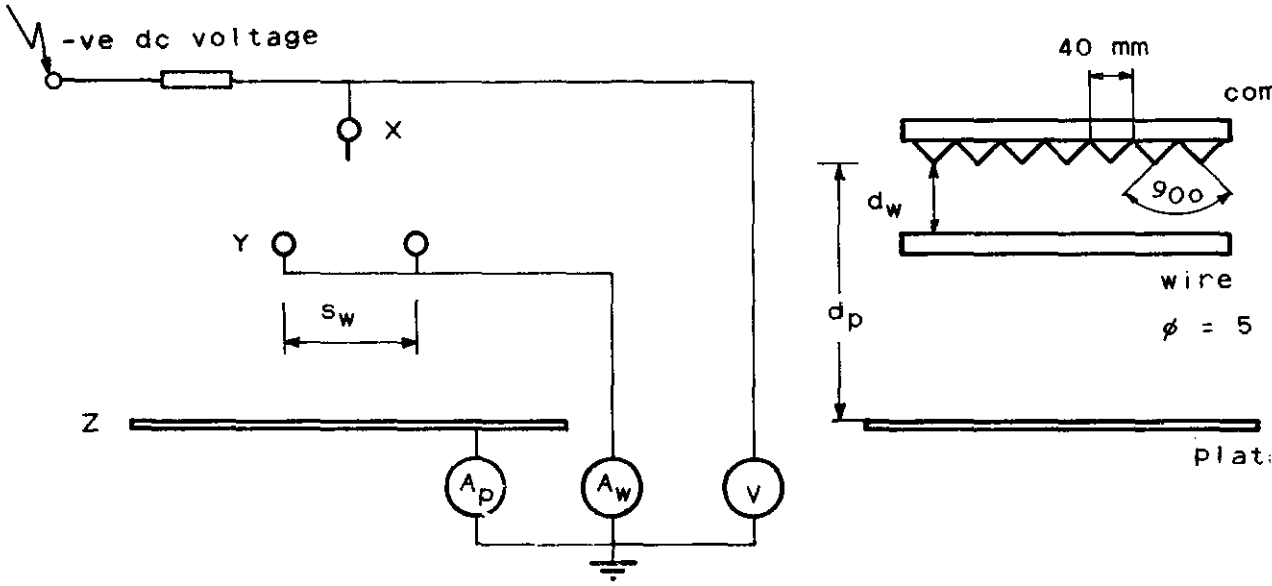

Fig. 6: Experimental circuit to determine the time averaged currents (I_c, I_w, I_p) vs gap voltage (V_g) characteristics of the EWS.
X = Cathode: one point or a multi-point comb.
Y = Anode: two grounded wires.
Z = Anode: grounded flat plate.

The circuit of Fig. 7 is used to determine the corona current waveforms in an EWS by measurement of the voltage waveforms across the 10 KΩ resistors. These voltages are fed into the input stages of a dual beam Tektronix oscilloscope type 556 having a frequency response of 0-20 MHz. The input coaxial cable to the oscilloscope has a characteristic impedance of 50 Ω, which means that parallel to the 10 KΩ measuring resistor a capacitance of l x100 pF is present, where l is the length of the coaxial cable. In order to determine the corona current waveforms in a point-to plate geometry the wires of the EWS are removed.

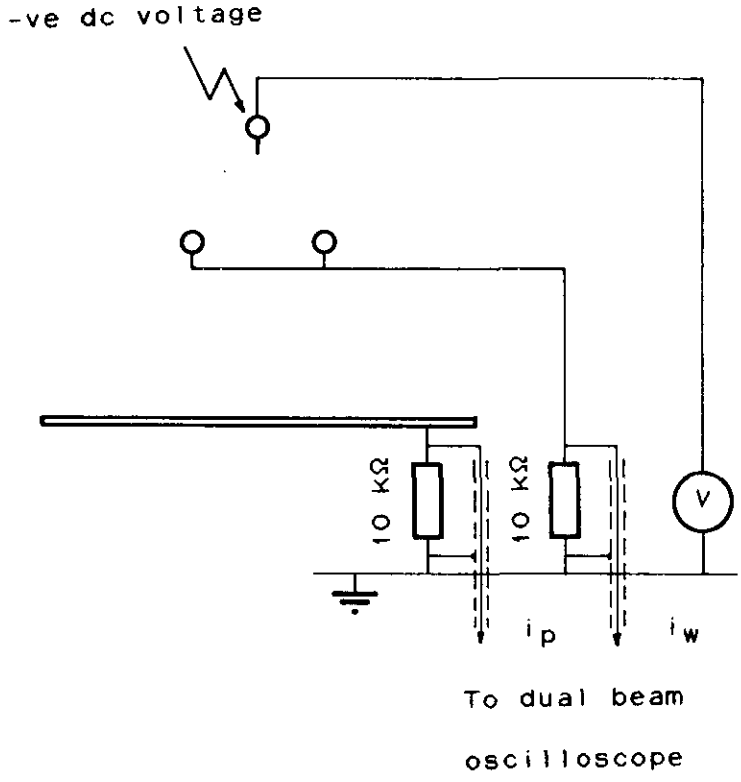

Fig. 7: Experimental circuit to determine the corona current waveforms $i_w(t)$ and $i_p(t)$.

3.1.2 Experimental Results and Discussions

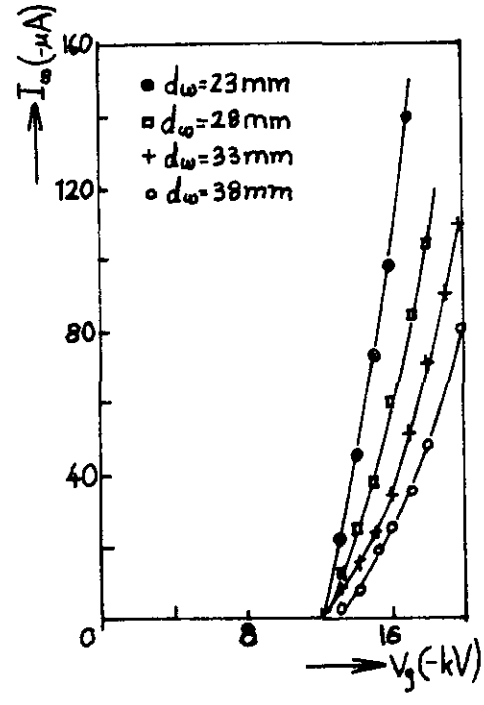

Fig.8: Current (I_w) vs gap voltage (V_g) for EWS.
Spacing between wires s_w = 10 mm.
Distance between cathode and plate d_p = 83 mm.
d_w = Distance between cathode and wires.
The cathode has 15 points.

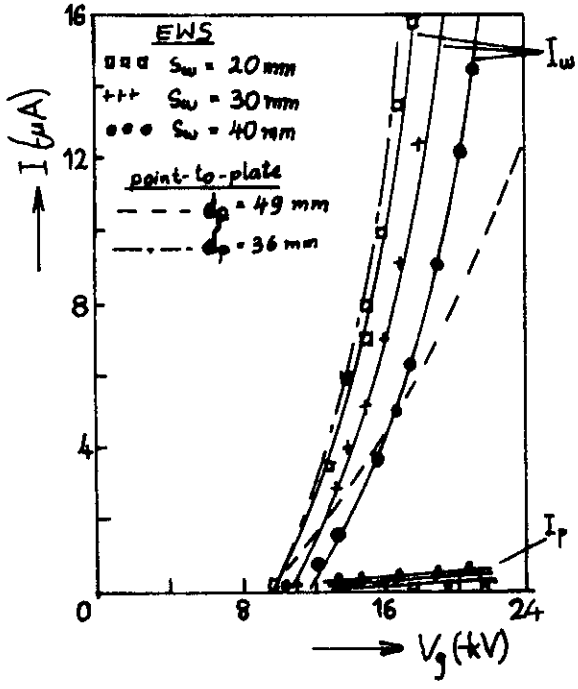

Fig. 9: Currents (I_w and I_p) vs gap voltage (V_g) for EWS and point-to-plate geometry.
EWS:
Distance between
cathode and wires d_w = 36 mm.
Distance between
cathode and plate d_p = 49 mm.
s_w = Spacing between wires.
The cathode has one point.

Fig. 8 and Fig. 9 show that the current to the wires can still be approximated by the classical corona current equation of Townsend, Eq. (11).

From Fig. 9 we see that the current to the plate

I_p is a very small proportion of the corona current I_c. Most of the corona current is collected by the wires. The small amount of the corona current which reaches the plate might be due to the corona wind drag force on the ions. A change in the electrode positions by variation of d_w, s_w, or d_p results in a change of the repetition frequency of the Trichel pulses Π according to Eq. (9) and because also the geometrical factor c changes in Eq. (9). A change in Π results in a change of I_c according to Eq. (7).

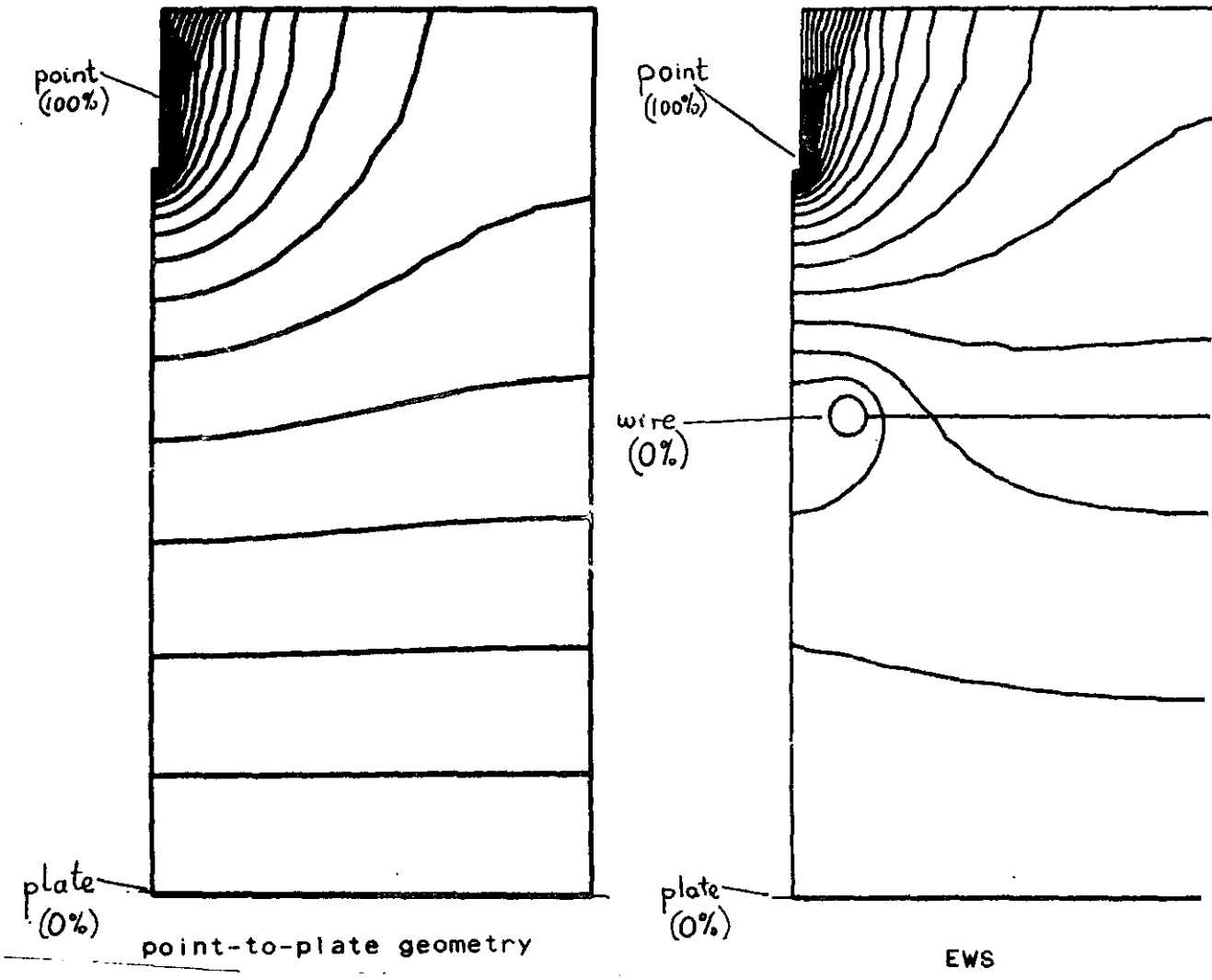

Fig. 10: Equipotential plots at 5 percent steps.

From the plots of equipotential lines in Fig. 10 we see that the wires strongly modify the configuration of the equipotential line distribution of a point-to-plate electrode gap. Most of the field lines from the ionisation region terminate at the wires in an EWS, we can therefore say that the effective gap length of the corona geometry is reduced; which leads to higher corona currents in the EWS, compare the space charge limited currents of Eq.(16).

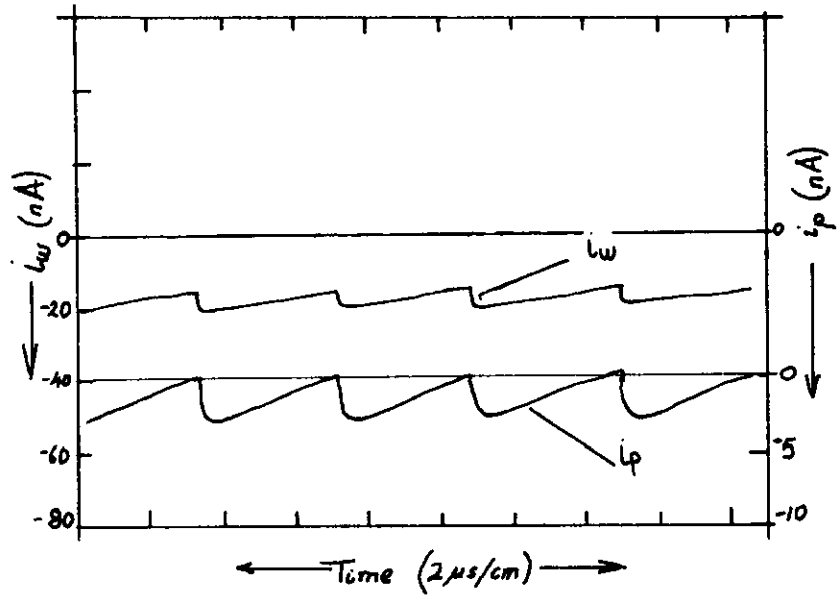

Fig. 11: Corona current waveforms (i_w and i_p) of EWS.
The cathode has one point only.

The oscillograms of Fig. 11 show the already discussed Trichel pulse current waveforms i_w and i_p. The current i_p is due to the capacitive coupling between the wires and the plate. The fast Trichel pulse is only measured with a poor frequency response because of the cable capacitance parallel to the 10 kΩ measuring resistors.

3.2 Pitot-Tube Velocity Measurements

The velocity distribution of the corona wind is determined by Pitot-tube measurements [66, 67] in an initial attempt to understand the hydrodynamic characteristics of the corona wind.

3.2.1 Principles of Measurements

Bernoulli's equation along a streamline, Eq.(30b) reads

$$p + \frac{\rho_m u^2}{2} - \int \rho E dx = \text{Constant} ,$$

in which the dynamic pressure is

$$\Delta p = \frac{\rho_m u^2}{2} . \qquad (32)$$

Since the Pitot-tube is positioned behind a grounded grid, the charge density distribution ρ is zero near the plane where the velocities are measured and therefore the last term on the left hand side of Eq.(30b) may be neglected.

The dynamic pressure can be calculated from measurements with a Pitot-tube according to the equation

$$\Delta p = \rho_{mf} \cdot g \cdot h_p . \qquad (33)$$

Here ρ_{mf} is the density of the fluid in the manometer used with the Pitot-tube, g is the acceleration due to gravity, and h_p is the difference

in the levels of the two fluid columns in the manometer. Water is used as the manometric fluid.

Therefore

$$u = \sqrt{\frac{2 \cdot \Delta p}{\rho_m}} \quad . \tag{34a}$$

Combining Eq. (33) and Eq.(34a) we obtain

$$u = \sqrt{\frac{2\rho_{mf} \cdot g \cdot h_p}{\rho_m}} \quad . \tag{34b}$$

The spatially resolved velocity distribution may be obtained experimentally from spatial measurements of the pressure increase at the tip of the Pitot-tube.

To enable mesurements of the corona wind velocity in a point-to-plane geometry a grid is used instead of a solid plate for the anode. The grid has square wire meshes of 59.17 percent optical transparency.

When the Pitot-tube is positioned behind the grid, the dynamic pressure measurements have to be corrected for the pressure loss across the grid by a factor X as given by Jonas [68]

$$X = 0.15(1/D_o^4-1)/u + 0.5(1/D_o^2-1) \quad . \tag{35}$$

Here X(percent) is the resistance coefficient of the grid, D_o(per unit) is the optical transparency of the grid, and u(m/s) is the velocity measured behind the grid.

The corrected dynamic pressure Δp which has to be used in Eq.(34a) is therefore

$$\Delta p = \left[1 + \frac{X}{100}\right] \cdot \Delta p_m ,$$

where Δp_m is the measured value of the dynamic pressure behind the grid.

3.2.2 Experimental Results

Fig. 12 shows the spatial distribution of the corona wind velocity for several cases. Fig. 13 shows a normalized spatial distribution of the corona wind and a comparison is made with the Warburg's current density distribution law given by Eq.(15), for a point-to-plate geometry.

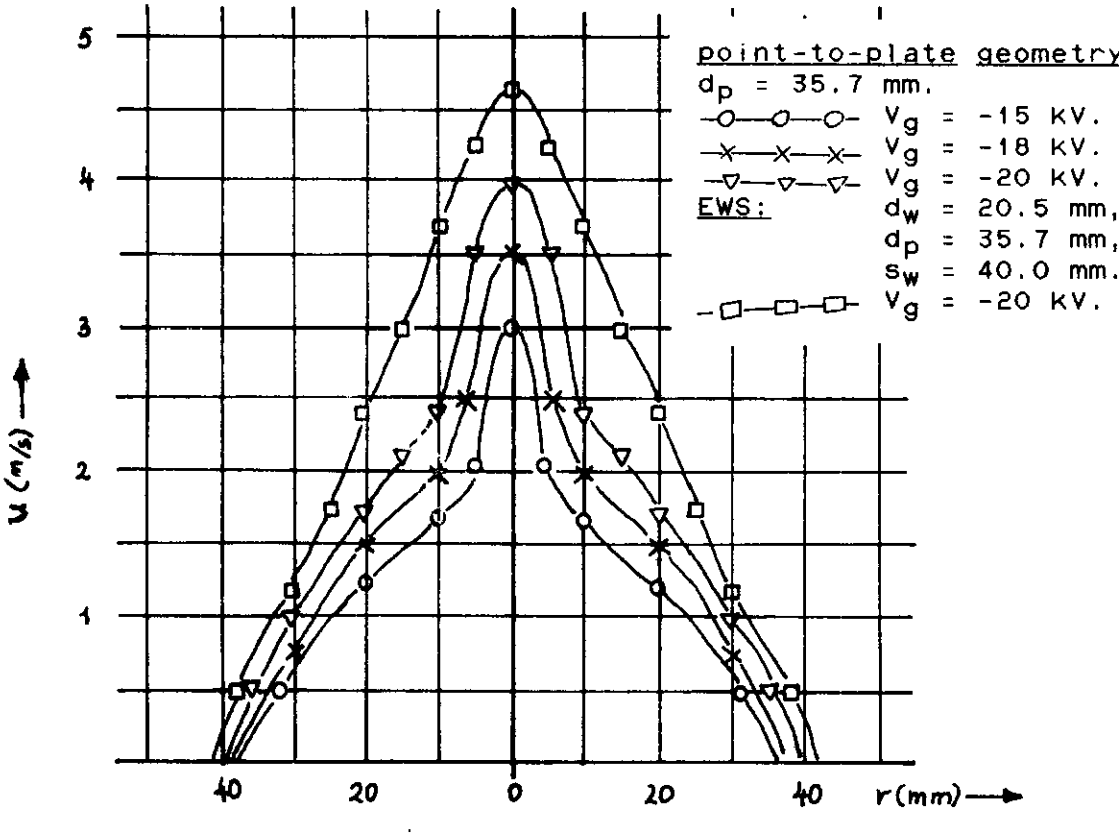

Fig 12: Corona wind velocity [u(r)] vs radial distance (r) at the anode. Note that the highest wind velocities are obtained with the EWS.

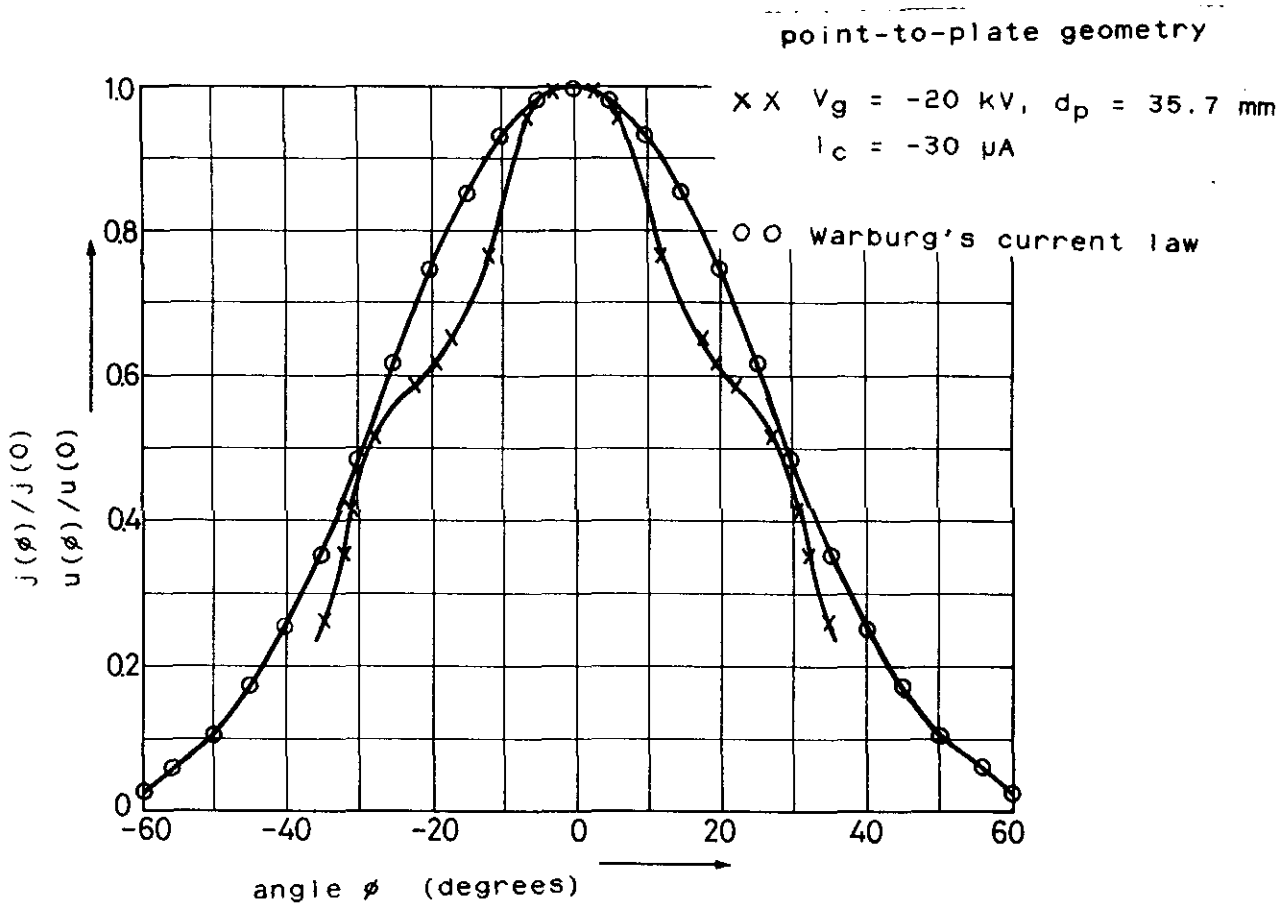

Fig. 13: Normalized corona wind velocity [u(r)/u(0)] vs angular displacement (ø) at the anode. A comparison is made with the Warburg's current density distribution law.

The air mass flow rate M due to the corona wind can be estimated from the equation

$$M = 2\pi\rho_m \int_0^\infty ru(r)dr \ . \qquad (36)$$

The number of air molecules N_a crossing a plane normal to the flow per sec may be deduced from

$$N_a = \frac{M}{m_a} \ , \qquad (37)$$

Where the average molecule in air has a mass m_a calculated from the equation

$$m_a = (0.8 \cdot 28 + 0.2 \cdot 32) \cdot 1.67252 \cdot 10^{-27} \text{ kg} \quad .$$

Here it is assumed that air consists of 80 percent Nitrogen with atomic weight 28, and 20 percent Oxygen with atomic weight 32.

The number of negative ions crossing a plane normal to the air flow per second may be found from

$$N_i = \frac{I_c}{e} \quad .$$

Here e is the electronic charge.

An approximate value of the kinetic energy W_a possessed by the corona wind can be calculated from the equation

$$W_a = \tfrac{1}{2} \cdot \rho_m \cdot 2 \int_o^\infty \pi r \cdot u^3(r)\, dr \quad . \tag{38}$$

Here the velocity distribution $u(r)$ is determined at the position of the plate.

From Eq.(38) an electrokinetic energy conversion efficiency ζ, can be deduced as follows:

$$\zeta \approx \frac{W_a}{W_e} \cdot 100\% \quad , \tag{39}$$

where

$$W_e = V_g \cdot I_c ,$$

is the electrical energy dissipated in the corona discharge per second .

A comparison of some hydrodynamic parameters and electrokinetic energy conversion efficiency is made between a point-to-plate geometry and EWS when the applied gap voltage V_g equals -20 kV in Table I. The data is obtained from Fig. 12.

TABLE I: EXPERIMENTAL RESULTS

	Electrical Parameters	Hydrodynamic Parameters	Electro Kinetic Conversion Efficiency
			ξ
			(%)
Point-to-plate Geometry d_p = 35.7 mm I_c = -30.0 μA	V_g = -20 kV N_i = 1.875×10^{14}/s W_e = 0.6 W	M = 0.0057 kg/s N_a = 1.19×10^{23}/s W_a = 0.0076 J/s u_{max} = 3.9 m/s	1.27
EWS d_w = 20.5 mm d_p = 35.7 mm s_w = 40.0 mm I_w = -38.0 μA I_p = -13.5 μA I_c = -51.5 μA	V_g = -20 kV N_i = 3.2×10^{14}/s W_e = 1.03 W	M = 0.0108 kg/s N_a = 2.25×10^{23}/s W_a = 0.0351 J/s u_{max} = 4.7 m/s	3.41

3.2.3 Discussion of Experimental Results

For the same applied gap voltage the EWS generates corona wind with a higher velocity distribution than a point-to-plate geometry as is shown in one of the graphs of Fig. 12. Since the average velocity of the corona wind is proportional to $\sqrt{(I_c)}$ as stated in Eq.(29a), the increase in the magnitude of velocity distribution generated in an EWS can be directly correlated to an increase in I_c as has been explained in section 3.1.2.

From the graphs of Fig. 13 it is concluded that there is no similitude between the velocity distribution function and the Warburg's current density distribution law. Apparently the correlation between current and wind velocity is more complicated.

From Table I we see that for the same applied gap voltage an EWS generates a higher air mass flow rate which has a greater kinetic energy than a point-to-plate geometry. The higher air mass flow rate and kinetic energy in the EWS correspond to the higher corona wind velocity which it generates. The electrokinetic conversion efficiency of such an EWS is also raised from about 1 percent to the order of 3 percent. The modification of the electric field configuration in the EWS geometry as shown in Fig. 10 may result in complex qualitative and quantitative changes of the discharge characteristics.

Our calculations snow that for every ion there are about 6.4×10^8 neutrals which reach the anode. The corona wind is therefore mainly made up of neutrals.

3.3 Constant-Temperature Hot-Wire Anemometer Velocity Measurements

The corona wind velocity distribution is measured by means of a constant-temperature hot-wire anemometer DISA type 55d01. The small size of the anemometer measuring probe should give a better spatial resolution of the velocity distribution than the Pitot-tube velocity measurements. The anemometer also can measure turbulence intensities with a frequency of up to 100 kHz.

3.3.1 Principles of Measurements

Anemometric velocity measurements [69-72] are based on a measurement of the convective heat loss from an electrically heated metallic wire, which acts as a sensor. The anemometer measuring probe is shown in Fig. 14.

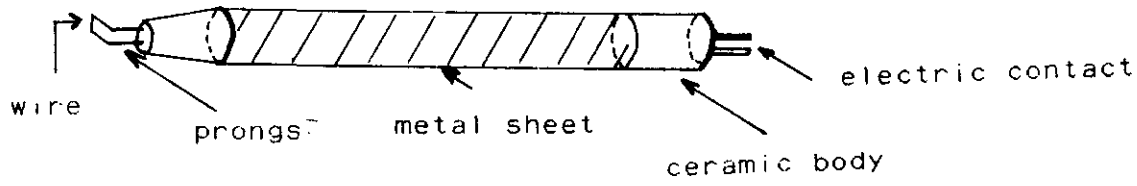

Fig. 14: Constant-temperature hot-wire anemometer probe.

Hot-wire anemometry relies on the fact that the electrical resistance of a metal conductor is a function of its temperature. The essential part of the hot-wire anemometer is therefore a very thin metal wire heated

by an electrical current and inserted into the flow under investigation. The transfer of heat from the wire to the flow increases with increasing flow velocity in the neighbourhood of the element. This cooling effect of the flow is compensated by using a variable-current feedback loop which keeps the temperature and the resistance of the sensitive element constant. The compensating current or voltage is then used as a measure of the flow in the immediate neighbourhood of the sensor.

The operating characteristics of the hot wire are fixed by selecting an overheating ratio λ. The resistance of the hot wire sensor is given by

$$R_h = (1 + \lambda)R_o \ .$$

$$= (1 + \beta \bullet \Delta T)R_o \ . \qquad (40)$$

Here R_o is the resistance of the sensor at ambient temperature. The temperature coefficient of resistivity of the sensor wire is β, and ΔT is the temperature difference between the hot wire sensor temperature and the ambient temperature. The sensitivity of the hot wire sensor increases with increasing overheating ratio. At higher wire temperatures however the sensor's lifetime is shortened because of its higher evaporation and oxidation rate. For this reason the overheating ratio in commercially available hot-wire probes is not chosen above 0.8.

The hot wire sensor is mainly sensitive to velocities in a plane perpendicular to the direction of the sensor as shown in Fig. 15. This makes hot wire anemometry readings difficult to interpret.

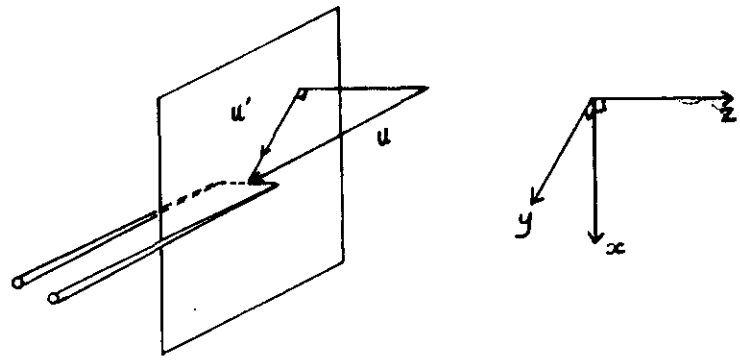

Fig.15: Velocity component u' of the velocity u to which the sensor is most sensitive. The sensor is placed in the y direction.

The output signal of the anemometer unit connected to a hot-wire probe is a voltage which is a non-linear function of the wind velocity. The output signal follows from the following formula,

$$V_a = V_o + B \bullet u^{\kappa} \quad . \tag{41}$$

The output voltage of the anemometer is denoted by V_a, and V_o is the output voltage with zero wind velocity. The wind velocity is denoted by u, while κ and B are constants. The value of κ is approximately 0.5. It follows that

$$(V_a - V_o)^2 = B^2 \bullet u \quad . \tag{42}$$

It may be necessary to electrically shield the anemometer probe from the EWS electric field in order to avoid errors in measurements. An error could be caused by corona current of the EWS which is drawn by the probe. This probe current may generate additional wind or disturb the velocity boundary layer around the probe. This problem is in fact a part of our subject matter. The probe may have to be placed below or near a grounded shield during velocity measurements. However

my measurements indicated that if the distance between the grounded wires of the EWS and the probe is equal or greater to the spacing between the wires of the EWS, then no extra shielding of the probe apart from that afforded by the grounded EWS wires is neccessary.

Fig. 16 shows a block diagram of the experimental setup for the determination of wind velocities and the recording of anemometer output signals. The probe in the electric wind system can be moved in the x, y , and z-directions by means of a displacement mechanism. The output signal of the anemometer unit can be fed to an x-t recorder, or to a dc-voltmeter. The dc-voltmeter measures the average output signal of the unit because of the use of an additional low pass filter. The x-t recorder is inherently slow.

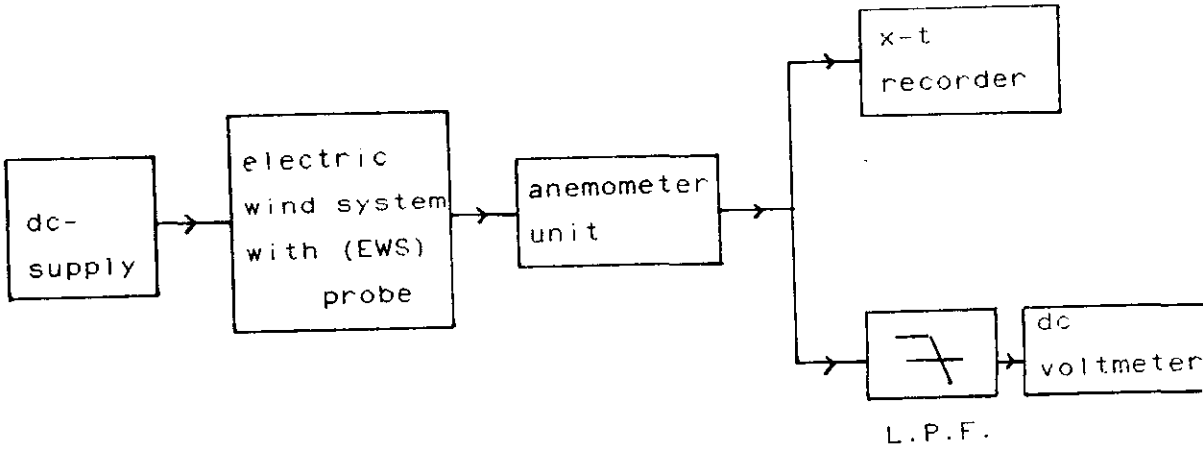

Fig. 16: Block diagram of the experimental setup.

Fig. 17 shows the configuration used for the determination of the time averaged wind velocity on axis as a function of the voltage applied to the cathode of the EWS. For these measurements the probe is situated

right below the corona discharge point with a fixed value x_p of 30 mm. The configuration of Fig. 17 is also used for measuring time averaged wind velocity profiles. The probe is then situated at a fixed value of x_p and can be moved in the y or z directions.

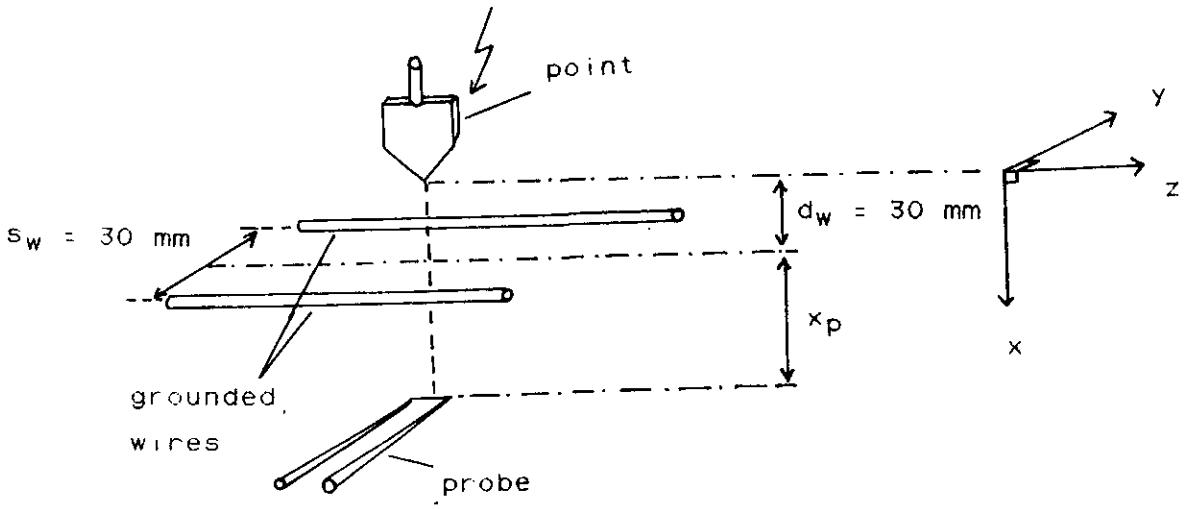

Fig. 17: Configuration for measurement of average corona wind velocity by a constant-temperature hot-wire anemometer.

3.3.2 Experimental Results

Experimental results are expressed in terms of $(V_a-V_o)^2$. This quantity is used because it is a direct measure for the wind velocity u according to Eq. (42).

Fig. 18 shows a plot of $(V_a-V_o)^2$ versus the applied voltage V_g at the point. The probe was fixed in position on the axis of the EWS. For this probe position, as already explained, it was not neccessary to provide an extra electrical shielding of the probe.

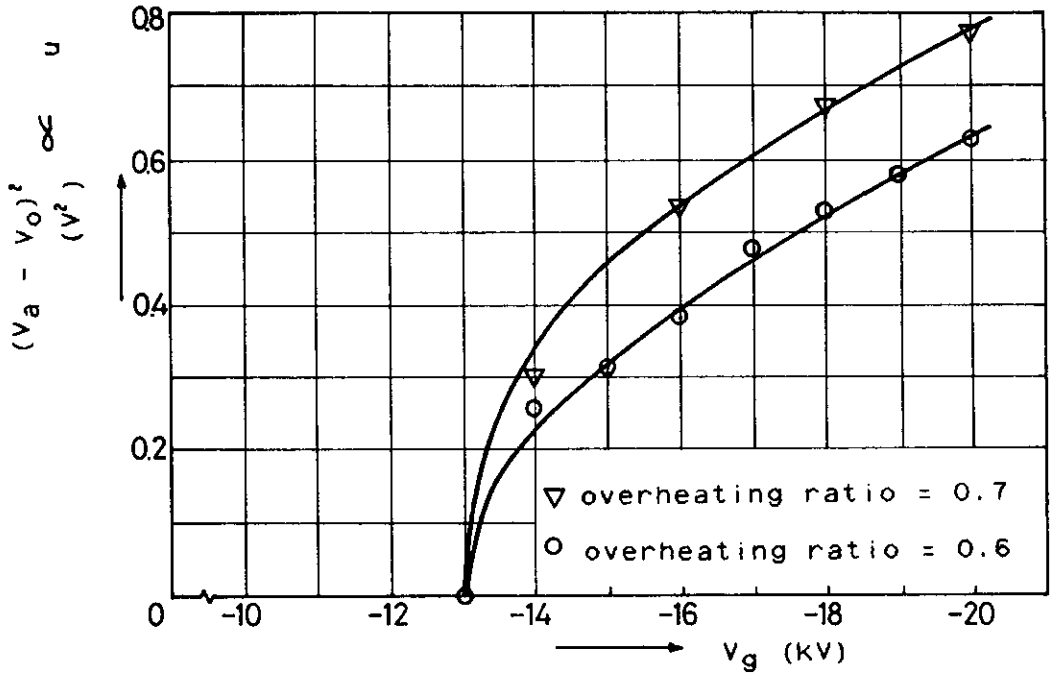

Fig. 18: Graph of $(V_a-V_o)^2$ versus applied point voltage V_g.
Probe coordinates x_p = 30 mm, y = z = 0.

In Fig. 19 the quantity $(V_a-V_o)^2$ is plotted against the displacement in the z direction at a zero value of y and four different values of the distance x_p.

In Fig. 20 the quantity $(V_a-V_o)^2$ is plotted with the probe displaced in the y direction at a zero value of z and the same four different values of the distance x_p.

In both these cases, the applied voltage at the cathode is -16 kV, the overheating ratio chosen for the

probe is 0.7, and there was no need to electrically shield the probe. The probe sensor is directed parallel to the z-axis.

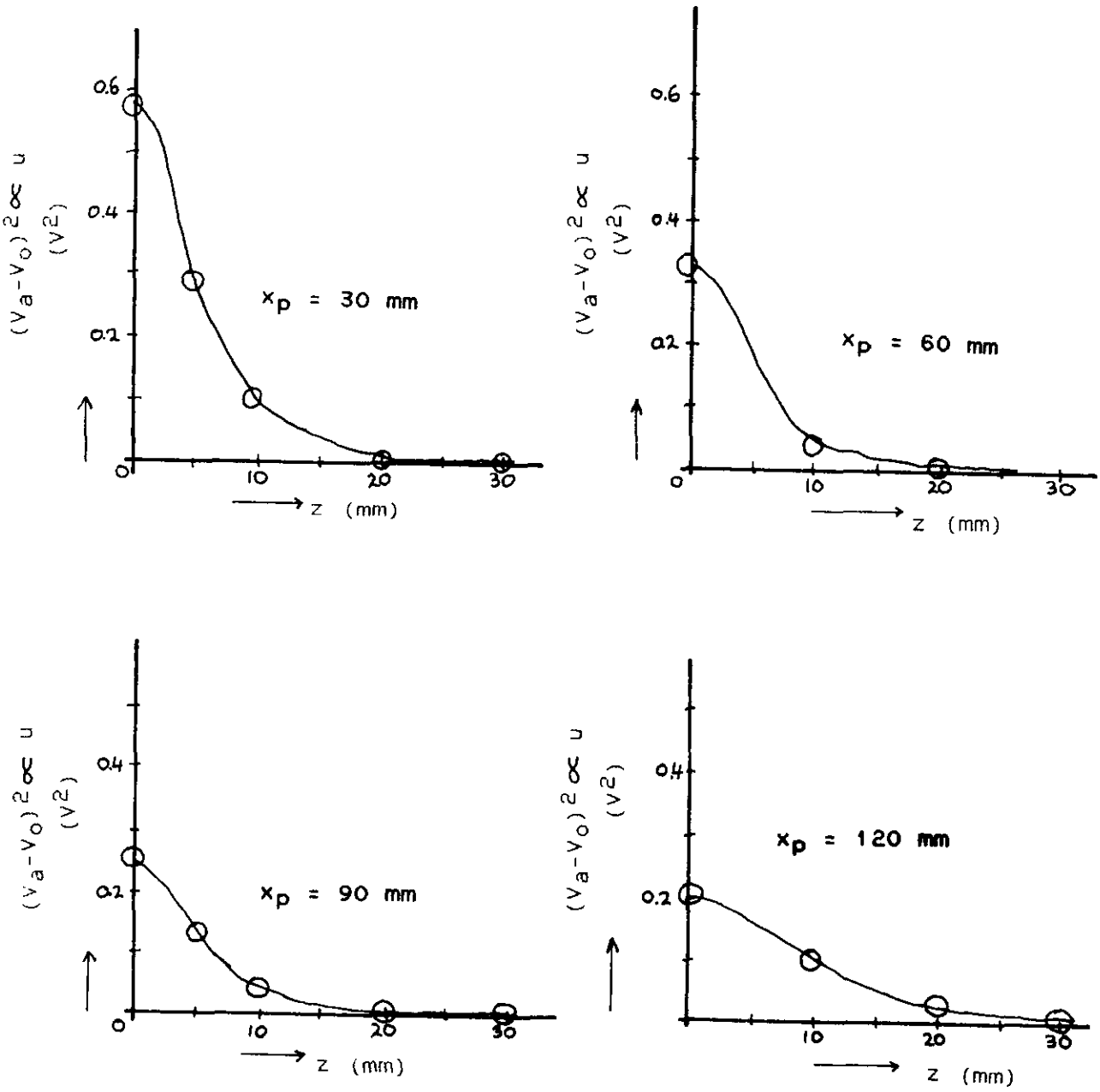

Fig. 19: Graph of $(V_a-V_o)^2$ versus the displacement z for an EWS

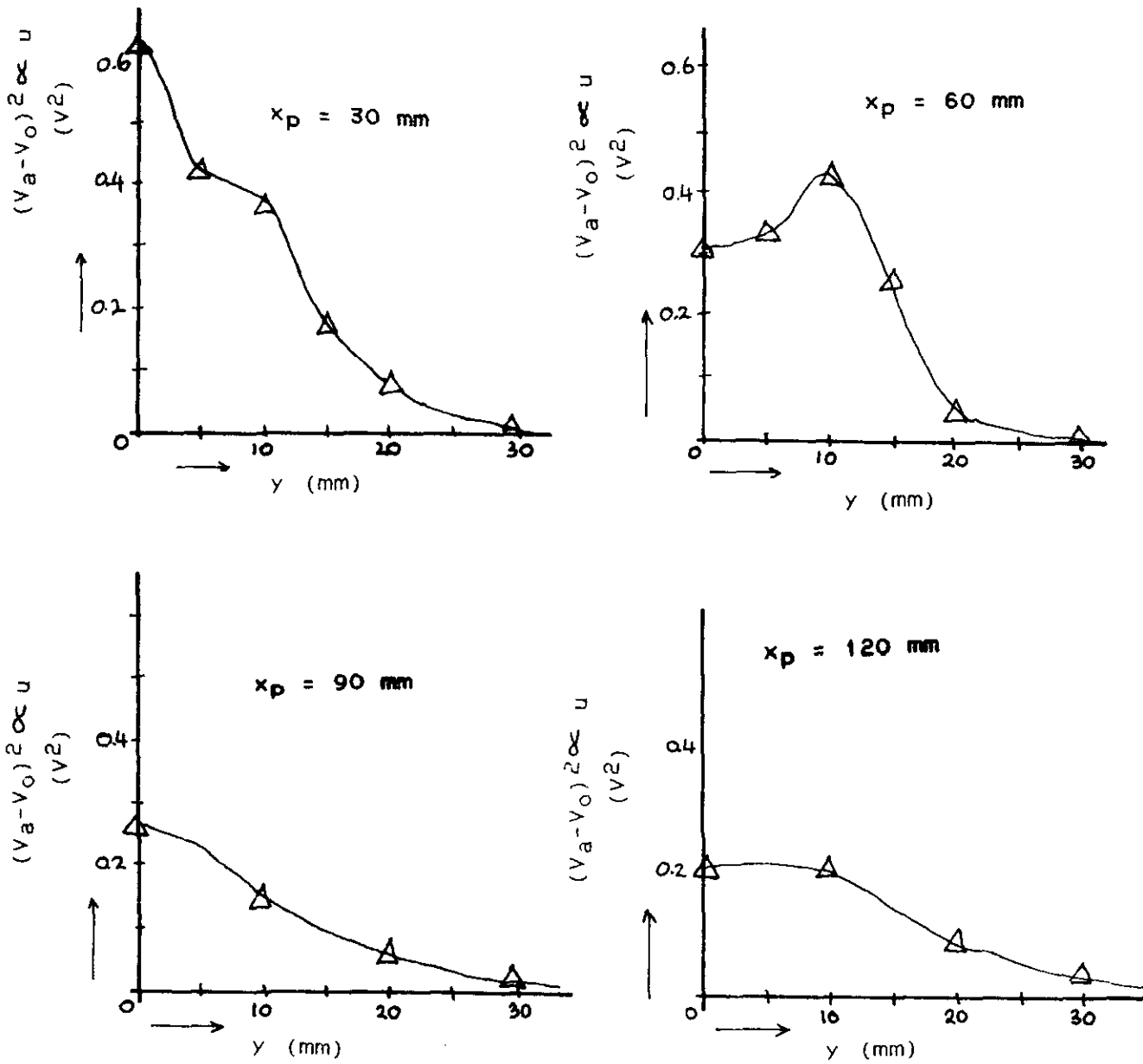

Fig. 20: Graphs of $(V_a-V_o)^2$ versus the displacement y.

3.3.3 Discussion of Experimental Results

From Fig. 18 we deduce that the time averaged on axis velocity of the corona wind is directly proportional to the applied gap voltages for applied gap voltages much higher than the corona inception voltage. This indicates that the average velocity of the corona wind is also directly proportional to the applied gap voltage which is in agreement with Eq.(29b).

From Fig. 19 and Fig. 20 it is deduced that the jet has a small spread. Beyond the wires the velocity generally decreases with increasing values of x_p. This is also characteristic for a free turbulent jet with no further input of energy and momentum. The velocity profiles in the z-direction are similar for different x_p while the velocity profiles in the y-directions are not because the wires disturb the flow and create wakes. The velocity profiles in the y-direction are wider than those in the z-direction due to the configuration of the electric field and obstruction caused by the wires to the flow.

These measurements with different positions of the probe indicate that the jet is confined to a region with a cross section of about 2x4 cm^2 in this particular setup. The spread of the jet in the y direction is greater. The maximum range of the corona wind was determined to be about 250 mm below the corona discharge point.

3.4 Flow Visualization by Schlieren Measurements

Schlieren measurements were performed to visualize the flow field of the corona wind. Very short time exposure pictures of the corona wind were taken. The fast photography schlieren technique should give more information on the structure of the corona wind. For comparison schlieren pictures of a mechanically generated jet were also taken.

3.4.1 Principles of Measurements

A conventional Toepler schlieren system [73, 74] with high speed photography was employed. A Nema Electronics nanolite provided the point light source supplying a divergent beam of light which is collimated by a 10 cm diameter lens of focal length 100 cm. The parallel beam of light was directed through the test gap to a schlieren head lens of 10 cm diameter and 100 cm focal length. The long focal lengths of the schlieren lenses are necessary to permit longer lengths of the corona wind under investigation. A "knife edge" was positioned in the focal plane of the schlieren head lens to obstruct a part of the light source image. A narrow black line on a transparent photographic plate was used as the knife edge. A mirror was used to reduce the length of the setup due to limitations of space. The Toepler schlieren system is shown in Fig. 21.

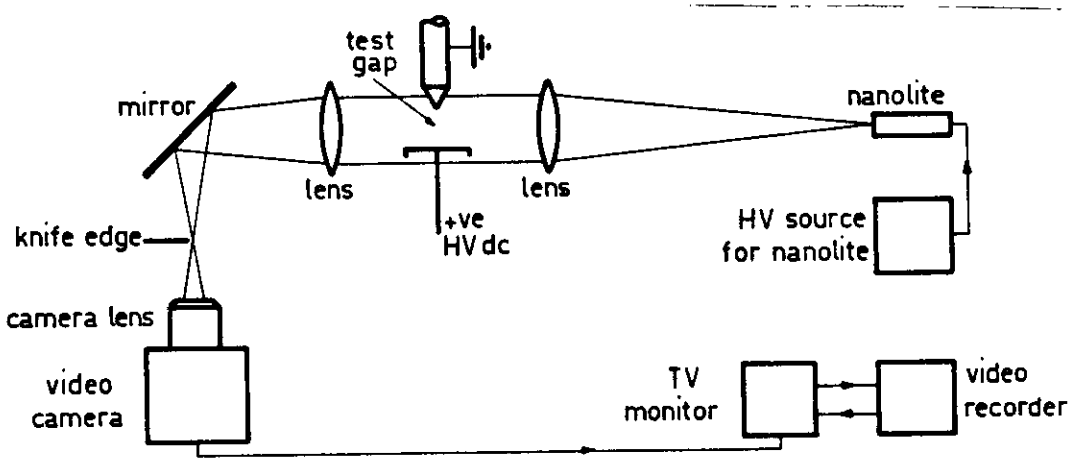

Fig. 21: The Toepler schlieren system for the visualization of the corona wind.

The nanolite provided a very short duration light pulse of 700 ns , with a risetime of 50 ns. The nanolite has its maximum light output in the wavelengths between 400 nm and 650 nm.

To take short time exposure photographs , a Nikon camera and objective lens of focal length 8.5 cm was used. A very short duration exposure picture was made by leaving the shutter of the camera open and allowing the nanolite to flashover once. The schlieren image is formed on a very sensitive photograhic film, type AGFA Scopic RPI, which is very sensitive to the green and blue light emitted by the nanolite.

A Philips video camera coupled with a Nikon objective lens of focal length 10.5 cm was used in making photographs of the corona wind on videotape. A 50 Hz high voltage source was used to flashover the nanolite.

The schlieren pictures were recorded on a 19 mm U-Matic KCA-30 video cassette. A Sony 750 m video recorder

was used. The schlieren pictures can be observed on a Philips TV monitor. Pictures can be made of the playback of the video recordings by a Nikon camera with a shutter speed of 1/15 s carrying a 50 ASA film.

A mechanically generated air jet was made by a heat gun rated at 220 V ac 50 Hz, 2 A. A 45 degrees nozzle is fitted to the heat gun, see Fig. 22. A 3.2 mm hole is drilled at the tip of this cone . A needle of less than 3 mm diameter , connected to a HV supply can be supported along the axis within the cone. This structure allowed the superposition of some corona wind on mechanical wind.

Experiments are carried out on a point-to-plate geometry and on an EWS. In both instances the cathode had only one point. The point was screwed to the top of a soldering iron which was subsequently heated by a 36 V dc supply to produce the neccessary temperature and the corresponding density variations in the corona wind. Without this additional heating system the corona wind velocity was found to be too low to generate discernible optical disturbances.

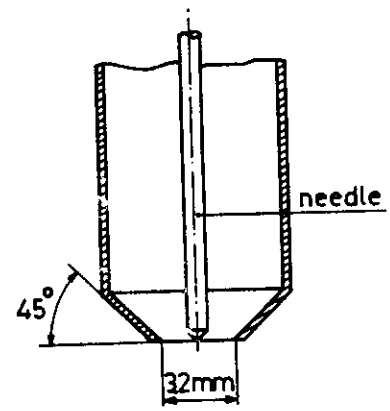

Fig. 22: Nozzle for mechanically generated jet.

If the knife edge in front of the camera lens cuts off a part of the light source image, the light intensity

on the photographic plate will be reduced. Let h_l be the reduced width of the light source image and Δh_l be a small increase of the width due to an optical disturbance in the test field caused by a density variation there. If the light source image is assumed to be constant it can be shown that the photographic plate will show a relative light intensity change

$$\frac{\Delta \upsilon}{\upsilon} = \frac{\Delta h_l}{h_l} \, . \tag{43}$$

In the above equation υ is the uniform light intensity at the photographic plate without any optical disturbance in the flow field, and $\Delta\upsilon$ is the light intensity change caused by air density variations in the flow field. It may be shown that , if the light beam is in the direction y

$$\frac{\Delta \upsilon}{\upsilon} = \frac{\Psi}{h_l} \int \frac{\partial n}{\partial z} \, dy \, , \tag{44}$$

where Ψ is the focal length of the schlieren head lens, and n is the refractive index of the test medium. The flow field boundaries define the limits of the integral along the light ray in the above equation.

A schlieren system can be used for qualitative, [75-80] as well as quantitative [81-89] measurements of gas flow. However the former only are performed in this work due to the unreliability and difficulty of making quantitative studies. Problems are the aberrations in the imaging of the light source and the

optical disturbance, not to mention the integrating nature of the quantitative parameter inherent with this measurement system.

3.4.2 Experimental Results

Fig. 23 and fig. 24 show pictures of a corona wind taken by the fast photography technique.

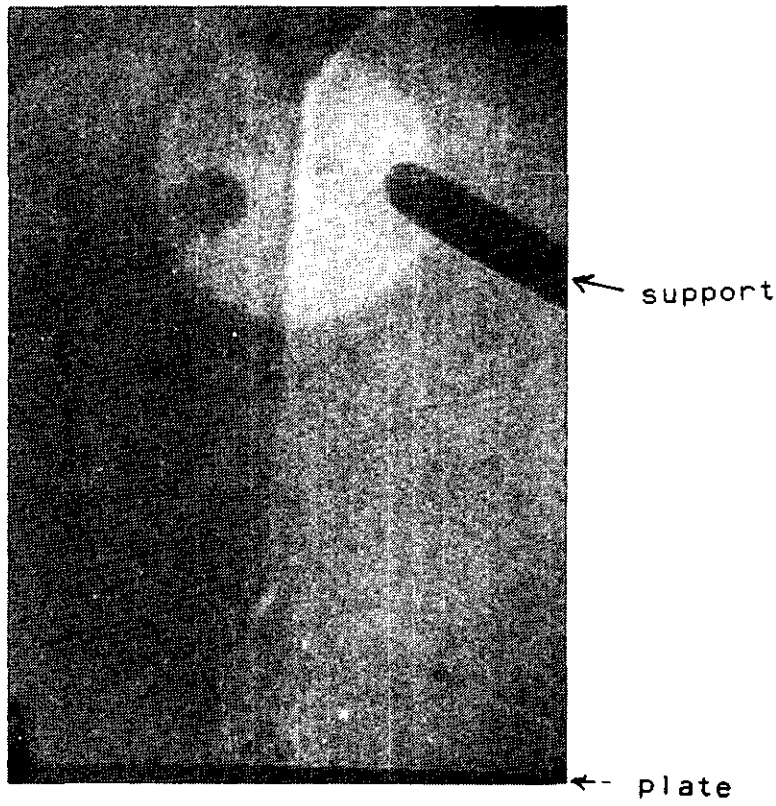

Fig. 23: The corona wind in an EWS.
d_w = 15 mm, d_p = 73 mm,
V_g = -17 kV, s_w = 20 mm.
Fast photography technique. Instant 1.
The two wires are perpendicular to the plane of the picture. Together with their supports they give a black outline.

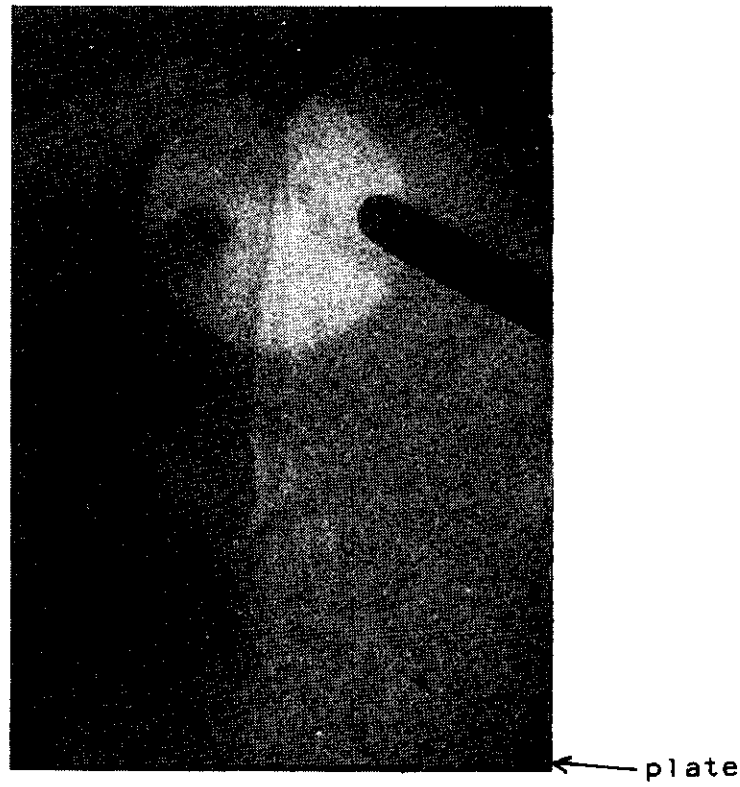

Fig. 24: The corona wind in an EWS, as Fig. 23, now at a different instant.

Fig. 25 and Fig.26 show pictures of the corona wind in a point-to-plate geometry and in an EWS.The narrow jet originates from the high-voltage electrode where it is firmly anchored and proceeds to the grounded plate where it was observed to wiggle or move about radially.

Fig.25: Corona wind in a point-to-plate electrode geometry. d_p = 73 mm, V_g = -30 kV. Pictures taken from TV monitor screen.

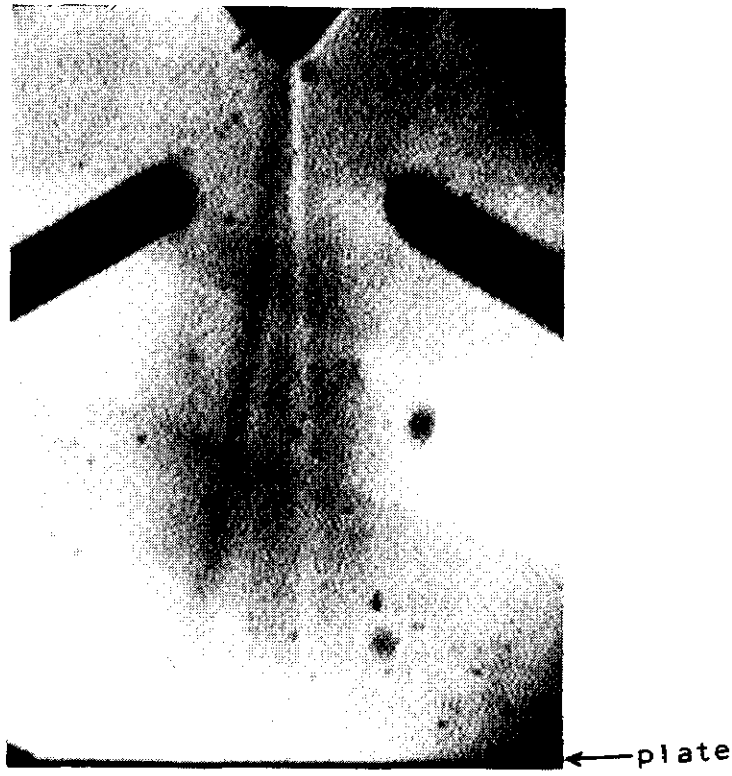

Fig. 26: Corona wind in an EWS.
d_w = 15 mm, d_p = 73 mm, s_w =15 mm,
V_g = -20 KV
Pictures taken from TV monitor screen.

Fig. 27 shows a picture of the mechanical wind. Fig. 28 shows a picture of the effect of corona discharge in a mechanical wind.

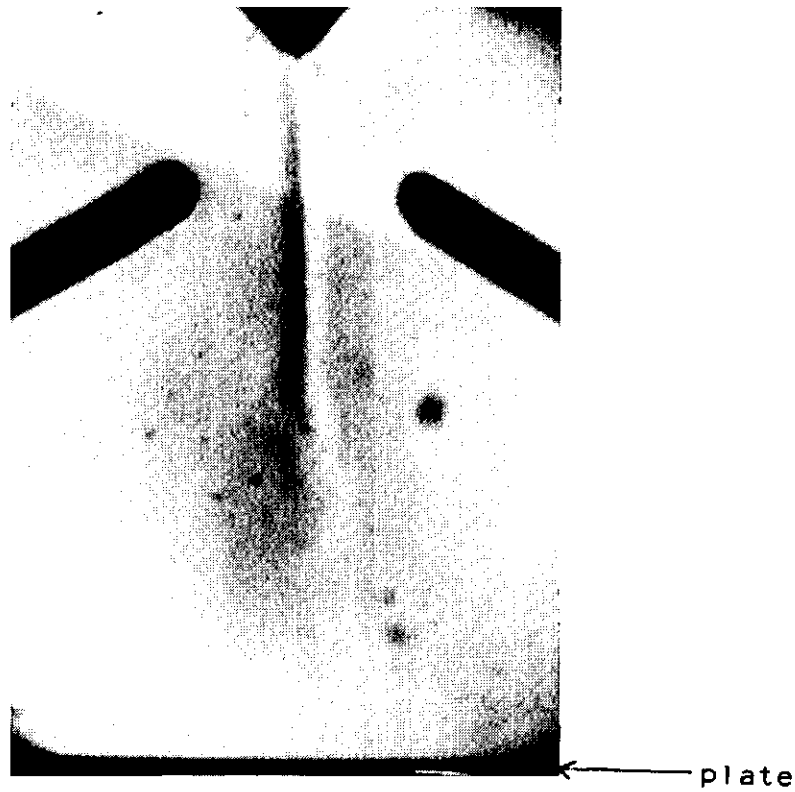

Fig. 27: Mechanical wind .
Picture taken from TV monitor screen.
Setup as in Fig. 26.

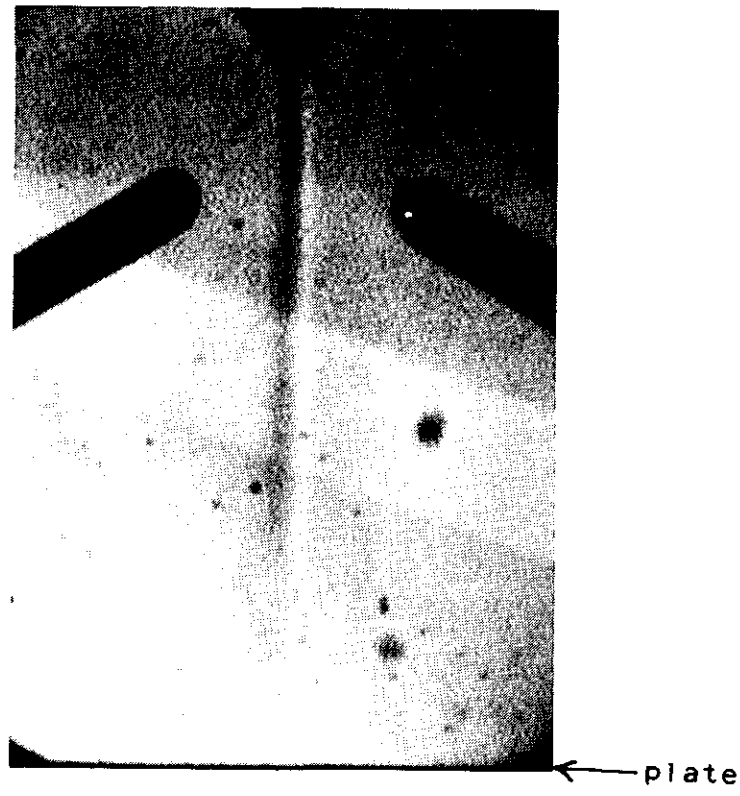

Fig. 28: Corona wind superimposed on mechanical wind. Setup as in Fig. 26. Same mechanical wind overpressure. Picture taken from TV monitor screen.

3.4.3 Discussion of Experimental Results

Schlieren pictures in Fig.23 to Fig. 26 indicate that the corona wind jet is basically laminar. However the corona wind jet wiggles about laterally presumably due to boundary condition variations at the electrode surfaces.

Fig. 27 shows that a mechanically created jet from an orifice is turbulent.

Fig. 28 shows that corona discharge superimposed on a mechanical wind makes the mechanical wind less turbulent.

In schlieren measurements flow visualization is only possible in regions which have large enough density variations. In our case the neccessary density variations were created by heating the cathode. This means we could see clearly only the air which became heated by coming into contact with the cathode. The schlieren pictures therefore indicate that the corona wind is a narrow jet which is not the case when we compare with the Pitot-tube and the anemometer measurements. It became therefore desirable to use another visualization technique which could show the entire flow pattern. This technique is outlined in the next section.

Even though the schlieren measurements show only the central part of the flow, we may conclude from the fairly stable behaviour of that central part that corona wind indeed produces a fairly stable flow pattern.

3.5 Flow Visualization by Injection of Carbon Dioxide Generated Mist Into the Corona Wind

According to a study on the flow characteristics of the corona wind by P.T.M. Vaessen [90], which forms a part of this research, the injection of a number of carbon dioxide generated mist trails into the corona wind visualizes the flow more faithfully. It is shown in this study that although the carbon dioxide generated mist particles acquire charge from the corona discharge their motion is not much affected by the electric field of the discharge gap, and can therefore be used to follow the flow of the air. The flow pattern of the mist trails is shown in Fig. 30.

From a study of the videotapes of the corona wind flow patterns which were made in this study, some pictures of the corona wind were made and are reproduced here. Part of this joint research work has been published elsewhere and appears as an appendix.

3.5.1 Experimental Results

Four possible viewing directions are possible as shown in Fig. 29.

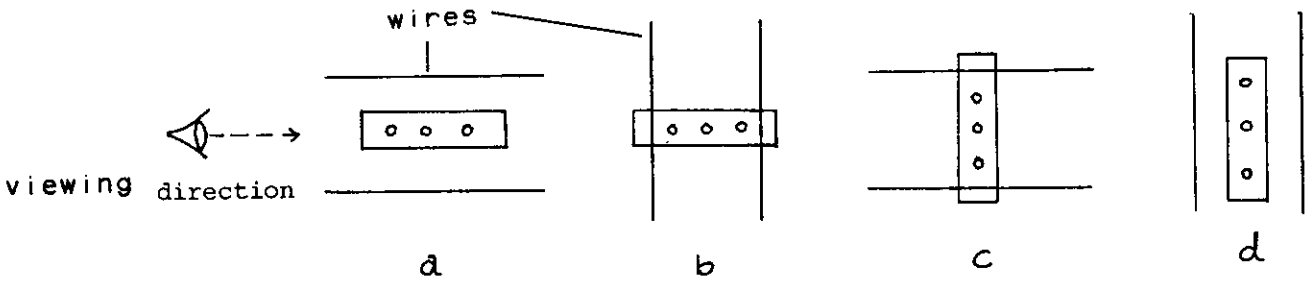

Fig. 29: Four possible viewing directions . The mist is flowing as separate trails from the holes in the mist generator (three holes shown in this figure).

Fig. 30 to Fig. 35, pictures taken from viewing direction d of Fig. 29, show the effect of starting the corona discharge . The two wires are grounded and $d_w = s_w = 30$ mm. A voltage of -20 kV is applied to the point.

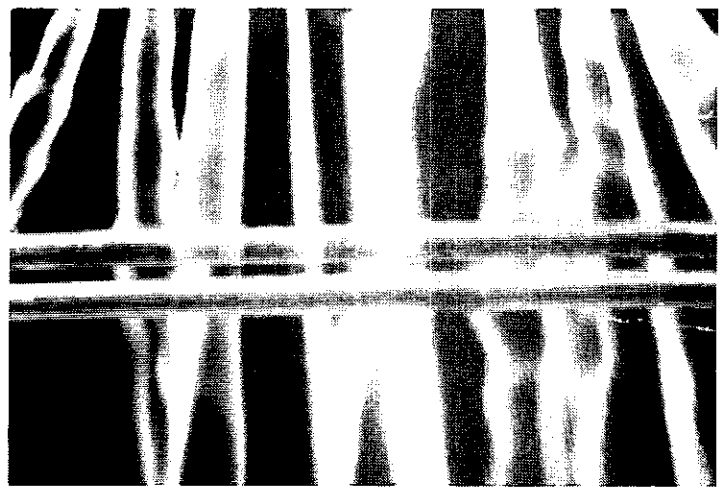

Fig. 30: No voltage applied to the point.

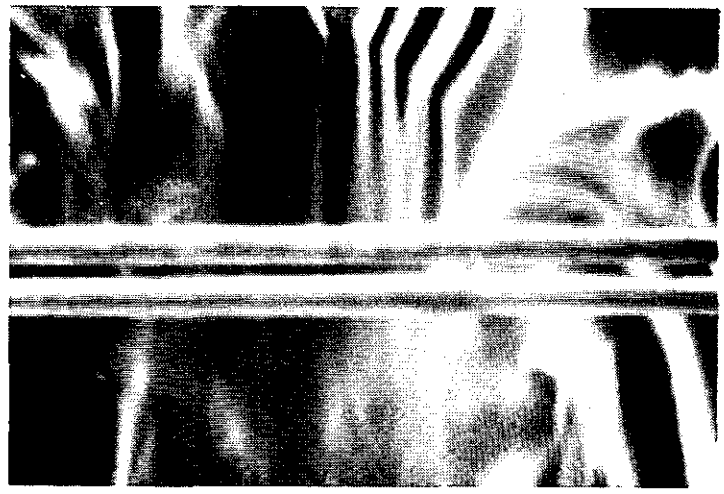

Fig. 31: 0.42 s after switching on -20 kV .

Fig. 32: 0.83 s After switching on -20 kV .

Fig. 33: 1.67 s after switching on -20 kV .

Fig.34: 2.50 s after switching on -20 kV .

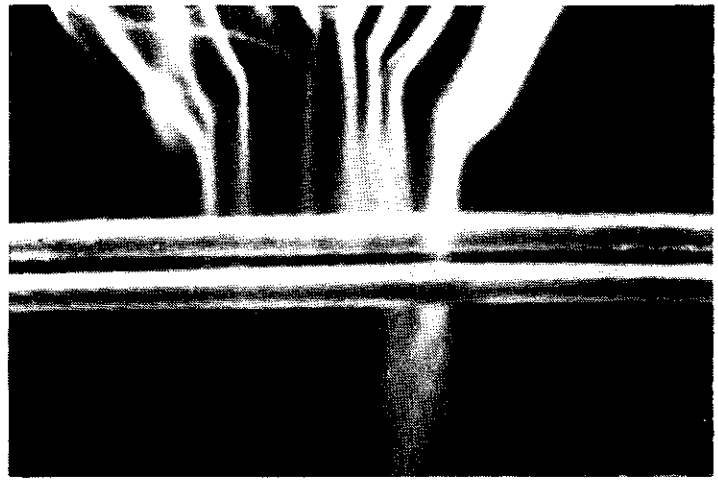

Fig. 35: 3.33 s after switching on -20 kV .

Fig. 36 and Fig. 37 are taken from the viewing direction c in Fig. 29. Fig.36 shows a smooth laminar multibeam flow. The corona point is indicated with a small black line at the top of fig. 37. The white circles are holes in the perspex device supporting the EWS. The configuration of the EWS is still the same.

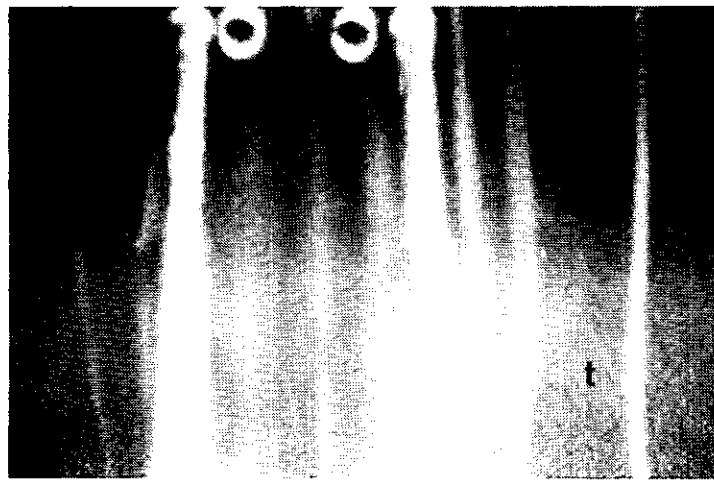

Fig. 36: No voltage applied to the point.

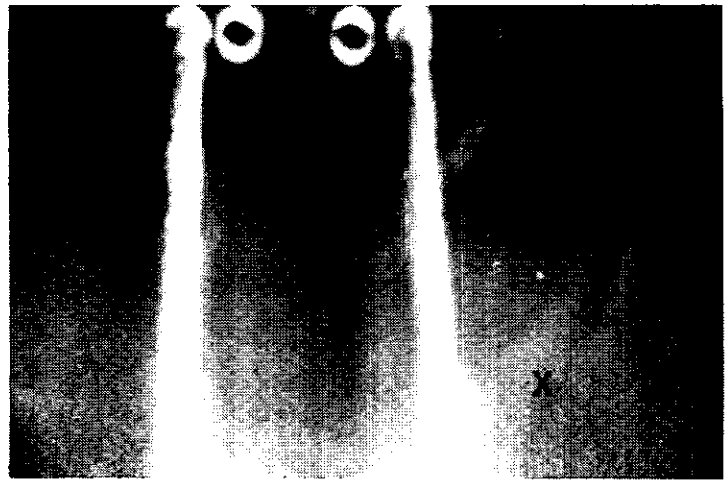

Fig. 37: Steady state after switching on -20 kV.

Fig. 38 and Fig. 39 are taken to demonstrate the effect of corona wind on mechanical wind. In this case only one mist trail was carried in by the air flow coming in through the orifice.

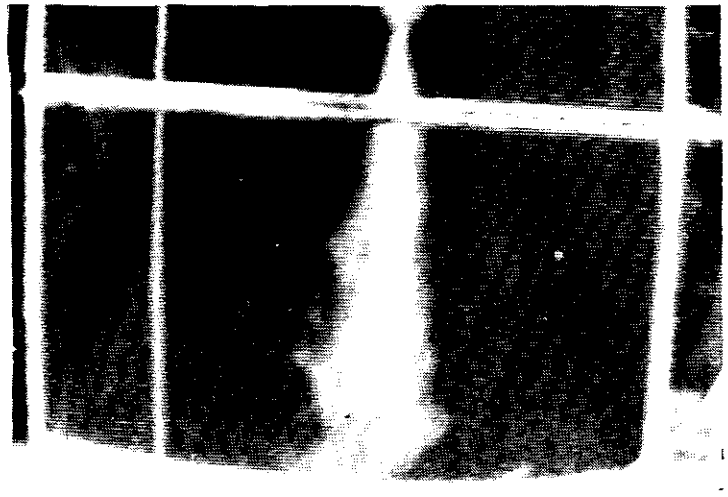

Fig. 38: Mechanically generated jet

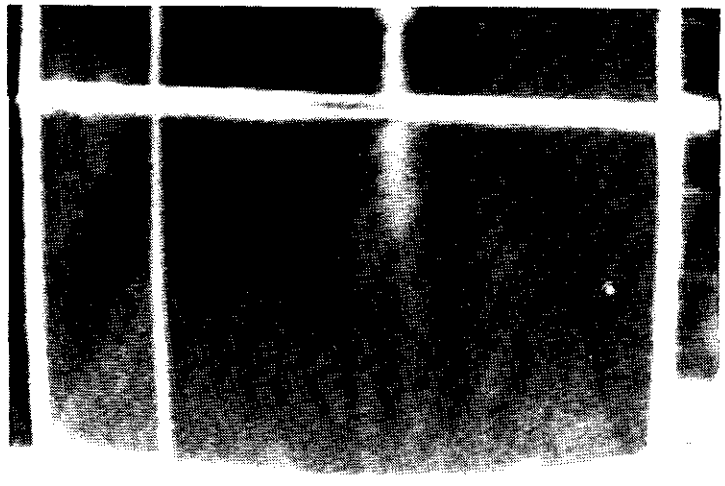

Fig. 39: Corona wind sumperimposed on mechanically generated jet . Steady state.

3.5.2 Discussion of Experimental Results.

In about 3 s the flow has reached a steady state as is shown in Fig. 30 to Fig. 35. In these figures we see that the air flow is initially drawn and directed towards the point and then pushed down with great velocity between the wires.

The diameter of the beam below the wires is ≈ 31 mm . This is in agreement with Pitot-tube velocity measurements and hot-wire constant-temperature anemometric measurements.

At the centre just below the point the air velocity has its maximum value. This can be seen in the figures because the mist is thicker at the outside of the flow than at the centre of the flow. We have already noted with Pitot-tube velocity measurements, that the velocity of the corona wind is bell shaped with an accentuated peak along the axis of the EWS or point-to-plate geometry. At higher air velocities the mist becomes less dense because of the quicker flow off of the water vapour droplets while the supply rate is still the same.

From Fig. 35 we deduce an envelope for the corona wind air flow as shown in Fig. 40.

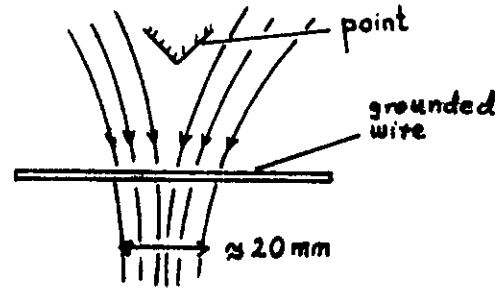

Fig. 40: Corona wind flow field from viewing direction d of Fig. 29.

From Fig. 36 and Fig.37 we deduce an envelope for the corona wind air flow as shown in Fig. 41.

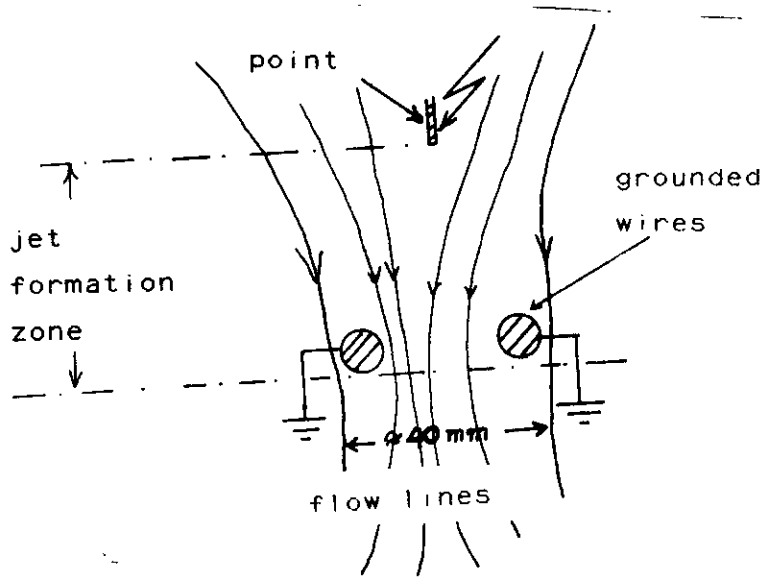

Fig. 41: Corona wind flow field from viewing direction c of Fig. 29.

Careful study of the video tape reveals that it takes generally less than 0.8 s for the flow to respond to the applied voltage. At voltages below the corona starting voltage no effect on the mist flow is observed. This proves that the electromagnetic polar forces indicated in Eq. (18) are negligible or we can equally conclude that the corona wind is due to the momentum transfer between ions and neutrals caused by Coulomb forces on ions.

From Fig. 38 and Fig. 39, we see that corona wind makes a mechanically created jet more laminar and reduces its spread. This is in agreement with schlieren measurements which are shown in Fig. 27 and Fig. 28..

Fig. 42 shows a sketch of a mechanically generated jet. Theoretically a mechanically genertated jet becomes turbulent when the Reynolds number is greater than 2100. In practice laminar free jets originating from an orifice cannot be produced [91]. This is

because the edge of the orifice introduces initial disturbances that grow and eventually make the jet a turbulent one. In Fig. 42 the growth of the disturbances introduced at the edge of the orifice is shown.

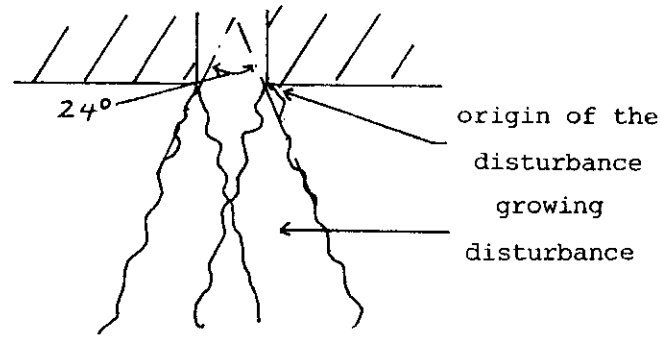

Fig. 42: Growth of the disturbances in a free jet.

The opening angle of the mechanically generated jets is about 24° [92]. The forces exerted by the wall which contain the air flow dissappear abruptly when the jet leaves the orifice. The disturbances that are introduced at that transition degenerate the jet.

On the other hand the corona wind is smoothly formed to a stable velocity profile within the discharge gap. When the jet leaves the energy input zone the change to a free jet is not abrupt as in the case of a mechanically generated jet but is very gradual. For this reason it has

a much better chance to create a laminar free jet. Indications for the existence of a laminar free jet are in the figures and the small cross section of the velocity distribution.

When the jet has travelled past the grounded wires the velocity profile decays slowly because turbulence starts to develop here also. Since the growth of this turbulence takes time, the spread in the flow remains fairly small.

3.6 Heat Transfer Measurements With and Without Corona Wind

The effect of corona wind blowing on a heat transfer surface is determined. The temperature-time curve of the heat transfer surface is measured when the heating element is switched on, first without corona wind. For comparison this temperature-time curve of the heat transfer surface is again measured when a corona wind is directed at the heat transfer surface.

3.6.1 Principles of Measurements

The EWS was used to generate corona wind. The heat transfer surface was a rectangular copper plate with dimensions 220 mm x 170 mm x 1.5 mm. The plate was mounted on a box made of pertinax. Heating of the plate was achieved by two heating elements conneceted in series. Each element is 61 Ohms. The heating elements are placed inside the box which is filled with styrofoam to minimize the conduction of heat to the opposite side of the heat transfer surface.

Power supply to the heating elements P_{in} is obtained from a 220 V/0-250 V, 0-4 A variable transformer, Philips type. P_{in} is measured by a Wattavi type wattmeter set in the range of 1 A, 100 V, and 0 - 100 W. The current through the heating elements I_h is measured by a Gossen UVA-5 type multimeter in the range of 0 - 1.5 A. We can say that

$$P_{in} = I_h^2 \cdot R_{he} \ ,$$

where R_{he} is the resistance of the heating elements. The experimental setup is shown in Fig. 43.

The temperature of the heated transfer surface is measured continuously. In this case use of thermocouple probes in conjuction with digital thermometers and an X-T plotter is adopted. The thermocouples which are used are model 8713 type K (Chromel-Alumel) with sensivity of 0.041 mV/^{o}C [93]. The probe tips are set to touch the heat transfer surface. The output of the thermocouple probe is fed to the Keithley model 871 digital thermometer. This digital thermometer

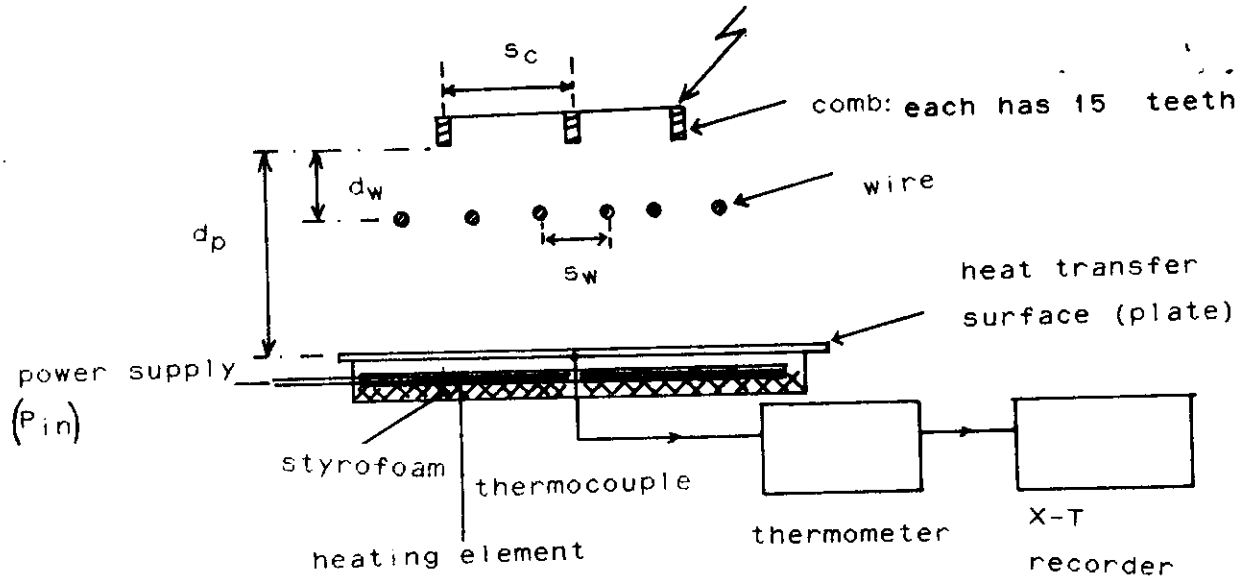

Fig. 43: Experimental setup for heat transfer measurements with and without corona wind.

is specially made to work with high resolution when Chromel-Alumel thermocouple probes are used. Its electronic unit has an input channel with two temperature ranges of 200^{o}C and 1370^{o}C, and analog output jacks from which continuous signal monitoring of temperature can be achieved by using a recorder.

The analog output jack of the thermometer is fed to the Y-input of the Siemens X-T recorder with a voltage range of 0.1 mV/cm - 3 V/cm and a time range of 0 - 10 cm/sec. The X-input is set to record time at the rate of 0.01 cm/sec. The Y-input is set in the range of 0.3 mV/cm. The obtained voltage against time curves are converted into temperature rise against time using standard conversion tables. [93, 94]

3.6.2 Experimental Results

Fig. 44 and Fig. 45 show the effect of a corona wind on the temperature of a heat transfer surface.

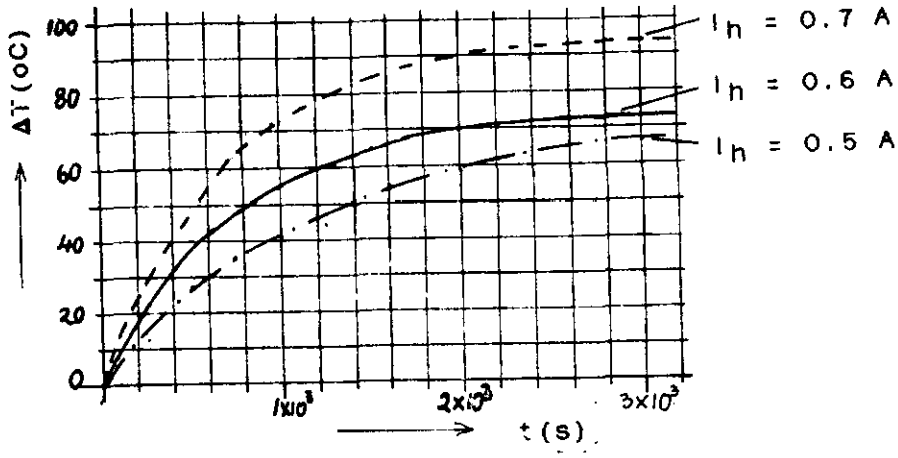

I_h = 0.5 A, τ = 540 s.
I_h = 0.6 A, τ = 550 s.
I_h = 0.7 A, τ = 760 s.

Fig. 44: Heating curves without corona wind. I_h = Current through the heating elements. The heating elements are switched on at t = 0.

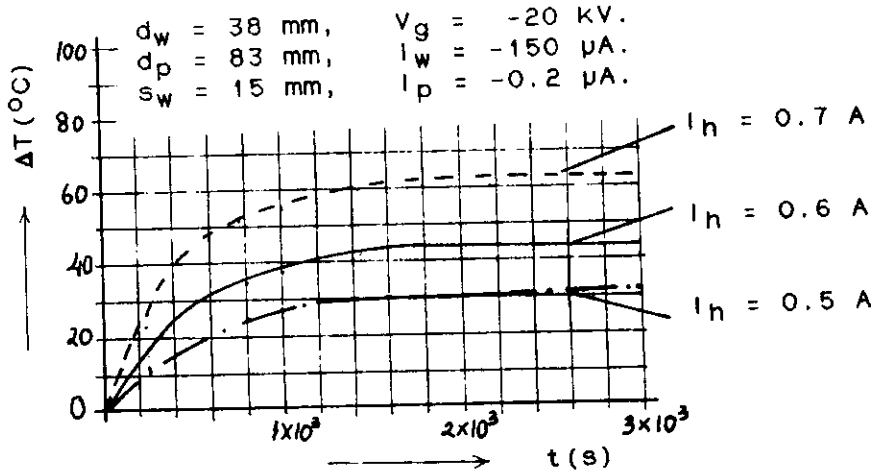

I_h = 0.5 A, τ = 340 s.
I_h = 0.6 A, τ = 340 s.
I_h = 0.7 A, τ = 280 s.

Fig.45: Heating curves with corona wind

Figure 46 to Fig. 53 are some of the measurements which show the effect of varying the arrangements of the EWS components on the heating curves of the heat transfer surface.

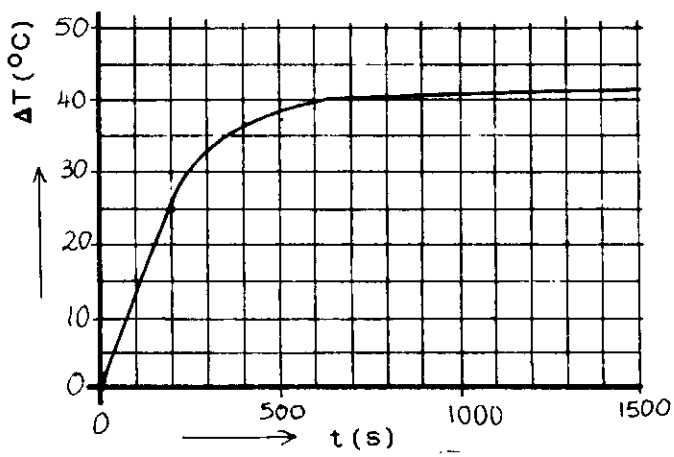

d_w = 33 mm, V_g = -20 KV, τ = 190 s.
d_p = 73 mm, I_w = -250 µA, I_h = 0.6 A.
s_w = 30 mm, I_p = -6.8 µA.

Fig.46

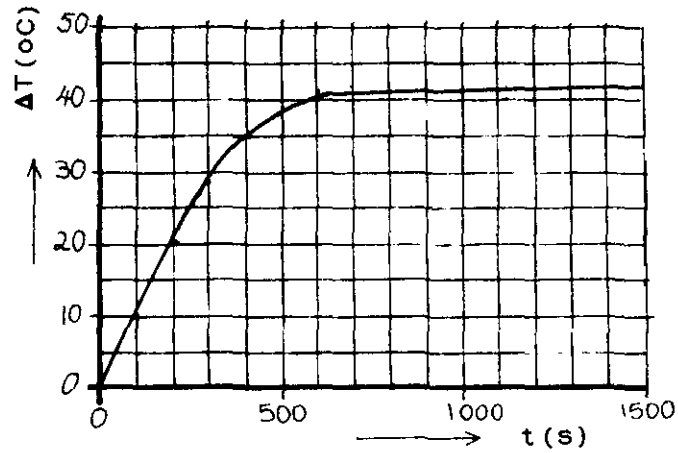

d_w = 33 mm, V_g = -20 kV, τ = 230 s.
d_p = 73 mm, I_w = -300 μA, I_h = 0.6 A.
s_w = 15 mm, I_p = -0.2 μA.

Fig. 47

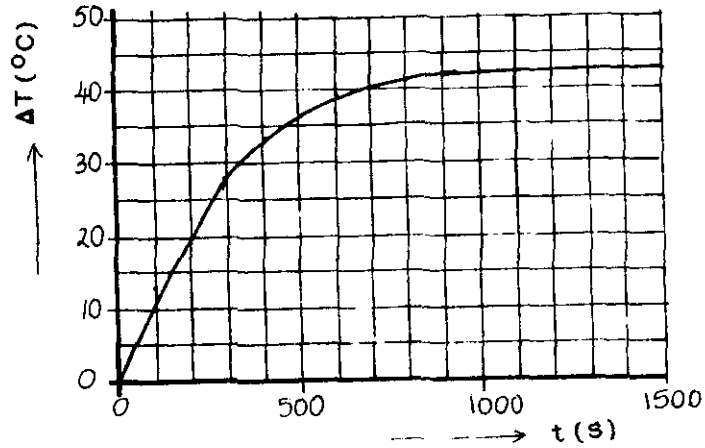

d_w = 38 mm, V_g = -20 kV, τ = 240 s.
d_p = 73 mm, I_w = -140 μA, I_h = 0.6 A.
s_w = 15 mm, I_p = -0.3 μA.

Fig. 48

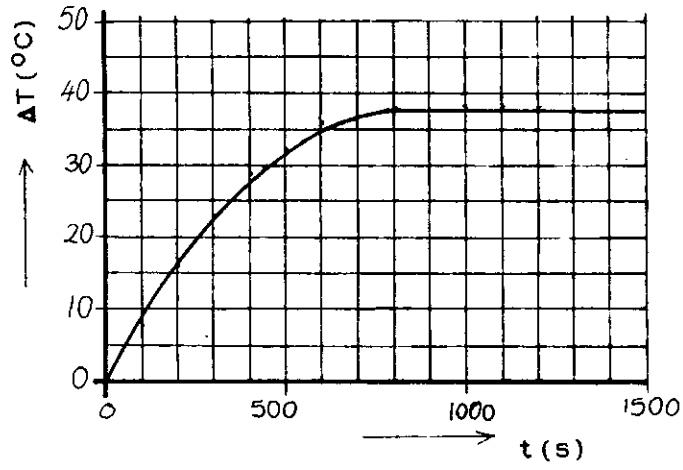

d_w = 33 mm, V_g = -20 kV, τ = 280 s.
d_p = 73 mm, I_w = -320 μA, I_h = 0.6 A.
s_w = 20 mm, I_p = -1.7 μA.

Fig. 49

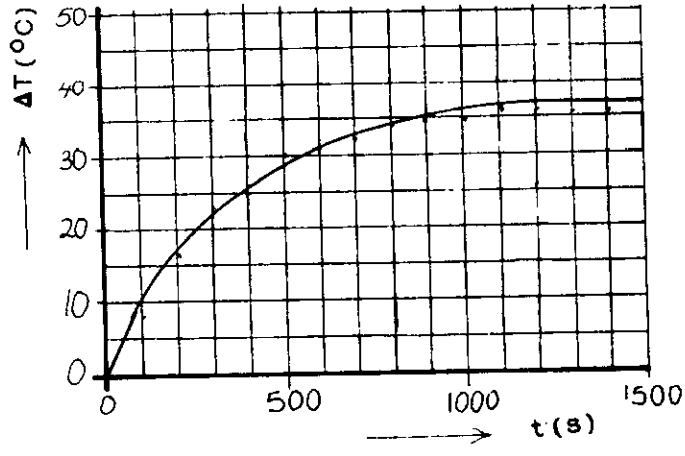

d_w = 33 mm, V_g = -20 kV, τ = 210 s.
d_p = 73 mm, I_w = -270 μA, I_h = 0.6 A.
s_w = 25 mm, I_p = -4.1 μA.

Fig. 50

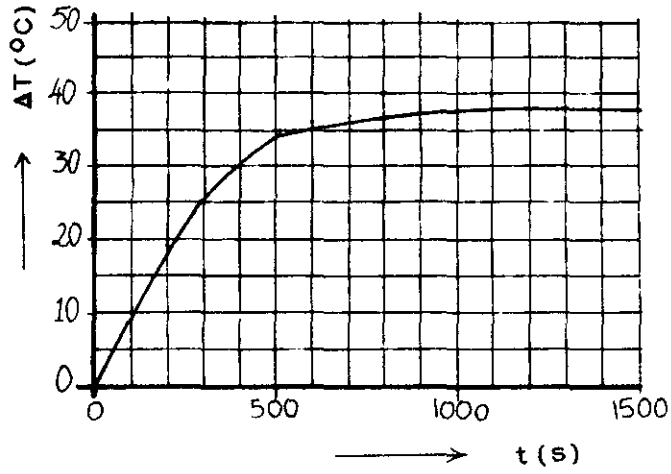

d_w = 28 mm, V_g = -20 kV, τ = 230 s.
d_p = 73 mm, I_w = -600 μA, I_h = 0.6 A.
s_w = 15 mm, I_p = -0.1 μA.

Fig. 51

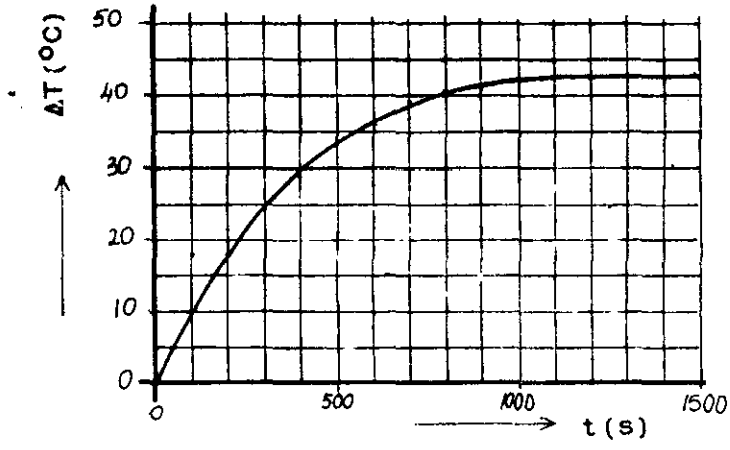

d_w = 33 mm, V_g = -20 kV, τ = 260 s.
d_p = 83 mm, I_w = -250 μA, I_h = 0.6 A.
s_w = 15 mm, I_p = -0.1 μA.

Fig. 52

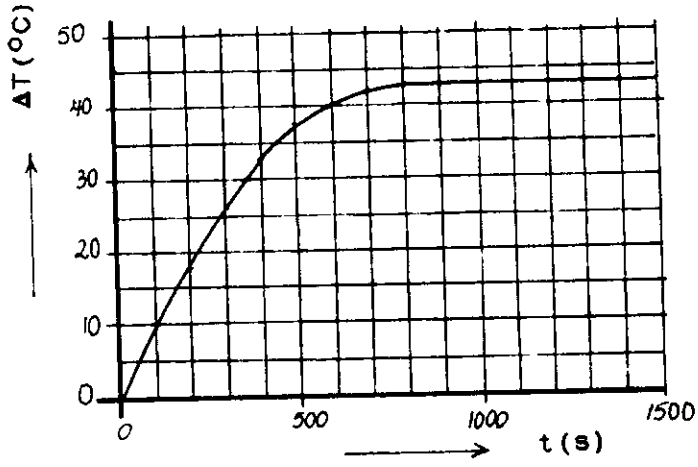

d_w = 33 mm, V_g = -20 kV, τ = 290 s.
d_p = 93 mm, I_w = -270 μA, I_h = 0.6 A.
s_w = 15 mm, I_p = 0.0 μA.

Fig. 53

The temperature rise of the heat transfer surface can be expressed by a general type of a differential equation

$$J = a \cdot \frac{d\Delta T}{dt} + \frac{\Delta T}{b} \quad . \tag{45}$$

Where J, a, and b are constants which will be defined later and ΔT is the temperature rise of the plate at time t.

A solution of Eq. (45) is

$$\Delta T = J \cdot b \cdot (1 - e^{-t/ab}) \quad .$$

After substitution of

$$\tau = a \cdot b$$

It follows that

$$\Delta T = J \cdot b \cdot (1 - e^{-t/\tau}) \quad . \tag{46}$$

Where τ is the time constant.

Let P_{in} be the constant power input to the heating elements which is wholly transferred to the heat transfer surface in Watts, and let R_{th} be the thermal resistance of the solid gaseous interface, which is determined by the convective heat transfer coefficient h, according to

$$R_{th} = 1/A \cdot h \quad . \tag{47}$$

Let also m be the mass of the heat transfer surface, and c_h be the specific heat capacity of the heat transfer surface.

If we assume that only a negligible amount of heat is stored in the material of the heating element and

that all heat is lost by convection through the plate,

$$P_{in} = c_h \cdot m \cdot \frac{d\Delta T}{dt} + \frac{\Delta T}{R_{th}} \quad . \tag{48}$$

Therefore,

$$\Delta T = R_{th} \cdot P_{in} \cdot (1-e^{-t/\tau}) \quad . \tag{49}$$

with

$$\tau = c_h \cdot m \cdot R_{th}$$

At steady state Eq.(48) reduces to

$$P_{in} = \frac{\Delta T}{R_{th}} \quad .$$

If we substitute Eq. (47) in the above expression, we obtain

$$P_{in} = A \cdot h \cdot \Delta T \quad , \tag{50}$$

Eq. (50) can be rewritten as

$$h = \frac{P_{in}}{A \cdot \Delta T} \quad .$$

Keeping P_{in} and A constant, and denoting the convective heat transfer coefficient with no corona wind as h_n, and the convective heat transfer coefficient with corona wind as h_c, we see that

$$h_n = \frac{P_{in}}{A . \Delta T_n} \quad .$$

and

$$h_c = \frac{P_{in}}{A . \Delta T_c} \quad . \qquad (51)$$

where ΔT_n is the steady state temperature rise of the heat transfer with no corona wind directed at it, and ΔT_c is the steady state temperature rise of the heat transfer surface with corona wind directed at it. Therefore the percentage enhancement of convective heat transfer over natural convection due to corona wind blowing to a heat transfer surface is

$$\Xi = \frac{h_c - h_n}{h_n} \cdot 100 \text{ percent} \quad .$$

or alternatively,

$$\Xi = \frac{\Delta T_n - \Delta T_c}{\Delta T_c} \cdot 100 \text{ percent} . \qquad (52)$$

The experimental results of Fig. 44 to Fig. 53 are summarized in Table II.

TABLE II: Summary of Experimental Results

Fig. No.	I_h	ΔT_n *	ΔT_c	Ξ	τ with corona wind**
	(A)	oC	oC	percent	(s)-1
45	0.5	66	31.0	112.9	340
45	0.6	76	43.0	76.7	340
45	0.7	93	62.0	50.0	280
46	0.6	76	41.5	83.1	190
47	0.6	76	43.5	74.7	230
48	0.6	76	42.5	78.8	240
49	0.6	76	37.0	105.4	280
50	0.6	76	36.0	111.1	210
51	0.6	76	38.0	100.0	230
52	0.6	76	42.5	78.8	260
53	0.6	76	42.5	78.8	290

* From Fig. 44.

** For values of τ with no corona wind , see Fig. 44.

3.6.3 Discussion of Experimental Results

From Table II, we conclude that corona wind has a significant influence on heat transfer at a solid gaseous interface when a corona wind is directed to a heat transfer surface which is heated by a constant inflow of energy. The convective heat transfer coefficient is enhanced by up to 112.9 percent. Temperature drops of the heat transfer surface of up to 40°C are recorded. The thermal time constants for heating up the heat transfer surface are also reduced by up to 65.4 percent. It must be mentioned here that the degree by which the corona wind enhances heat transfer from the heat transfer surface is dependent upon the following factors:

-The orientation of the heat transfer surface: It matters for example if the heat transfer surface is facing upwards, sideways, downwards , or placed inside an oven.

Because of the orientation of the heat transfer surface natural convection may be augmented by corona wind or hindered by it. When the heat transfer surface faces upwards, the natural convection driving force acts upwards. The convective heat transfer coefficient due to natural convection is substantial in this case. Corona wind when applied, creates heat convection cells. When the heat transfer surface faces downwards the driving force in natural convection acts upwards and the warm air can only move sideways. The convective heat transfer coefficient due to natural convection is lower compared to the previous case. Therefore the application of corona wind will enhance convective heat transfer more significantly in the latter case. When the heat transfer surface faces sideways the warm air rises upwards due to natural convection.

In this case when corona wind blows at the heat transfer surface from the side it augments natural convection. In an oven, heat transfer due to natural convection is very dependent on the temperature distribution and takes place very slowly where the temperature differences are very small. When corona wind is applied in an oven there is a constant driving force which depends on corona current only. Therefore equalisation of temperatures in the oven becomes faster.

-Temperature difference between the heat transfer surface and the ambient: At higher temperature differences between the heat transfer surface and the ambient the cofficient for natural heat convection is substantial as it is proportional to the said temperature difference. Therefore the heat convected away due to natural convection increases more than linearly with increasing temperature difference with the ambient as is implied by Eq.(3). At higher absolute temperatures of the heat transfer surface radiation becomes more significant. From Eq. (2) the net heat lost by radiation is given by

$$q_{nr} = \sigma(T_p^4 - T_a^4) \quad . \tag{53}$$

Here q_{nr} is the net heat which is radiated away by the heat transfer surface, σ is Stefan's constant, T_p is the absolute temperature of the heat transfer surface and T_a is the absolute ambient temperature. The general dependence of the enhancement of heat convection on the temperature of the heat transfer surface has been verified by results in the first three rows of Table II where it is shown that an

three rows of Table II where it is shown that an increase of the temperature of the heat transfer surface T_n by only 27°C reduces the enhancement of convective heat transfer coefficient by 56 percent.

From Fig. 46 to Fig. 53 we note that the cooling effect of the corona wind which is directed at a heat transfer surface depends on the configuration of the EWS. From Table II we see that the optimum configuration for the EWS is approximately that indicated in Fig. 50. The dependence of heat convection on the configuration of the EWS is important because of two reasons. Firstly the configuration of the EWS determines the magnitude of the corona current according to Eq. (11), the corona current in turn is related to the average corona wind velocity according to Eq.(29a), which determines the convective heat transfer coefficient h acccording to Eq. (5). Secondly it is important that the wires be positioned such that they do not reduce very much the velocity of the corona wind in the central core of the corona wind. In Fig. 51 for example, the wires are very close to each other and hence diminish the effectiveness of the high corona current generated by the EWS.

3.7 The Corona Triode

The corona triode is studied to clarify whether ions reaching the plate could have an effect on the heat transfer. In contrast to the EWS, studied up till now, the corona triode allows us to direct more ions to the plate.

3.7.1. General Remarks

The corona triode which is shown in Fig. 54 has been used in a number of scientific measurements and applications.

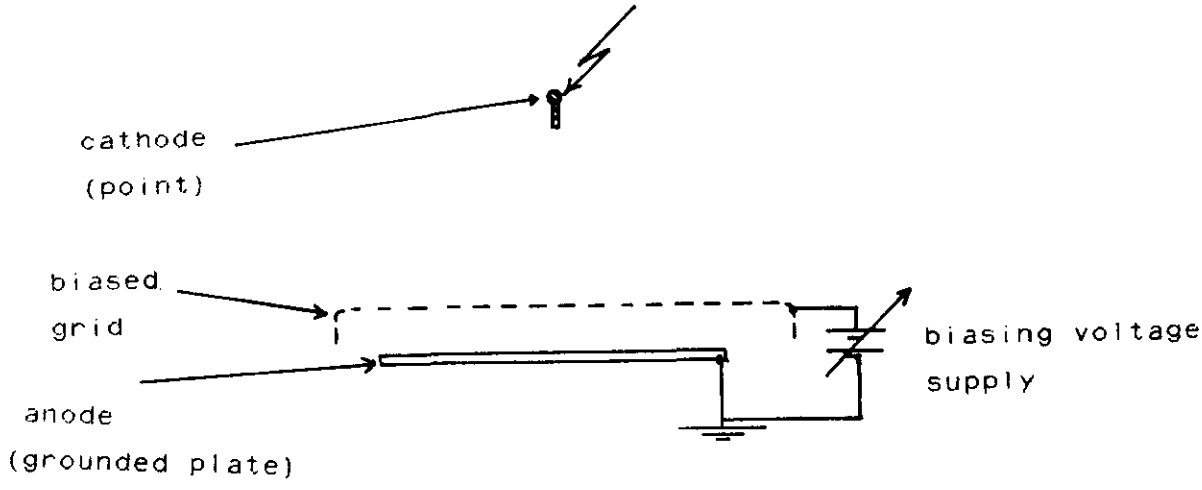

Fig. 54: Corona triode.

Hayne [95] has used the corona triode to control the charging level of a photo-receptor in a xerographic copier. Goldman et al [96] have used the corona triode to measure the mobility spectra of ions produced in a corona discharge, while Masuda et al [97] have used it in the study of the initiation conditions and mode of

back discharges in electrostatic precipitators. Withers et al [98] have used the corona triode to stop the corona wind in their study of aerosols which are subjected to an electrostatic field in a corona discharge. Allen et al [99] have used the corona triode to study the ionic species formed in a corona wind. Gross et al [100] have used the corona triode to implant ions in thin polymer films. Bradley et al [101] have used the corona triode to study the effect of temperature distribution on electrohydrodynamic driven instabilities.

Mclean et al [102] have developed a theoretical model which describes the electrical current transparency D_e of the biased grid of a corona triode. The electrical current transparency of the grid is defined as

$$D_e = \frac{j_p}{j_o} \quad . \tag{54}$$

Here j_p is the current density to the anode which has crossed the grid and j_o is the current density in the corona discharge region measured before the grid. In their model, current penetration through a biased grid is solely a function of the field penetration from the cathode through the grid. Furthermore they show that this field penetration is a function of the field E_g between the grid and the anode, the field E_o adjacent to the grid in the corona discharge region, and the optical transparency of the grid D_o related to the construction of the grid. The measurements presented here show that D_e does not depend on the field penetration through the grid alone, but is strongly

dependent on the corona wind velocity also. This result is in agreement with Haug [103].

According to Haug et al [103-106] the electrical current transparency of the grid in a corona triode depends on the ionised gas velocity upstream of the grid, the mobility of the ions, the optical transparency of the grid, and the fields E_o and E_g. These authors give a mathematical expression for D_e which gives values that seem to describe experimental measurements rather well.

Oliveira et al [107] have shown that the plate current I_p is a space charge limited current (SCLC) for low grid-anode attracting voltages and I_p is only determined by D_e for higher grid-anode attracting voltages because the corona current then remains smaller than the SCLC in the grid-anode spacing. These authors show further that the neccessary cut-off voltage V_r which will reduce I_p to zero is given by

$$V_r = \frac{u \cdot l}{K} + V_f \quad , \tag{55}$$

where u is the corona wind velocity, l the grid-anode spacing, K the ion mobility, and V_f is the quasi-potential which simulates the anode current caused by field penetration through the grid. The value of V_f is given by [108].

$$V_f = E_o \frac{a}{2\pi} \left[1 + \mathrm{Ln}(a/2\pi r)\right] \quad . \tag{56}$$

where a is the spacing between wires of the grid

and r is the radius of the wires of the grid.

This section reports on our experimental investigation of the penetration of ions through the grid of a corona triode.

3.7.2. Experimental Setup.

The experimental apparatus consists of a corona triode in which the cathode is formed by a 90 degrees flat aluminum edge. The grid is a copper mesh of 60 percent optical transparency. To allow for unhampered flow of air we used a square meshed grid instead of a plate as anode. A Pitot-tube is positioned at the anode in a hole of 20 mm diameter. A flat copper disk cap of 15 mm diameter is fitted to the Pitot-tube to collect ions for current measurements. The Pitot-tube forms a part of the velocity measuring system, while the copper cap collects a part of the anode current, and forms a part of the anode current detection system. This enables us to measure current and velocity at one point simultaneously. The grid is biased by a 0-400 Vdc power supply. The anode is grounded, and hence serves also as a guard ring. The experimental arrangement is depicted in Fig. 55.

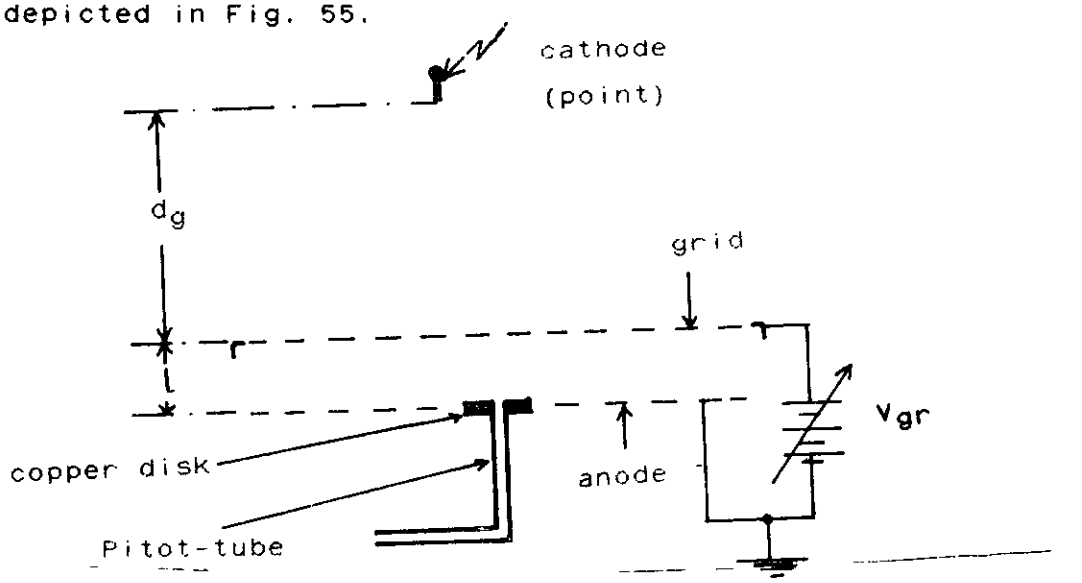

Fig. 55: Experimental setup.

3.7.3 Experimental Results

Fig. 56 shows the current characteristics for low anode currents only. These curves are similar and parabola-like, which as observed by Oliveira indicate that the anode is space charge limited.

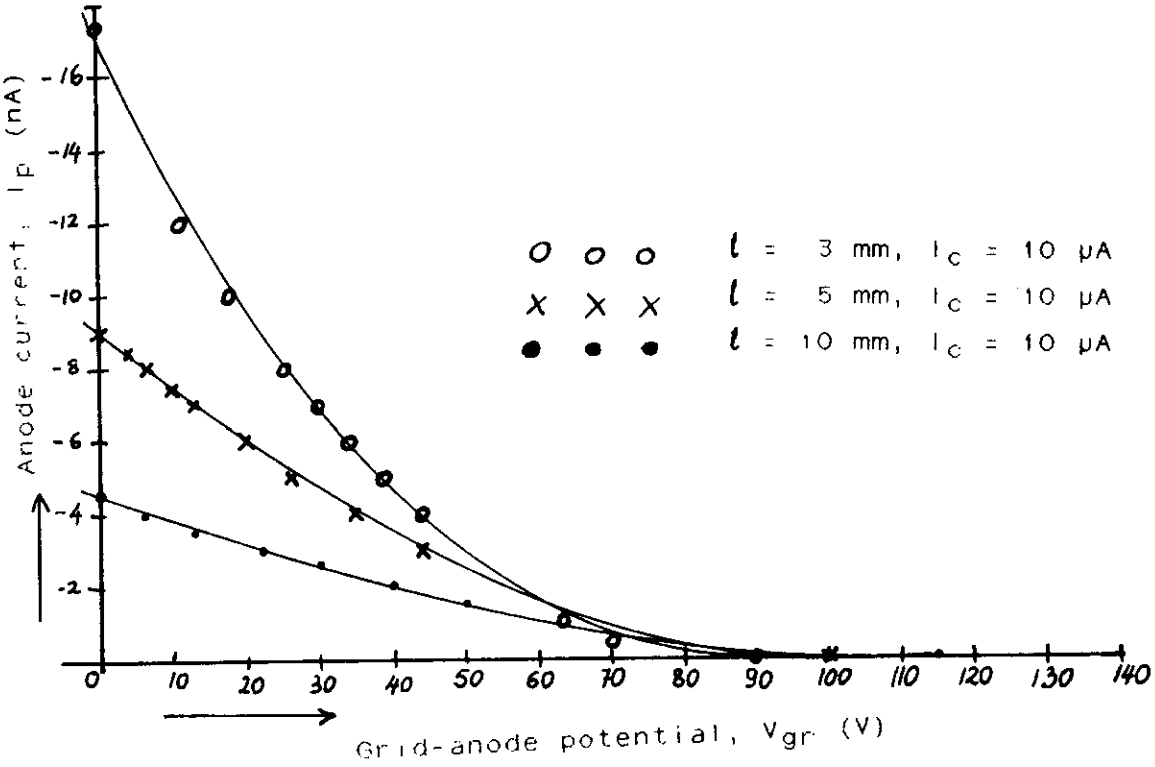

Fig. 56: Anode current (I_p) vs grid-anode voltage (V_{gr}) characteristics of the corona triode, for three values of the grid-anode spacing l. Note: Only a small fraction of the 10 μA corona current reaches the measuring disk in the anode plane.

Fig. 57 shows the cut-off grid-anode potential as a function of the gap spacing l between the grid and the anode.

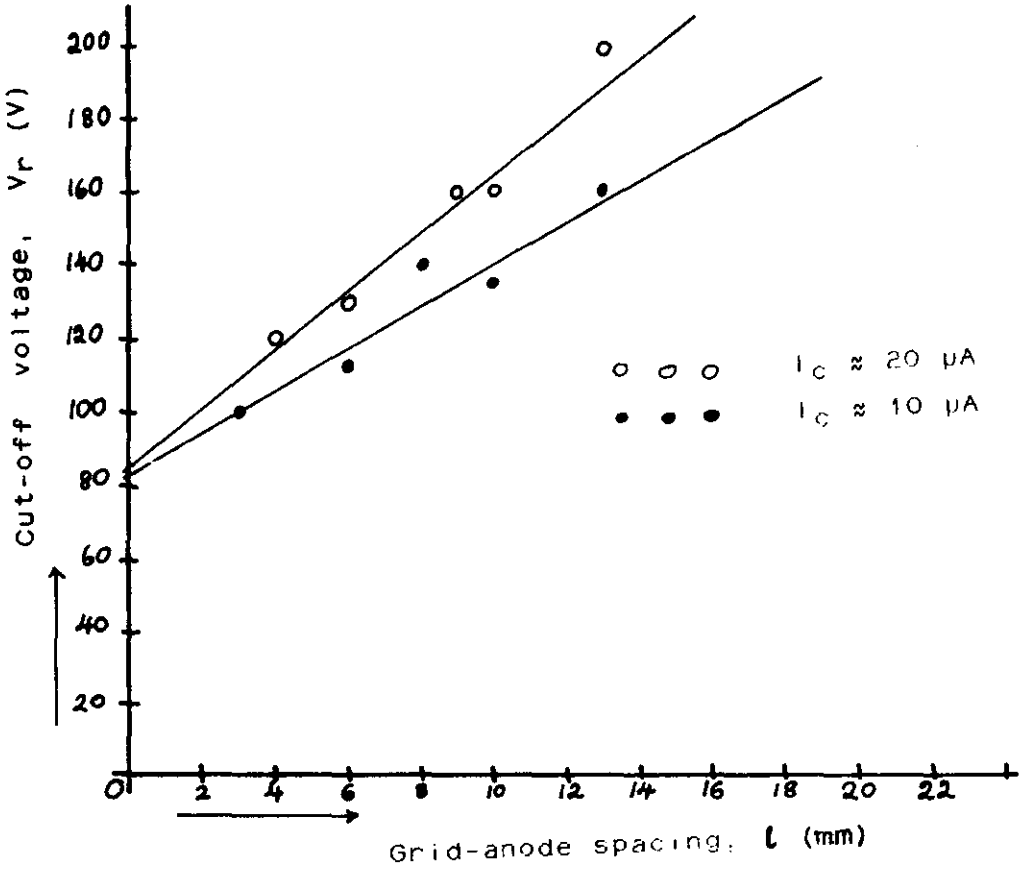

Fig. 57: Cut-off voltage (V_r) vs grid-anode gap length (l) .

Fig. 58: shows the corona wind velocity on axis u_{max} as a function of anode current I_p.

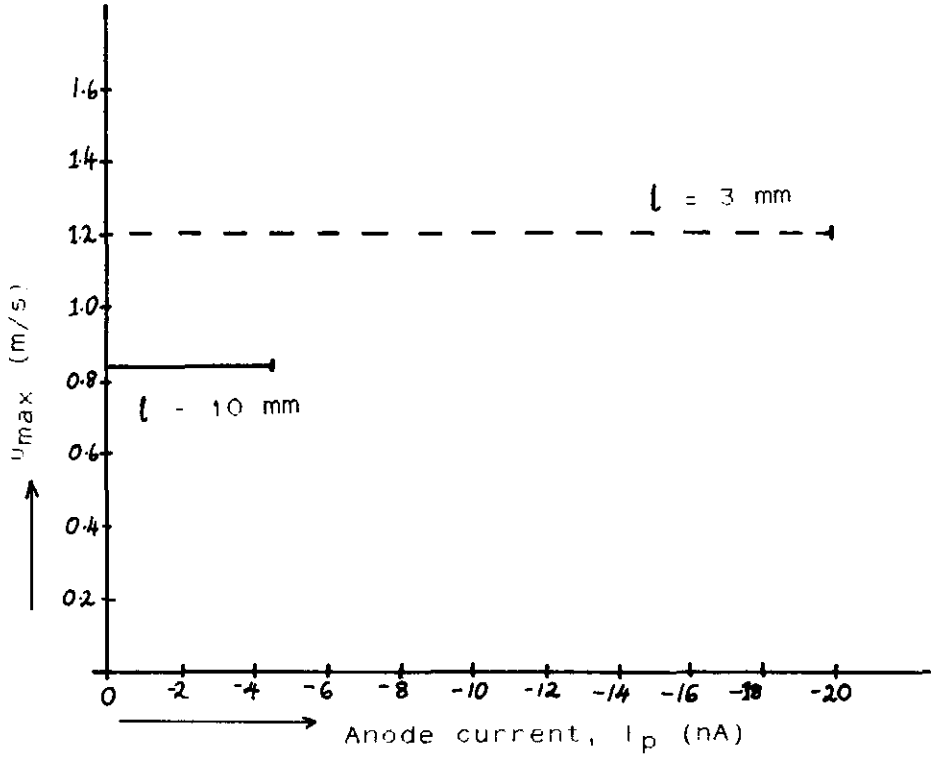

Fig. 58: Corona wind velocity on axis (u_{max}) vs anode current (I_p) characteristic of the corona triode. I_c = -10 μA.

3.7.4 Discussion of Experimental Results

From Fig. 56 we see that for low current densities,

the anode current I_p is indeed a space charge limited current. If we start with the classical equations $j = \rho u_i$, $\nabla . j = 0$, $\nabla . E = \rho/\epsilon_o$; and use the ion motion equation $u_i = u + KE$, we arrive at the unidimensional solution of these equations,

$$j = \frac{9K\epsilon_o}{8l^3}\left[V_{gr} + \frac{ul}{K}\right]^2 \quad . \tag{57}$$

We can write the unidimensional solution of these equations as a new expression for the space charge limited currrent in the presence of the corona wind.

$$j = \frac{9K\epsilon_o}{8l^3}V_{gc}^2 \quad . \tag{58}$$

where,

$$V_{gc} = V_{gr} + \frac{u \cdot l}{K} \quad .$$

Following Oliveira the term V_{gc} might contain an addditional term V_f to describe the effect of field penetration through the grid. That is to say

$$V_{gc} = V_{gr} + \frac{u \cdot l}{K} + V_f \quad .$$

Equation (58) represents a generalized form of the Child-Langmuir law [109] .

From Fig. 57 we see a linear increase of the cut-off voltage V_r with an increasing grid-anode spacing and corona wind velocity as was stated in Eq.(55). The intercept value in Fig. 57 is V_f , the quasi-potential due to field which has penetrated through the grid from the cathode.

Fig. 58 indicates that the magnitude of the current I_p in the grid-anode spacing does not appreciably alter the velocity of the corona wind. This is because the anode current density is normally very small. The grid-anode spacing is also much smaller than the corona gap length. The effect of current density and spacing between grid and anode to the generated corona wind velocity can easily be understood if one refers to Eq.(23).

3.8 Heat Transfer Measurements With Corona Triode Used to Control the Magnitude of Current Collected by the Heat Transfer Surface

The enhancement of convective heat transfer by corona wind blowing on a flat upward facing heat transfer surface is measured. The corona triode is used to create the corona wind and to control the magnitude of the ionic current collected by the heat transfer surface. The effect of the interaction of the ionic current and the heat transfer surface is investigated and conclusions are drawn.

3.8.1 Principles of Measurements

The experimental setups are shown in Fig. 59 and Fig. 60. The heat transfer surface is an upward facing aluminum plate which is heated from below by electrical heating elements. Three heating elements are connected in series to the temperature controlled 220 V ac power supply. Glass wool or/and styrofoam provide thermal insulation to ensure that heat is only lost through the upper surface. A narrow airgap separates the plate from the heating elements.

If the temperature of the plate is maintained constant with the help of thermocouples installed in the plate the following relation must be correct, averaged in time

$$P_{in} = A \cdot h \cdot (T_p - T_a). \qquad (59)$$

Here P_{in} is the average electrical power input to the plate at constant temperature T_p of the plate, A the surface area of the plate, T_a the ambient temperature, and h the convective heat

transfer coefficient.

If the temperature of the plate, the ambient temperature, and the surface area of the plate are kept constant, then the average electrical power input P_{in} varies directly with the convective heat transfer coefficient h. Power losses by radiation and convection from the edges of the plate also remain constant when we change the parameters of the corona discharge, and therefore cancel out.

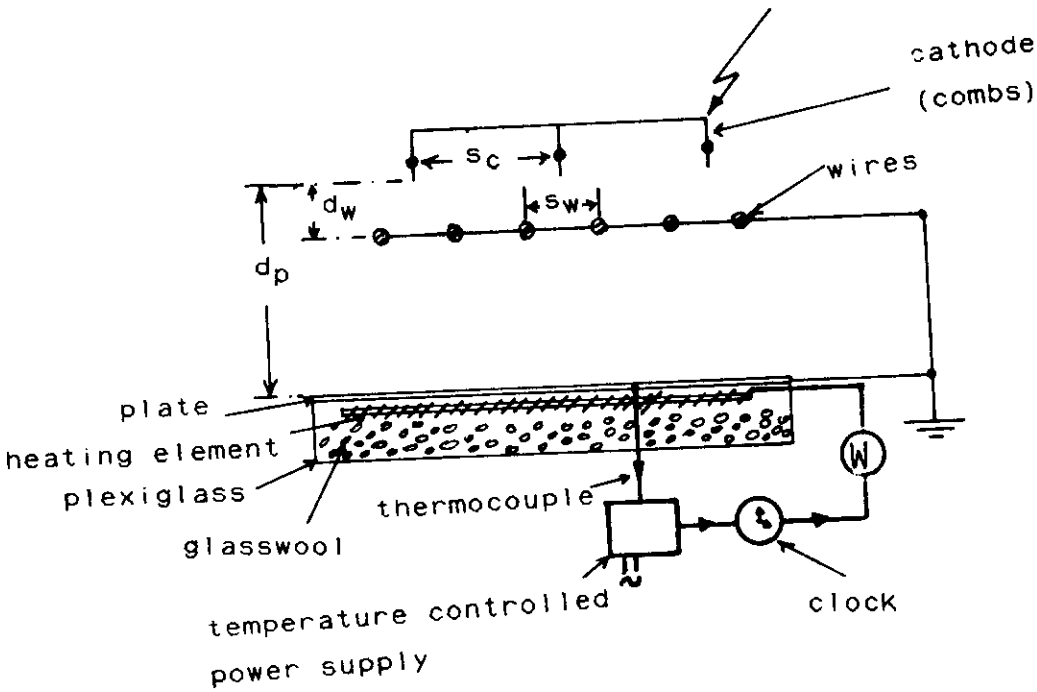

Fig. 59: Experimental setup for the measurement of the enhancement of convective heat transfer by corona wind.
d_w = 35 mm, d_p = 92 mm,
s_c = 30 mm, s_w = 12 mm.
3X Combs, each 25 teeth.
Heat transfer surface 450 X 290 mm².

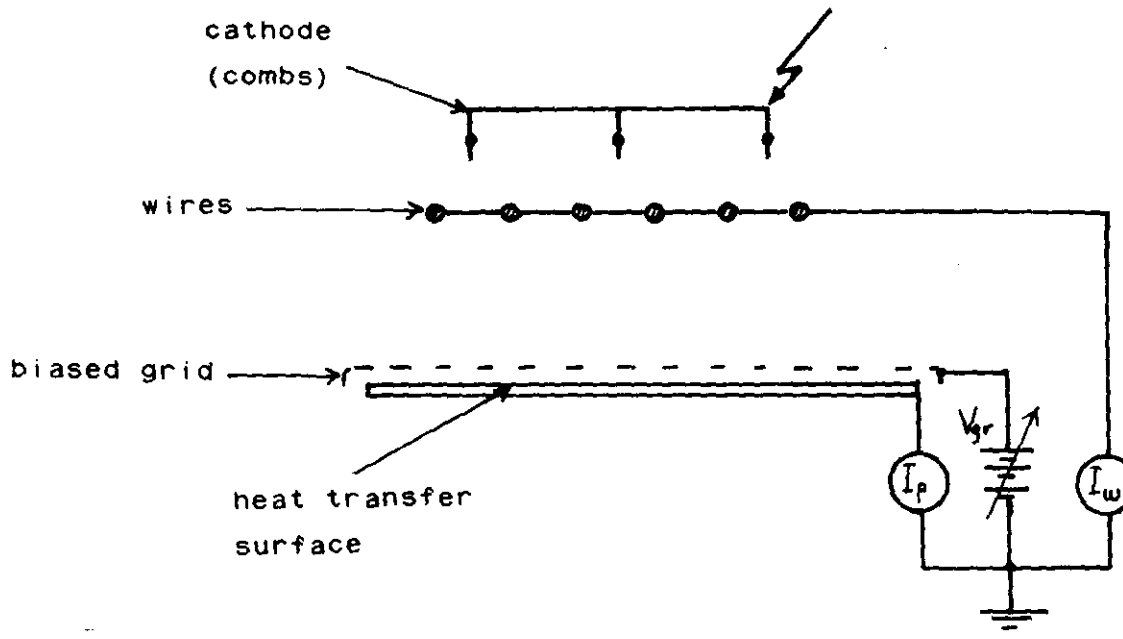

Fig. 60: Experimental setup to measure the effect of I_p on the enhancement of the convective heat transfer coefficient.
d_w = 35 mm, d_p = 92 mm,
s_c = 30 mm, s_w = 12 mm.
Distance between grid and heat transfer surface l = 1 mm.
3X Combs, each 25 teeth.
Heat transfer surface 450 X 290 mm².

The power supply to the heating elements is thyristor controlled. The temperature of the plate is maintained constant by switching on and off complete cycles of the ac voltage supply to the heating elements. The electrical clock only measures the time t_p when power is supplied to these heating elements. Therefore if it is assumed that the heating elements consume constant power P_h, the average power P_{in} to the heating elements is given by

$$P_{in} = P_h \cdot \frac{t_p}{t_c} \quad . \tag{60}$$

Here t_c is the total length of time the plate is maintained at a constant temperature.

3.8.2 Experimental Results

Measurements of the plate current (the current which is collected by the heat transfer surface) I_p as a function of the grid voltage V_{gr} for the experimental setup shown in Fig. 60 are shown in Fig. 61. These measurements were done with a gap voltage V_g at the combs of -20.1 kV and a total corona current I_c of -330 μA.

Fig. 62 shows plots of the power input to the heating elements P_{in} (which is directly proportional to the heat transfer coefficient h) as a function of corona current I_c.

Table III is a presentation of more measurements to investigate the mechanism of the enhancement of the heat transfer by corona wind.

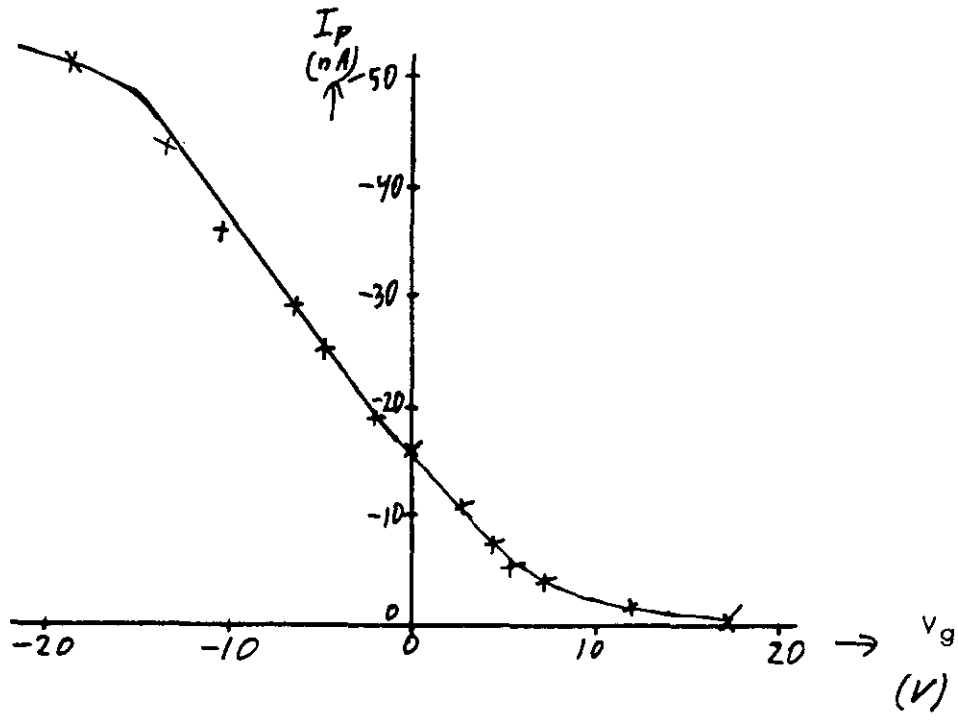

Fig. 61: I_p vs V_{gr} for the experimental set up of Fig. 60; V_g = -20.1 kV, I_c = -330 μA.

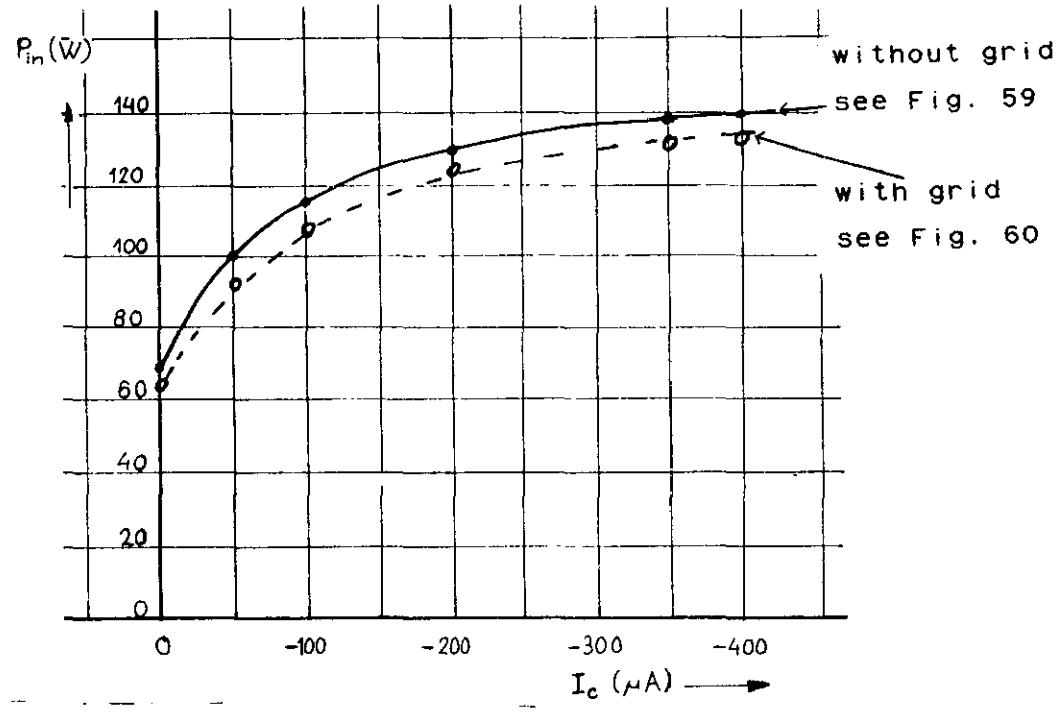

Fig. 62: P_{in} vs I_c. P_{in} is directly proportional to h. $T_p - T_a$ = 32°C.

Table III: Heat Transfer Measurements

No	t_c (min)	V_g (KV)	I_c (μA)	I_p (nA)	V_{gr}* (V)	P_{in} (W)	ΔT (^oC)	h** (W/m² ^oC)
1	20	-19.8	-330	-16	0	129.6	32	26.8
2	20	-19.8	-330	0	+135	130.1	32	26.9
3	10	-20.0	-330	-16	0	128.7	32	26.7
4	10	-19.0	-330	-58	-44	129.9	32	26.9
5	10	-19.5	-330		--	129.5	32	31.0
6	10	0	0		--	71.5	32	17.1
7	10	-11.9	0		--	72.0	32	17.2
8	10	-16.8	-100		--	114.6	32	27.4
9	10	-16.8	-200		--	124.5	32	29.8
10	10	-15.6	-50		--	101.6	32	24.3

* The V_{gr} vs I_p plot is shown in Fig. 61, "--" means there is no grid in position.

** Surface area of heat transfer surface is 0.1305 m².

3.8.3 Discussion of Experimental Results

From Fig. 62 or Table III rows No. 5, No. 8, No. 9, and No. 10, we conclude that the enhancement of heat transfer increases with the corona current.

From Table III rows No. 6, and No. 7 we conclude that the convective heat transfer coefficient remains constant when no corona current is flowing. Therefore the augmentation of the hydrodynamic flow of the air, which is caused by the flow of corona current, is responsible for this enhancement of convective heat transfer.

In the experimental measurements, the grid which is used in an experimental setup reduces the corona wind, which minimizes the effect of corona wind on thermal convection at the plate. One of the plots in Fig. 62 indicates this phenomenon.

From Table III rows No. 5 and No. 6 we see that the convective heat transfer coefficient is enhanced by up to 90 percent when corona wind is blown to the heat transfer surface.

From Table III rows No. 1, No. 2, No. 3, and No. 4, we see that V_{gr} and consequently I_p have no effect on heat transfer at a heat transfer surface which is blown at by corona wind. (Fig. 61 shows the V_{gr} vs I_p curve for this experimentai setup .) We can explain this phenomenon as follows: measurements in section 3.1 of this thesis have indicated that the largest part of the corona current is collected by the wires. On the other hand measurements in section 3.7 of this thesis have indicated that there is a very small potential drop between the wires (a grid) and the plate of a corona triode. From these two measurements it may be concluded that any further augmentation of the

corona wind past the grid by the ions which reach the plate is too small to have any effect on the coefficient of heat transfer as has been discussed above. Another effect of the ions reaching the plate could have been due to their potential energy of ionization which the ions release when they get neutralized at the plate. The ionization energy carried by these negative ions is at most a few eV. Note that positive ions have a higher ionization energy, of the order of 10 eV. On reaching the plate the negative ions are neutralized, but since the plate current is very small the net energy which is released by the neutralization of the ions at the plate is too small to be of any consequence (approximately 0.15 μW at 50 nA plate current).

From Eq. (29a) the average corona wind velocity is proportional to $I_c^{0.5}$. From Fig. 62 it can be deduced that h is proportional to $I_c^{0.3}$. So it may be concluded that h due to corona wind is proportional to $u_{av}^{0.6}$. This compares favourably with a mechanically generated jet where h is proportional to $u_{av}^{0.5}$ as was stated in Eq. (5).

CHAPTER IV CONCLUSIONS

The basic equations which govern the nature of corona wind are outlined in section 2.3. Corona wind is created when the Coulomb forces acting on ions are transferred by collisions to the neutral air molecules. Magnetic forces and electrical polar forces are negligible.

Most of the field lines from the ionisation region of an EWS terminate at the wires. Therefore most of the corona current is collected by the wires. The collection of most of the corona current by the wires of an EWS increases the magnitude of the geometrical constant in the classical corona current equation of Townsend for a point-to-plate geometry with a fixed point-to-plate spacing. As a result more corona current can flow before space charge limitation takes place, consequently the velocity of the corona wind increases. However the electrokinetic conversion efficiency of the EWS although better than for a point-to-plate geometry is low of the order of 3 percent. Most of the electrical energy is used in elastic and inelastic collisions, and ends up as heat.

The corona wind velocity distribution is bell shaped with an accentuated narrow peak. In the accentuated peak region the wind is created because the Coulomb forces on ions are trasferred to the neutrals as explained above, while around this region air motion is caused by viscous forces.

There is about one ion to 600 million neutrals in the corona wind. The effect of the ions on the thermal conductivity and viscosity of the air media is therefore negligible.

Corona wind is laminar, and consequently has a

rather small spread. Some wiggling behaviour is seen which may be caused by changes in the boundary conditions at the electrodes. In my setup the corona wind of one point is confined in an area of 2x4 cm^2. The corona wind has a long reach of up to 25 cm below the corona discharge points.

Mechanically created free jets are in comparison turbulent and divergent because of strong edge effects at the orifice and the resulting abrupt transition from pipe flow to free flow.

When a corona wind is superimposed on a mechanical jet, the jet becomes less turbulent.

The blowing of corona wind on a heated transfer surface has a significant cooling effect on the surface and enhances convective heat transfer from the heat transfer surface by up to 110 percent according to my measurements. Temperature drops of up to 40^oC of the heated surface were measured. The time constants for heating up the surfaces are also reduced by up to 65 percent. The degree by which the corona wind enhances heat transfer from a heated surface depends on the orientation of the heated surface and the temperature differences between the heated surface and the ambient. The importance of these factors is explained in section 3.6.3.

The configuration of the EWS can be optimized to generate maximum corona wind and at the same time a sufficiently wide opening between the wires to allow the corona wind to reach the heat transfer surface. In my measurements, the optimum configuration of the EWS turns out to be the one depicted in Fig. 50.

The Langmuir-Child equation for space charge limited current is generalized to include the case where the gas is in motion (section 3.7.4).

Corona wind enhances the convective heat transfer coefficient by augmenting the hydrodynamic flow. A possible empirical correlation between convective heat transfer and corona current is that the coefficient of convective heat transfer h from a heated upward facing surface which is blown at with corona wind is proportional to $I_c^{0.3}$ as outlined in section 3.8.3.

There is no contribution to the rate of convective heat transfer due to the interaction of ions with the heat transfer surface.

The laminar nature of the corona wind makes it more suitable than a mechanical jet in enhancing the convective heat transfer coefficient by blowing on flat heat transfer surfaces.

Further research should be directed into the effect of superimposing corona discharges on mechanically generated turbulent jets to reduce the turbulence of mechanically generated jets. A proper reduction of turbulence in mechanically generated jets, could make such applications possible.

Proc. 7th Int. Symp. on Plasma Chemistry, Eindhoven, 1-5 July 1985. Ed. by C.J. Timmermans. Dept. of Technical Physics, Eindhoven Univ. of Technology, 1985. P. 522-527.

ENHANCEMENT OF HEAT TRANSFER BY CORONA WIND

H. Kadete*, P.T.M. Vaessen and P.C.T. van der Laan
High-Voltage Laboratory, Department of Electrical Engineering,
Eindhoven University of Technology, Eindhoven, The Netherlands.
* Department of Electrical Engineering,
University of Dar es Salaam, Dar es Salaam, Tanzania.

ABSTRACT

The convective heat transfer to or from a solid, can be significantly enhanced by a nearby corona discharge, through the interaction of the corona wind with the thermal boundary layer. Experimental measurements with a number of measuring techniques have shown that this interaction can be effective because the corona wind flows in quite laminar jets with a long reach and a small spread.

1. INTRODUCTION

The enhancement of heat transfer across solid-gaseous interfaces by a nearby corona discharge has been known since 1899 (Chattock). In the 1960's increases of the heat transfer coefficient by about a factor four above that for natural convection were measured. This resulted in an intense research on this process throughout the world [1,2]. Nowadays several patents exist on the practical application of this phenomenon. The heat transfer augmentation process is however, not yet clearly explained. The corona wind itself, the character of the stream, the interaction of charged particles with the target object, or a combination of these factors may be responsible. The aim of this paper is to find the predominant factors wich cause the observed heat transfer enhancement. New applications of corona wind and an optimization of already existing apparatus are then possible. Throughout the paper we employ S.I. units.

2. THEORY

In a corona discharge the ionization takes place in a very small region near the electrode with the smallest radius of curvature. If this electrode is negative and if an attaching gas is present in the gap, rapidly drifting negative ions are formed. These ions make frequent collisions with the neutral molecules, so that they acquire a constant

drift velocity. The force caused by the electric field is then completely transferred to the neutral gas. This is the essential element in the ion drag theory [3]. The flow created in this manner, the so called corona wind, resembles a jet flow. The body force,

$$F = \rho_c E, \qquad (1)$$

in which ρ_c is the charge density and E the electric field strength, is a function of the location within the jet flow and acts throughout the entire region between the electrodes. This force couples the electrical and fluid dynamical behaviour of the corona discharge and shows up as a source term in the Navier-Stokes equation [4]. The equations governing the electric, velocity and temperature field form a large set of coupled partial differential equations. The boundary conditions have a large influence on the nature of the flow field but are often difficult to formulate.

3. EXPERIMENTAL SETUP

The electric wind system as shown in Fig. 1 consists of a flat 90 degree, 1 mm thick brass edge and two parallel stainless steel rods of 5 mm diameter. In this system d is the distance between the two rods and S_1 the distance between the point and the plane of the rods. In commercially used electric wind systems of this type (The METC-system, INTER-PROBE Inc., Chicago) a flat plate is placed a distance h below the rods; this plate may be the heat transfer surface in an oven. We consider the point to be the center of a right handed cartesian coordinate system where the x-axis is normal to the plane. A negative high voltage is applied to the point. The discharge is a negative corona discharge of the "Trichel-type", in atmospheric air [5].

4. MEASUREMENTS

Electrical measurements. Figure 2 shows the current drawn to the rods versus the negative voltage applied to the point. The voltage current characteristic follows the well known empirical formula [6]:

$$I_1 = K_1 V(V-V_s). \qquad (2)$$

I is the current to the rods, V is the voltage applied to the point, V_s is the corona starting voltage and K_1 is a constant with dimensions AV^{-2}. When a grounded heat transfer plate is placed some distance below the rods and the current, I_2, drawn to this surface is measured we observe that:

$$I_2 << I_1 \quad \text{and} \quad I_2 = K_2 (V-V_s). \qquad (3), (4)$$

K_2 is a constant with dimensions AV^{-1}. The current I_2 is small which indicates that almost all ions reach the grounded rods. This is also confirmed by the hot-wire anemometry measurements.

Pitot-tube measurements. The velocity of the corona wind is determined by measuring the pressure difference in accordance with Bernoulli's equation:

$$\Delta p = \tfrac{1}{2}\rho u^2, \qquad (5)$$

Δp is the difference between ambient pressure and stagnation pressure, ρ is the mass density of air and u is the air velocity. The Pitot-tube was placed behind a grounded wire mesh of 59.2% transparency and corrections were made for the disturbances created by this wire mesh. The measurements show a bell shaped velocity profile with a typical peak air velocity of 4.5 ms^{-1}. In the absence of the grounded rods the velocity profile remains bell shaped with in addition a sharp accentuated peak at the center, and lower air velocities.

Hot-wire anemometry. Anemometer measurements are based on a measurement of the convective heat-loss from an electrically heated fine wire [7]. Measurements of air velocities down to 0.2 ms^{-1} are possible. The hot-wire anemometry showed a reach of the jet of at least 25 cm for V = -20 kV and S_1 = d = 30 mm and a relatively small cross section of the jet (typical size 10 cm^2) which shows little spreading downstream. The velocity profile as shown in Fig. 3 is bell shaped and the average wind velocity is proportional to the applied voltage V for voltages well above the corona starting voltage V_s. Only low frequencies, less than 1 kHz, were present in the anemometer output signal. No significant differences between the readings of a "shielded" and an "unshielded" hot-wire sensor were observed for wire to rod distances greater than the rod to rod spacing d. The grounded shielding devices for the hot-wire sensor should divert charged particles away from the wire. An additional test was to measure the current drawn by an unshielded hot-wire sensor placed at a distance less than d below the plane of the rods; even then its current was less then 0.05 μA. This confirms that most of the ions flow to the two grounded rods.

Schlieren diagnostics. A Schlieren setup provides an optical visualization technique in which the intensity of the transmitted light depends on the gradient of the air density [8]. In our experiments we had to heat the corona electrode to generate the necessary air density variations. Photograph 1 shows a Schlieren picture of a corona wind jet. The photograph shows a stable flow pattern; the actual jet is wider than is shown in the picture,

because the hot air comming from the heated point is concentrated in the center of the jet.

Artificial mist. We also used a mist produced by solid CO_2 to visualize the air flow in an electric wind system. Photograph 2 shows a picture where the mist is introduced downward into the electric wind system through 11 small holes in the wall of a tube parallel to the rods. From the artificial mist experiments we obtained the following conclusions:

- the velocity profile has a small diameter ($\approx$ 35 mm)
- the flow is stationary within two seconds after the application of the negative high voltage.
- the generated jet has a much more laminar character than a jet originating from an orifice.

This last conclusion is in full agreement with the results from Schlieren and anemometer measurements. A difficulty in the comparison of an "orifice jet" and a corona wind jet is the question which parameter should be the same in both jets. Nevertheless the conclusion is quite general, since a longer reach, a smaller spread and a lower turbulence was seen in all measurements on corona wind jets.

Heat transfer measurements. Figure 4 shows some results of heat transfer measurements on a heated horizontal copper plate with dimensions 220 x 170 mm. The electric wind system used here consists of 75 discharge points as in Fig. 1, arranged in five rows of 15 teeth parallel to the rods. The temperature rise ΔT with a heating input of 44 W decreases by a factor two after the electric wind system has been energized. The electric power input to the corona discharge is 5.4 W. This observed increase in the heat transfer coefficient is in this case only a factor two, because the free natural convection upward from the horizontal plate is appreciable. Preliminary optimization with respect to the parameter d shows that maximum heat transfer takes place for d $\approx$ 25 mm, for S_1 = 33 mm. The other parameters S_1 and h have only a weak influence on the heat transfer.

5. DISCUSSION AND CONCLUSIONS

A jet generated in an electric wind system is more laminar, spreads less and has a longer reach than a jet originating from an orifice. The reason for this is that the smoothly distributed body force acting in the corona wind generates much less initial disturbance than a sharp edge at the end of the tube in the case of an orifice jet. The conclusion must be that the enhancement of heat transfer is caused by the more laminar character and

the longer reach of the corona wind jet. The negative ions cannot contribute significantly to the heat transfer since very few ions reach the heat transfer surface.

REFERENCES

1 Robinson, M.
MOVEMENT OF AIR IN THE ELECTRIC WIND OF THE CORONA DISCHARGE.
AIEE Trans., Part 1, Vol. 80(1961) (=Commun. & Electron., No. 54), p. 143-150.

2 Mitchell, A.S. and L.E. Williams
HEAT TRANSFER BY THE CORONA WIND IMPINGING ON A FLAT SURFACE.
J. Electrostat., Vol. 5(1978), p. 309-324. Proc. 2nd Symp. on Electrohydrodynamics, Fort Collins, Colo., 16-18 Jan. 1978. Ed. by T.B. Jones.

3 Stuetzer, O.M.
ION DRAG PRESSURE GENERATION.
J. Appl. Phys., Vol. 30(1959), p. 984-994.

4 Kulacki, F.A.
ELECTROHYDRODYNAMIC ENHANCEMENT OF CONVECTIVE HEAT AND MASS TRANSFER.
In: Advances in Transport Processes. Vol. 2. Ed. by A.S. Mujumdar and R.A. Mashelkar.
New Delhi: Wiley Eastern, 1982. P. 105-147.

5 Goldman, M. and R.S. Sigmond
CORONA AND INSULATION.
IEEE Trans. Electr. Insul., Vol. EI-17(1982), p. 90-105.

6 Lama, W.L. and C.F. Gallo
SYSTEMATIC STUDY OF THE ELECTRICAL CHARACTERISTICS OF THE "TRICHEL" CURRENT PULSES FROM NEGATIVE NEEDLE-TO-PLANE CORONAS.
J. Appl. Phys., Vol. 45(1974), p. 103-113.

7 Bradshaw, P.
AN INTRODUCTION TO TURBULENCE AND ITS MEASUREMENT.
Oxford: Pergamon, 1971.
Commonwealth and international library: Thermodynamics and fluid mechanics. Chapter 5.

8 Merzkirch, W.
FLOW VISUALIZATION.
New York: Academic Press, 1974. Chapter 3.

ACKNOWLEDGMENT

The authors gratefully acknowledge the enthusiastic technical support by mr. P.F.M. Gulickx and the cooperation of the group Transport Physics of the Physics Department with the Schlieren measurements. The heat transfer measurements were carried out in Dar es Salaam with the assistance of mr. B.M.M. Mwinyiwiwa. These investigations have been financially supported by NUFFIC, as a part of the collaboration of the universities at Eindhoven and Dar es Salaam.

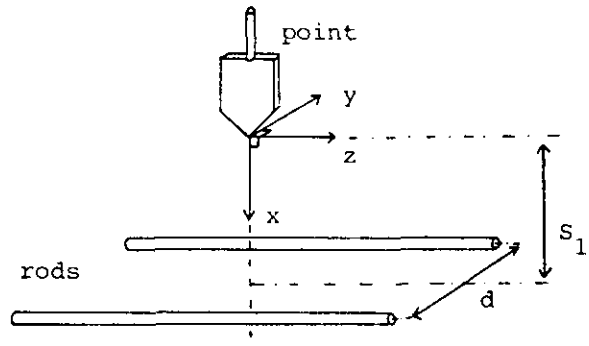

Fig. 1 Electric wind system.

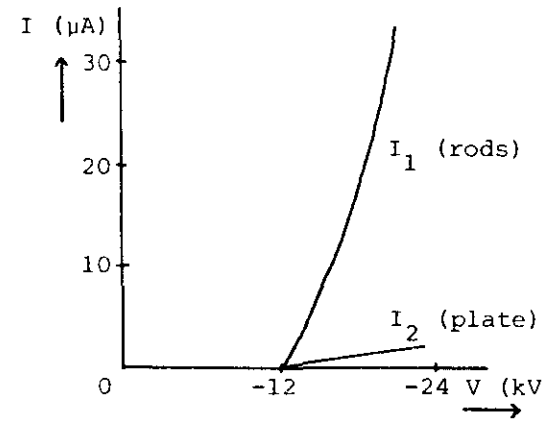

Fig. 2 Current versus applied voltage; S_1 = d = 30 mm and h = 60 mm.

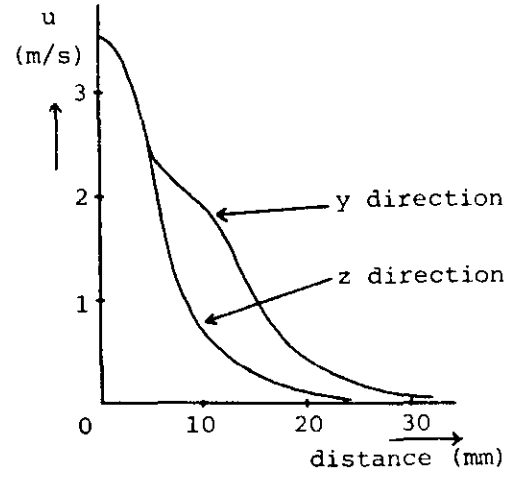

Fig. 3 Average wind velocity versus the y and z coordinates; S_1 = d = h = 30 mm, V = -16 kV.

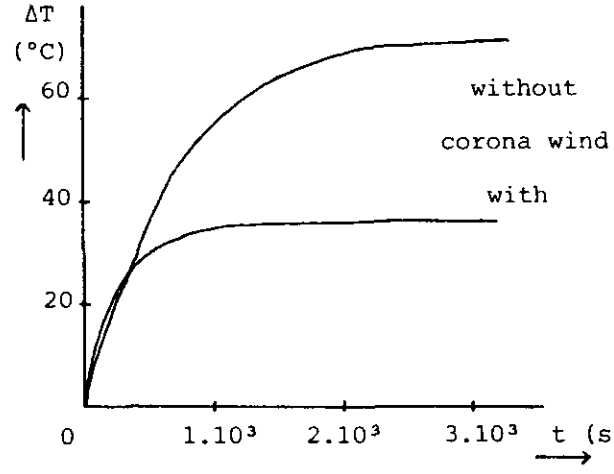

Fig.4 Temperature rise of a horizontal metal plate after the heating elements have been switched on; with and without the corona wind. S_1 = 33 mm, d = 25 mm, h = 40 mm and V = -20 kV.

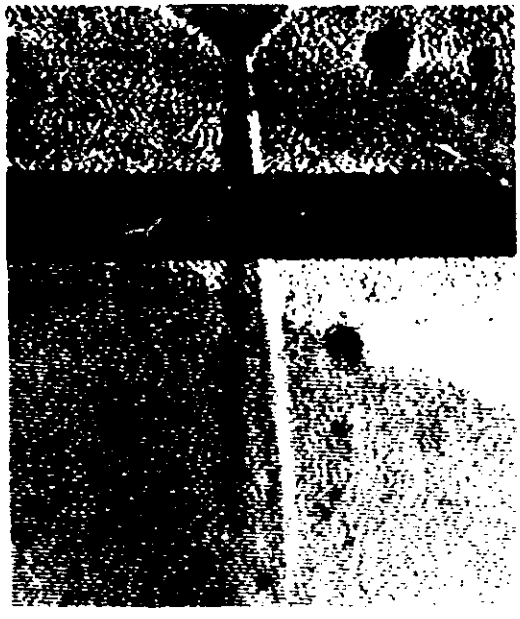

Photograph 1, Schlieren picture of corona wind, originating from a heated point. S_1 = 15 mm, d = 27 mm and V = -18 kV.

Photograph 2, Corona wind influencing artificial mist trails. S_1 = d = 30 mm and V = -20 kV (steady state). Note the discharge point in the top center.

REFERENCES

[1] Hauksbee, F.
PHYSICO-MECHANICAL EXPERIMENTS ON VARIOUS SUBJECTS. Containing an account of several surprizing phenomena touching light and electricity.
London, 1709. P. 46-47. New York: Johnson Reprint Corp., 1970.

[2] Newton, I.
OPTICKS.
London, 1718. New York: Dover, 1979. P. 315-316.

[3] Faraday, M.
EXPERIMENTAL RESEARCHES IN ELECTRICITY.
London: Taylor & Francis, 1839. New York: Dover, 1965, Paragraphs 655, 1443, 1444, 1535, 1592.

[4] Maxwell, J.C.
A TREATISE ON ELECTRICITY AND MAGNETISM. Vol. 1.
Oxford: Clarendon Press/London: Macmillan, 1873.
Clarendon Press Series. P. 52-54.

[5] Chattock, A.P.
ON THE VELOCITY AND MASS OF THE IONS IN THE ELECTRIC WIND IN AIR.
Philos. Mag., Vol. 48(1899), p. 401-420.

[6] Loeb, L.B.
FUNDAMENTALS OF ELECTRICITY AND MAGNETISM. 3rd ed.
New York: Wiley/London: Chapman & Hall, 1947. P. 192-194.

[7] Harney, D.J.
AN AERODYNAMIC STUDY OF THE ELECTRIC WIND.
M.Sc. Thesis. California Institute of Technology, Pasadena, Cal., 1957.

[8] Stuetzer, O.M.
ION DRAG PRESSURE GENERATION.
J. Appl. Phys., Vol. 30(1959), p. 984-994.

[9] Stuetzer, O.M.
ION DRAG PUMPS.
J. Appl. Phys., Vol. 31(1960), p. 136-146.

[10] Robinson, M.
MOVEMENT OF AIR IN THE ELECTRIC WIND OF THE CORONA DISCHARGE.
AIEE Trans., Part 1, Vol. 80(1961) (= Commun. & Electron., No. 54), p. 143-150.

[11] Loeb, L.B.
ELECTRICAL CORONAS: Their basic physical mechanisms.
Berkeley: University of California Press, 1965. P. 402-406.

[12] Senftleben, H.
DIE EINWIRKUNG ELEKTRISCHER UND MAGNETISCHER FELDER AUF DAS WÄRMELEIT-VERMOGEN VON GASEN.
Phys. Z., Vol. 32(1931), p. 550.

[13] Kronig, R. and N. Schwarz
ON THE THEORY OF HEAT TRANSFER FROM A WIRE IN AN ELECTRIC FIELD.
Appl. Sci. Res., Vol. A1(1949), p. 35-46.

[14] Arajs, S. and S. Legvold
ELECTROCONVECTIONAL HEAT TRANSFER IN GASES.
J. Chem. Phys., Vol. 29(1958), p. 531-536.

[15] Lykoudis, P.S. and C.P. Yu
THE INFLUENCE OF ELECTROSTRICTIVE FORCES IN NATURAL THERMAL CONVECTION.
Int. J. Heat & Mass Transfer, Vol. 6(1963), p. 853-862.

[16] Moss, R.A. and J. Grey
HEAT TRANSFER AUGMENTATION BY STEADY AND ALTERNATING ELECTRIC FIELDS.
In: Proc. Heat Transfer and Fluid Mechanics Institute, Santa Clara, Cal., 22-24 June 1966. Ed. by M.A. Saad and J.A. Miller.
Stanford, Cal.: Stanford University Press, 1966. P. 210-235.

[17] O'Brien, R.J. and A.J. Shine
SOME EFFECTS OF AN ELECTRIC FIELD ON HEAT TRANSFER FROM A VERTICAL PLATE IN FREE CONVECTION.
Trans. ASME. J. Heat Transfer, Vol. 89(1967), p. 114-116.

[18] Franke, M.E.
EFFECT OF VORTICES INDUCED BY CORONA DISCHARGE ON FREE-CONVECTION HEAT TRANSFER FROM A VERTICAL PLATE.
Trans. ASME. J. Heat Transfer, Vol. 91(1969), p. 427-433.

[19] McDermott, J.
HIGH-VOLTAGE IONIC DISCHARGES PROVIDE SILENT, EFFICIENT COOLING.
Electron. Des., Vol. 19, No. 20(30 Sept. 1971), p. 22-24.

[20] Sadek, S.E. and R.G. Fax, M. Hurwitz
THE INFLUENCE OF ELECTRIC FIELDS ON CONVECTIVE HEAT AND MASS TRANSFER FROM A HORIZONTAL SURFACE UNDER FORCED CONVECTION.
Trans. ASME. J. Heat Transfer, Vol. 94(1972), p. 144-148.

[21] Kibler, K.G. and H.G. Carter, Jr.
ELECTROCOOLING IN GASES.
J. Appl. Phys., Vol. 45(1974), p. 4436-4440.

[22] Asakawa, Y.
PROMOTION AND RETARDATION OF HEAT TRANSFER BY ELECTRIC FIELDS.
Nature, Vol. 261(1976), p. 220-221.

[23] Yabe, A. and Y. Mori, K. Hijikata
HEAT TRANSFER AUGMENTATION AROUND A DOWNWARD-FACING FLAT PLATE BY NON-UNIFORM ELECTRIC FIELDS.
In: Proc. 6th Int. Heat Transfer Conf., Toronto, 7-11 Aug. 1978. Vol. 3. Ottawa, Ont.: National Research Council of Canada/Washington, D.C.: Hemisphere, 1978. P. 171-176.

[24] Mitchell, A.S. and L.E. Williams
HEAT TRANSFER BY THE CORONA WIND IMPINGING ON A FLAT SURFACE.
J. Electrostat., Vol. 5(1978), p. 309-324. Proc. 2nd Symp. on Electrohydrodynamics, Fort Collins, Colo., 16-18 Jan. 1978. Ed. by T.B. Jones.

[25] Morgan, V.T. and R. Morrow
COOLING OF A HEATED CYLINDER IN STILL AIR BY ELECTRICAL CORONA.
Inst. Eng. Aust. Electr. Eng. Trans., Vol. EE 16(1980), p. 1-5.

[26] Konno, H. and T. Kohya, M. Toda, T. Saito, M. Kuriyama, E. Harada
HEAT TRANSFER FROM A HORIZONTAL FINE WIRE AND CYLINDERS IN A CORONA WIND.
Heat Transfer-Jpn. Res., Vol. 10, No. 2(April-June 1981), p. 20-36.

[27] Blomgren, Jr., O.C. and O.C. Blomgren, Sr., S.R. Griffiths, Jr., E.G. Munck
HEAT CONTROL DEVICE AND METHOD.
US Patent 3,224,485. Issue date 21 Dec. 1965.

[28] Blomgren, Jr., O.C. and O.C. Blomgren, Sr., S.R. Griffiths, Jr., E.G. Munck
METHOD AND APPARATUS FOR LOWERING THE TEMPERATURE OF A HEATED BODY.
US Patent 3,224,497. Issue date 21 Dec. 1965.

[29] Blomgren, Jr., O.C.
METHOD AND APPARATUS FOR THE NONDESTRUCTIVE TESTING OF MATERIALS.
US Patent 3,629,584. Issue date 21 Dec. 1971.

[30] Blomgren, Jr., O.C. and Blomgren, Sr., O.C.
METHOD AND APPARATUS FOR COOLING THE WORKPIECE AND/OR THE CUTTING TOOLS OF A MACHINING APPARATUS.
US Patent 3,670,606. Issue date 20 June 1972.

[31] Blomgren, O.
METHOD AND APPARATUS FOR REMOVING HEAT FROM WITHIN A VACUUM AND FROM WITHIN A MASS.
US Patent 3,735,175. Issue date 22 May 1973.

[32] Lyczko, F.
COOLING APPARATUS.
US Patent 3,747,284. Issue date 24 July 1973.

[33] Blomgren, O.
LOW CURRENT ELECTROSTATIC COOLING METHOD AND APPARATUS FOR ELECTRIC ARC WELDING UTILIZING HIGH VOLTAGE.
US Patent 3,757,079. Issue date 4 Sept. 1973.

[34] Blomgren, Jr., O.C. and O.C. Blomgren, Sr., F.J. Lyczko
COOLING APPARATUS AND METHOD FOR HEAT EXCHANGERS.
US Patent 3,872,917. Issue date 25 March 1975.

[35] Rhodes, I.
PROCESSES OF COOLING FOODS AND APPARATUS THEREFOR.
US Patent 4,072,762. Issue date 7 Febr. 1978.

[36] Rhodes, I.
BAKING OVENS. British Patent 1,122,514. Issue date 7 April 1966. And:
PROCESSES OF COOKING FOODS, AND APPARATUS THEREFOR. Can. Patent 783,385.
Issue date 23 April 1968.

[37] Velkoff, H.R. and F.A. Kulacki
ELECTROSTATIC COOLING.
ASME Paper No. 77-DE-36. Design Engineering Conf. and Show, Chicago, 9-12 May 1977.
New York: American Society of Mechanical Engineers, 1977.

[38] Kulacki, F.A. and J.A. Daumenmier
A PRELIMINARY STUDY OF ELECTROHYDRODYNAMIC AUGMENTED BAKING.
J. Electrostat., Vol. 5(1978), p. 325-336. Proc. 2nd Symp. on
Electrohydrodynamics, Fort Collins, Colo., 16-18 Jan. 1978. Ed. by T.B. Jones.

[39] Chapman, A.J.
HEAT TRANSFER. 3rd ed.
New York: Macmillan, 1974. P. 3-15.

[40] Eckert, E.R.G. and R.M. Drake, Jr.
HEAT AND MASS TRANSFER.
New York: McGraw-Hill, 1959.
McGraw-Hill series in mechanical engineering. P. 1-21.

[41] Rohsenow, W.M. and H.Y. Choi
HEAT, MASS, AND MOMENTUM TRANSFER.
Englewood Cliffs, N.J.: Prentice-Hall, 1961. P. 87-92.

[42] Prandtl, L.
ÜBER FLÜSSIGKEITSBEWEGUNG BEI SEHR KLEINER REIBUNG.
In: Proc. 3rd Int. Mathematical Congress, Heidelberg, 1904. P. 484-491.

[43] Kuffel, E. and W.S. Zaengl
HIGH-VOLTAGE ENGINEERING: Fundamentals.
Oxford: Pergamon, 1984.
Applied electricity and electronics. P. 377-383.

[44] Cobine, J.D.
GASEOUS CONDUCTORS: Theory and engineering applications.
New York: Dover, 1958. Reprint of the 1941 ed. P. 205-289.

[45] Nasser, E.
FUNDAMENTALS OF GASEOUS IONIZATION AND PLASMA ELECTRONICS.
New York: Wiley, 1971.
Wiley series in physics. P. 332-354.

[46] Goldman, M. and A. Goldman
CORONA DISCHARGES.
In: Gaseous Electronics. Vol. 1: Electrical discharges. Ed. by M.N. Hirsh
and H.J. Oskam.
New York: Academic Press, 1978. P. 219-290.

[47] Lama, W.L. and C.F. Gallo
SYSTEMATIC STUDY OF THE ELECTRICAL CHARACTERISTICS OF THE "TRICHEL" CURRENT
PULSES FROM NEGATIVE NEEDLE-TO-PLANE CORONAS.
J. Appl. Phys., Vol. 45(1974), p. 103-113.

[48] Sigmond, R.S.
CORONA DISCHARGES.
In: Electrical Breakdown of Gases. Ed. by J.M. Meek and J.D. Craggs.
Chichester: Wiley, 1978.
Wiley series in plasma physics. P. 319-384.

[49] Gravendeel, B. and P.C.T. van der Laan
FAST CURRENT MEASUREMENTS IN CORONA AND LASER-TRIGGERED CORONA-LIKE DISCHARGES.
In: Proc. 8th Int. Conf. on Gas Discharges and their Applications, Oxford,
16-20 Sept. 1985.
Leeds University Press/Oxford: Pergamon, 1985. P. 216-218.

[50] Peek, W.F.
DIELECTRIC PHENOMENA IN HIGH-VOLTAGE ENGINEERING.
New York: McGraw-Hill, 1929.

[51] Waters, R.T. and W.B. Stark
CHARACTERISTICS OF THE STABILIZED GLOW DISCHARGE IN AIR.
J. Phys. D, Vol. 8(1975), p. 416-426.

[52] Zalesski, A.M.
Trudy Leningradskogo Polytechničeskogo Instituta im. M.I. Kalinina (Trudy LPI), Vol. 3(1948), p. 94-99.

[53] Hartmann, G.
THEORETICAL EVALUATION OF PEEK'S LAW.
IEEE Trans. Ind. Appl., Vol. IA-20(1984), p. 1647-1651.

[54] Townsend, J.S.
THE POTENTIALS REQUIRED TO MAINTAIN CURRENTS BETWEEN COAXIAL CYLINDERS.
Philos. Mag., Vol. 28(1914), p. 83-90.

[55] = [47]

[56] = [51]

[57] Thomson, J.J. and G.P. Thomson
CONDUCTION OF ELECTRICITY THROUGH GASES. Vol. 2: Ionisation by collision and the gaseous discharge.
Cambridge University Press, 1933. New York: Dover 1969. P. 552.

[58] Henson, B.L.
A SPACE-CHARGE REGION MODEL FOR MICROSCOPIC STEADY CORONAS FROM POINTS.
J. Appl. Phys., Vol. 52(1981), p. 709-715.

[59] Henson, B.L.
DERIVATION OF THE CURRENT-POTENTIAL EQUATION FOR STEADY POINT-TO-PLATE CORONA DISCHARGES.
J. Appl. Phys., Vol. 53(1982), p. 3305-3307.

[60] Warburg, E.
ÜBER DIE STILLE ENTLADUNG IN GASEN.
In: Handbuch der Physik, Vol. 14. Herausgegeben von H. Geiger und K. Scheel.
Berlin: Springer, 1927. P. 149-170.

[61] Sigmond, R.S.
SIMPLE APPROXIMATE TREATMENT OF UNIPOLAR SPACE-CHARGE-DOMINATED CORONAS: The Warburg law and saturation current.
J. Appl. Phys., Vol. 53(1982), p. 891-898.

[62] Melcher, J.R.
FIELD-COUPLED SURFACE WAVES: A comparative study of surface-coupled electrohydrodyanmic and magnetohydrodynamic systems.
Cambridge, Mass.: MIT Press, 1963. P. 22-23.

[63] Stratton, J.A.
ELECTROMAGNETIC THEORY.
New York: McGraw-Hill, 1941.
International series in pure and applied physics. P. 145-146.

[64] Felici, N.J.
ELECTROSTATICS AND HYDRODYNAMICS.
J. Electrostat., Vol. 4(1977/1978), p. 119-129.

[65] Schlichting, H.
BOUNDARY-LAYER THEORY. 7th ed.
London: McGraw-Hill, 1979.
McGraw-Hill series in mechanical engineering. P. 179-181.

[66] Duckworth, R.A.
MECHANICS OF FLUIDS.
London: Longman, 1977.
Introductory engineering series. P. 86-87.

[67] Massey, B.S.
MECHANICS OF FLUIDS. 3rd ed.
New York: Van Nostrand Reinhold, 1975. P. 89-91.

[68] Jonas, P.
THE CHANGES PRODUCED IN AN AIR STREAM BY WIRE GAUZE.
Eng. Dig., Vol. 18, No. 5(May 1957), p. 191-193. English Abstract from:
Czech. J. Phys., Vol. 7, No. 2(1957), p. 202-212.

[69] Smol'yakov, A.V. and V.M. Tkachenko
THE MEASUREMENT OF TURBULENT FLUCTUATIONS: An introduction to hot-wire anemometry and related transducers.
New York: Springer, 1983. P. 65-67. Transl. from Russian: Moskva: Energija, 1980.

[70] Reynolds, A.J.
TURBULENT FLOWS IN ENGINEERING.
London: Wiley, 1974. P. 57-64.

[71] Bradshaw, P.
AN INTRODUCTION TO TURBULENCE AND ITS MEASUREMENT.
Oxford: Pergamon, 1971.
Commonwealth and international library: Thermodynamics and fluid mechanics.
P. 112-117 and p. 119-123.

[72] Kumaran, A. and R. Leach, S.A. Self
ANOMALOUS READINGS FROM HOT WIRE ANEMOMETERS IN STRONG ELECTRIC FIELDS.
T.S.I.Quarterly, Vol. 9, No. 3(July-Sept. 1983), p. 9-11.

[73] Merzkirch, W.
FLOW VISUALIZATION.
New York: Academic Press, 1974. P. 86-100.

[74] Schardin, H.
DIE SCHLIERENVERFAHREN UND IHRE ANWENDUNGEN.
In: Ergebnisse der exakten Naturwissenschaften. Band 20. Herausgegeben von S. Flügge et al.
Berlin: Springer, 1942. P. 303-439.

[75] Adachi, T.
IONIC WIND IN THE ELECTROSTATIC PRECIPITATION: Experimental treatment by Schlieren method.
Electr. Eng. Japan, Vol. 93, No. 4(1973), p. 43-49. Transl. from: Denki Gakkai Ronbunshi, Vol. 93B, No. 7(July 1973), p. 273-280.

[76] Moore, C.J.
THE ROLE OF SHEAR-LAYER INSTABILITY WAVES IN JET EXHAUST NOISE.
J. Fluid Mech., Vol. 80(1977), p. 321-367.

[77] Heavens, S.N.
VISUALIZATION OF UNSTEADY JETS AND AERODYNAMIC NOISE FIELDS.
In: Proc. 13th Int. Congress on High Speed Photography and Photonics, Tokyo, 20-25 August 1978. Ed. by Shin-ichi Hyodo.
Tokyo: Japan Society of Precision Engineering/Bellingham, Wash.: Society of Photo-Optical Instrumentation Engineers, 1978.
Proceedings SPIE, Vol. 189. P. 676-683.

[78] Baricos, J. and J. Dupuy, R. Peyrous, G. Schreiber
CORONA DISCHARGE AND ENERGY TRANSFER.
J. Phys. D, Vol. 11(1978), p. L187-L190.

[79] Kurimoto, A. and O. Farish
NEGATIVE D.C. CORONA STUDY IN ATMOSPHERIC AIR USING SCHLIEREN AND INTERFEROMETRIC TECHNIQUES.
IEE Proc. A, Vol. 127(1980), p. 89-94.

[80] Kurimoto, A. and O. Farish, D.J. Tedford
SCHLIEREN STUDIES OF IMPULSE BREAKDOWN IN AIR GAPS.
Proc. IEE, Vol. 125(1978), p. 767-769.

[81] Boulloud, A. and J. Charrier
CURRENT DENSITY ON THE PLANE ELECTRODE OF A POSITIVE POINT-TO-PLANE GLOW CORONA DISCHARGES.
In: Proc. 6th Int. Conf. on Gas Discharges and their Applications, Edinburgh, 8-11 Sept. 1980.
London: Institution of Electrical Engineers, 1980.
IEE Conference Publication, No. 189, Part 1. P. 110-113.

[82] Boulloud,A. and J. Charrier
POSITIVE GLOW CORONA AT A POINT IN AIR: Stabilization of the dual-patch regime.
In: Proc. 7th Int. Conf. on Gas Discharges and their Applications, London, 31 Aug.-3 Sept. 1982.
Stevenage: Peter Peregrinus, 1982.
PPL Conference, No. 20. P. 151-154.

[83] Boulloud,A. and J. Charrier, W.B. Stark, R.T. Waters
INTERACTION BETWEEN ADJACENT POSITIVE GLOW CORONA.
Ibid., p. 185-188.

[84] Merzkirch, W.F.
A SIMPLE SCHLIEREN INTERFEROMETER SYSTEM.
AIAA J., Vol. 3(1965), p. 1974-1976.

[85] Rye, B.J. and J.W. Waller, A.S.V. McKenzie, J. Irving
SCHLIEREN PHOTOGRAPHY OF THE FIRST HALF-CYCLE OF A THETA PINCH DISCHARGE.
Br. J. Appl. Phys., Vol. 16(1965), p. 1404-1406.

[86] Thompson, L.L. and L.S. Taylor
ANALYSIS OF TURBULENCE BY SCHLIEREN PHOTOGRAPHY.
AIAA J., Vol. 7(1969), p. 2030-2031.

[87] Davis, M.R.
MEASUREMENTS IN A SUBSONIC TURBULENT JET USING A QUANTITATIVE SCHLIEREN TECHNIQUE.
J. Fluid Mech., Vol. 46(1971), p. 631-656.

[88] Kogelschatz, U. and W.R. Schneider
QUANTITATIVE SCHLIEREN TECHNIQUES APPLIED BY HIGH CURRENT ARC INVESTIGATIONS.
Appl. Opt., Vol. 11(1972), p. 1822-1832.

[89] Ineichen, B. and U. Kogelschatz, R. Dändliker
SCHLIEREN DIAGNOSTICS AND INTERFEROMETRY OF AN ARC DISCHARGE USING PULSED HOLOGRAPHY.
Appl. Opt., Vol. 12(1973), p. 2554-2556.

[90] Vaessen, P.T.M.
CORONA WIND AND HEAT TRANSFER.
M.Sc. Thesis. High-Voltage Group, Dept. of Electrical Engineering, Eindhoven University of Technology, 1985.

[91] Tritton, D.J.
PHYSICAL FLUID DYNAMICS.
New York: Van Nostrand Reinhold, 1977.
The modern university physics series. P. 112-115.

[92] Rajaratnam, N.
TURBULENT JETS
Amsterdam: Elsevier, 1976.
Developments in water science, Vol. 5. P. 27-49.

[93] Higgins, R.A.
ENGINEERING METALLURGY. Part 1: Applied physical metallurgy.
London: English Universities Press, 1957.
The technical college series. P. 378, tab. 23.1.

[94] STANDARD HANDBOOK FOR ELECTRICAL ENGINEERS. 10th ed. Ed. by D.G. Fink and J.M. Carroll.
New York: McGraw-Hill, 1968. P. 3-248, tab. 3.11.

[95] Hayne, T.F.
SCREEN CONTROLLED CORONA DEVICE (SCOROTRON) FOR CHARGING IN A XEROGRAPHIC COPIER.
IEEE Trans. Ind. Appl., Vol. IA-12(1976), p. 63-67.

[96] Goldman, A. and R. Haug, R.V. Latham
A REPULSIVE-FIELD TECHNIQUE FOR OBTAINING THE MOBILITY-SPECTRA OF THE ION SPECIES CREATED IN A CORONA DISCHARGE.
J. Appl. Phys., Vol. 47(1976), p. 2418-2423.

[97] Masuda, S. and A. Mizuno
INITIATION CONDITION AND MODE OF BACK DISCHARGE.
J. Electrostat., Vol. 4(1977/1978), p. 35-52.

[98] Withers, R.S. and J.R. Melcher, J.W. Richmann
CHARGING, MIGRATION AND ELECTROHYDRODYNAMIC TRANSPORT OF AEROSOLS.
J. Electrostat., Vol. 5(1978), p. 225-239. Proc. 2ns Symp. on Electrohydrodynamics, Fort Collins, Colo., 16-18 Jan. 1978. Ed. by T.B. Jones.

[99] Allen, N.L. and Y. Teisseyre, P. Ballereau, M. Goldman
ELECTRICAL WIND AND IONIC SPECIES FORMED BY POINT-PLANE CORONA.
In: Proc. 6th Int. Conf. on Gas Discharges and their Applications, Edinburgh, 8-11 Sept. 1980.
London: Institution of Electrical Engineers, 1980.
IEE Conference Publication, No. 189, Part 1. P. 150-152.

[100] Gross, B. and J.A. Giacometti, G.F. Leal Ferreira, O.N. Oliveira, Jr.
CONSTANT CURRENT CORONA CHARGING OF PVF_2.
J. Appl. Phys., Vol. 56(1984), p. 1487-1491.

[101] Bradley, R.F. and J.F. Hoburg
ELECTROHYDRODYNAMIC AUGMENTATION OF FORCED CONVECTION HEAT TRANSFER.
IEEE Trans. Ind. Appl., Vol. IA-21(1985), p. 1373-1376.

[102] McLean, K.J. and Z. Herceg, R.I. Boccola
ELECTRICAL TRANSPARENCY OF A CORONA TRIODE.
J. Electrostat., Vol. 9(1981), p. 211-222.

[103] Haug, R. and J. Lebas, Y. Teisseyre
ION CURRENT CALCULATION IN A SYSTEM OF PLANE GRIDS IN AN IONISED GAS FLOW.
J. Phys. D, Vol. 17(1984), p. 357-366. In French.

[104] Haug, R. and J. Lebas, Y. Teisseyre
NUMERICAL SIMULATION OF THE IONIC TRANSPARENCY FOR A GRID IN AN IONSED GAS-FLOW.
J. Phys. D, Vol. 15(1982), p. 1709-1720. In French.

[105] Haug, R. and J. Lebas, Y. Teisseyre
MAY THE CURRENT DELIVERED BY AN ION SOURCE AND COLLECTED BY A SURFACE BE INDEPENDENT OF THE DISTANCE?
In: Proc. 8th Int. Conf. on Gas Discharges and their Applications, Oxford, 16-20 Sept. 1985.
Leeds University Press/Oxford: Pergamon, 1985. P. 439-440.

[106] Lebas, J. and R. Haug, Y. Teisseyre
INFLUENCE OF THE GRID TRANSPARENCY IN ION-MOBILITY MEASUREMENTS.
In: Proc. 7th Int. Conf. on Gas Discharges and their Applications, London, 31 August - 3 Sept. 1982.
Stevenage: Peter Peregrinus, 1982.
PPL Conference, No. 20. P. 332-334.

[107] Oliveira, Jr., O.N. and G.F. Leal Ferreira
GRID-TO-PLATE CURRENT-VOLTAGE CHARACTERISTICS OF A CORONA TRIODE.
Rev. Sci. Instrum., Vol. 56(1985), p. 1957-1961.

[108] Weber, E.
ELECTROMAGNETIC FIELDS: Theory and applications. Vol. 1: Mapping of fields.
New York: Wiley/London: Chapman & Hall, 1950. P. 291-297.

[109] Langmuir, I.
THE EFFECT OF SPACE CHARGE AND RESIDUAL GASES ON THERMIONIC CURRENTS IN HIGH VACUUM.
Phys. Rev., Vol. 2(1913), p. 450-486.

ACKNOWLEDGEMENTS

My sincere and deepfelt thanks go to Prof. dr. P.C.T. van der Laan whose constant illuminating guidance during the course of the research work has ensured my successful completion of this work. I also wish to express my gratitude to Ing. Piet Gulickx for his assistance in the technical work. The technical assistance in carrying out experimental work at Eindhoven University of Technology by graduate student P.T.M. Vaessen and the stimulating discussions with him are deeply appreciated. Frans Schulpen assisted in schlieren measurements and A.G.W.M Berkers assisted in heat transfer measurements during their undergraduate projects work at Eindhoven University of Technology. The experimental work which was carried out at the University of Dar es Salaam received the assistance of my student B.M.M. Mwinyiwiwa.

This work has been supported by the Netherlands Universities Foundation (NUFFIC), the University of Dar es Salaam, and Eindhoven University of Technology.

AUTOBIOGRAPHY

Henry Kadete

The author was born on the 23rd of August 1954 at Igalula, Tabora region,western Tanzania to Damson Kaunga Kadete and Yohana Herman Maganga. He is Tanzanian. He received his primary school education at Nturu Primary School, Igalula(1961-1962) and later at Inala Primary School(1962-1964) where he had to follow his father who was a village primary school headmaster. He completed his primary school education at Chabutwa Upper Primary School(1965-1967). He proceeded to Tabora Boys' Secondary School(1968-1971) and later went to Kibaha High School (1972-1973). After completing his high school education he was awarded an All African Universities(AAU) scholarship to pursue a B.Sc.E.E degree at The University of Lagos, Nigeria(1974-1977). He joined the Department of Electrical Engineering, University of Dar es Salaam as a Tutorial Assistant soon after the completion of his first degree studies in 1977. He then proceeded to the University of Manchester Institute of Science and Technology(UMIST) in England for a masters degree in high voltage engineering and electrical power systems which was awarded to him in 1980. The author has worked with UNILEVER Engineering Division in Rotterdam as a plant electrification engineer trainee for one year(1981). He has worked for his Ph. D.thesis under the guidance of Prof. dr. P.C.T. van. der Laan in the high-voltage laboratory at Eindhoven University of Technology for two years (1984 and 1986). For a period of one year (1985) he

did some experiments at the high-voltage laboratory of the University of Dar es Salaam as part of his Ph. D. work. The author is a lecturer in high-voltage engineering and electrical power systems at the department of electrical engineering, University of Dar es Salaam. He is married to Chem-Chemi, with whom they have one son, Camara.

Eindhoven University of Technology Research Reports
Faculty of Electrical Engineering

ISSN 0167-9708
Coden: TEUEDE

(166) Dielen, M. and J.F.M. Theeuwen
AN OPTIMAL CMOS STRUCTURE FOR THE DESIGN OF A CELL LIBRARY.
EUT Report 87-E-166. 1987. ISBN 90-6144-166-8

(167) Oerlemans, C.A.M. and J.F.M. Theeuwen
ESKISS: A program for optimal state assignment.
EUT Report 87-E-167. 1987. ISBN 90-6144-167-6

(168) Linnartz, J.P.M.G.
SPATIAL DISTRIBUTION OF TRAFFIC IN A CELLULAR MOBILE DATA NETWORK.
EUT Report 87-E-168. 1987. ISBN 90-6144-168-4

(169) Vinck, A.J. and Pineda de Gyvez, K.A. Post
IMPLEMENTATION AND EVALUATION OF A COMBINED TEST-ERROR CORRECTION PROCEDURE FOR MEMORIES WITH DEFECTS.
EUT Report 87-E-169. 1987. ISBN 90-6144-169-2

(170) Hou Yibin
DASM: A tool for decomposition and analysis of sequential machines.
EUT Report 87-E-170. 1987. ISBN 90-6144-170-6

(171) Monnee, P. and M.H.A.J. Herben
MULTIPLE-BEAM GROUNDSTATION REFLECTOR ANTENNA SYSTEM: A preliminary study.
EUT Report 87-E-171. 1987. ISBN 90-6144-171-4

(172) Bastiaans, M.J. and A.H.M. Akkermans
ERROR REDUCTION IN TWO-DIMENSIONAL PULSE-AREA MODULATION, WITH APPLICATION TO COMPUTER-GENERATED TRANSPARENCIES.
EUT Report 87-E-172. 1987. ISBN 90-6144-172-2

(173) Zhu Yu-Cai
ON A BOUND OF THE MODELLING ERRORS OF BLACK-BOX TRANSFER FUNCTION ESTIMATES.
EUT Report 87-E-173. 1987. ISBN 90-6144-173-0

(174) Berkelaar, M.R.C.M. and J.F.M. Theeuwen
TECHNOLOGY MAPPING FROM BOOLEAN EXPRESSIONS TO STANDARD CELLS.
EUT Report 87-E-174. 1987. ISBN 90-6144-174-9

(175) Janssen, P.H.M.
FURTHER RESULTS ON THE McMILLAN DEGREE AND THE KRONECKER INDICES OF ARMA MODELS.
EUT Report 87-E-175. 1987. ISBN 90-6144-175-7

(176) Janssen, P.H.M. and P. Stoica, T. Söderström, P. Eykhoff
MODEL STRUCTURE SELECTION FOR MULTIVARIABLE SYSTEMS BY CROSS-VALIDATION METHODS.
EUT Report 87-E-176. 1987. ISBN 90-6144-176-5

(177) Stefanov, B. and A. Veefkind, L. Zarkova
ARCS IN CESIUM SEEDED NOBLE GASES RESULTING FROM A MAGNETICALLY INDUCED ELECTRIC FIELD.
EUT Report 87-E-177. 1987. ISBN 90-6144-177

(178) Janssen, P.H.M. and P. Stoica
ON THE EXPECTATION OF THE PRODUCT OF FOUR MATRIX-VALUED GAUSSIAN RANDOM VARIABLES.
EUT Report 87-E-178. 1987. ISBN 90-6144-178-1

(179) Lieshout, G.J.P. van and L.P.P.P. van Ginneken
GM: A gate matrix layout generator.
EUT Report 87-E-179. 1987. ISBN 90-6144-179-X

(180) Ginneken, L.P.P.P. van
GRIDLESS ROUTING FOR GENERALIZED CELL ASSEMBLIES: Report and user manual.
EUT Report 87-E-180. 1987. ISBN 90-6144-180-3

(181) Bollen, M.H.J. and P.T.M. Vaessen
FREQUENCY SPECTRA FOR ADMITTANCE AND VOLTAGE TRANSFERS MEASURED ON A THREE-PHASE POWER TRANSFORMER.
EUT Report 87-E-181. 1987. ISBN 90-6144-181-1

(182) Zhu Yu-Cai
BLACK-BOX IDENTIFICATION OF MIMO TRANSFER FUNCTIONS: Asymptotic properties of prediction error models.
EUT Report 87-E-182. 1987. ISBN 90-6144-182-X

(183) Zhu Yu-Cai
ON THE BOUNDS OF THE MODELLING ERRORS OF BLACK-BOX MIMO TRANSFER FUNCTION ESTIMATES.
EUT Report 87-E-183. 1987. ISBN 90-6144-183

(184) Kadete, H.
ENHANCEMENT OF HEAT TRANSFER BY CORONA WIND.
EUT Report 87-E-184. 1987. ISBN 90-6144-184-6